REPORT DOCUMENTATION PAGE

Form Approved OMB NO. 0704-0188

1. REPORT DATE (DD-MM-YYYY)	2. REPORT TYPE	3. DATES COVERED (From - To)
06-07-2020	Final Report	15-Mar-2019 - 14-Mar-2020

4. TITLE AND SUBTITLE
Final Report: DURIP: Center for Semiconductor Modelling Computational Infrastructure

5a. CONTRACT NUMBER
W911NF-19-1-0161

5b. GRANT NUMBER

5c. PROGRAM ELEMENT NUMBER
611103

6. AUTHORS

5d. PROJECT NUMBER

5e. TASK NUMBER

5f. WORK UNIT NUMBER

7. PERFORMING ORGANIZATION NAMES AND ADDRESSES
Boston University
Office of Sponsored Program
881 Commonwealth Avenue
Boston, MA 02215 -1300

8. PERFORMING ORGANIZATION REPORT NUMBER

9. SPONSORING/MONITORING AGENCY NAME(S) AND ADDRESS (ES)
U.S. Army Research Office
P.O. Box 12211
Research Triangle Park, NC 27709-2211

10. SPONSOR/MONITOR'S ACRONYM(S)
ARO

11. SPONSOR/MONITOR'S REPORT NUMBER(S)
73884-MA-RIP.1

12. DISTRIBUTION AVAILIBILITY STATEMENT
Approved for public release; distribution is unlimited.

13. SUPPLEMENTARY NOTES
The views, opinions and/or findings contained in this report are those of the author(s) and should not contrued as an official Department of the Army position, policy or decision, unless so designated by other documentation.

14. ABSTRACT

15. SUBJECT TERMS

16. SECURITY CLASSIFICATION OF:			17. LIMITATION OF ABSTRACT	15. NUMBER OF PAGES	19a. NAME OF RESPONSIBLE PERSON
a. REPORT	b. ABSTRACT	c. THIS PAGE			Enrico Bellotti
UU	UU	UU	UU		19b. TELEPHONE NUMBER 617-358-1576

RPPR Final Report
as of 08-Jul-2020

Agency Code:

Proposal Number: 73884MARIP **Agreement Number: W911NF-19-1-0161**
INVESTIGATOR(S):

Name: Enrico Bellotti
Email: bellotti@bu.edu
Phone Number: 6173581576
Principal: Y

Organization: **Boston University**
Address: Office of Sponsored Program, Boston, MA 022151300
Country: USA
DUNS Number: 049435266 EIN: 042103547

Report Date: 14-Jun-2020 Date Received: 06-Jul-2020
Final Report for Period Beginning 15-Mar-2019 and Ending 14-Mar-2020
Title: DURIP: Center for Semiconductor Modelling Computational Infrastructure
Begin Performance Period: 15-Mar-2019 **End Performance Period:** 14-Mar-2020
Report Term: 0-Other

Submitted By: Enrico Bellotti Email: bellotti@bu.edu
Phone: (617) 358-1576

Distribution Statement: 1-Approved for public release; distribution is unlimited.

STEM Degrees: 0 **STEM Participants:**

Major Goals: To better understand these risks, Bajaj and co-authors have surveyed the development process of several technologies that are relevant for the ARMY and their transition to systems. They have pointed out that a novel approach is necessary to improve the ability of the science and technology community to develop novel semiconductor devices and transition into specific system applications. Specifically, they emphasized that the timely technology transition with minimal risk requires an understanding of fundamental and technology limitations of material synthesis, device operation and design controllable parameters. However, this knowledge-based approach requires substantial investment of resources in the Science and Technology (S&T) stage of development. For low volume niche semiconductor technologies of DoD relevance, industry alone cannot justify these investments simply because there is no significant return on investment. As a result, technology transition from S&T to product development is often expensive, delayed, and carries
risks. To address this challenge, the Computational Electronics Group at Boston University led by Prof. E. Bellotti and a team from the Army Research Laboratory led by Dr. M. Reed have worked to establish the Center for Semiconductor Modeling (CSM). The CSM immediate scientific focus will be to develop robust and predictive models to minimize risk in developing new technology. The CSM will focus on the theory, simulation and the experimental validation of the models.

Accomplishments: The computational platform acquired with the DURIP 2019 funding has enabled the Computational Electronics Group at Boston University to investigate and answer a number of fundamental questions related to semiconductor materials and devices of interested for DoD and the ARMY.

- We have investigate the nature of InAs1?xSbx alloys that are important for the design of a variety of infrared detectors. Specifically we have theoretically determined the behavior of the energy gap of these alloys as a function of the composition and shown that it is similar to what was measured by the group of S. Svensson at ARL.

- We have computed the band offsets of AlxGa1-xN alloys that are very important for a number of critical applications of interest to the ARMY. The knowledge of the band edge (valence and conduction) offsets is critical to the device design.

- We have shown that the presence of disorder, regardless its nature and cause, introduces fundamental limitations to the vertical carrier transport properties of gallium free strained balanced InAs/InxAs1-xSb type-II superlattices. These limitations become particularly severe at low operating temperature that are normally required to reduce noise and dark current. Furthermore, when holes are the minority carrier that contribute to the device photocurrent, the degradation of their transport coefficient is so dramatic that the operation of detector may be

compromised.

- Three journal papers and a conference paper (invited talk) where published as a result of the investigations that were made possible by the system that was acquired. Two more journal papers are under review.

The final hardware that was acquired in composed of:

- Ten nodes with two Intel Xeon Gold 6248 processors, each with 20 cores, 768GB of memory, 10Gb and 100Gb EDR interfaces.
- Two nodes with two Intel Xeon Gold 6248 processors, each with 20 cores, 1.5TB of memory, 10Gb and 100Gb EDR interfaces.
- A file server with two Intel Xeon Gold 6248 processors, each with 20 cores, 256GB of memory, 10Gb and 100Gb EDR interfaces, and 97TB of solid state storage.
- A 36-port EDR 100Gb InfiniBand switch.

The system has been installed in a rack within the main server room in the BU campus and uses the main communication backbone of the room, the redundant power and connectivity. This approach does allow the system to be operational during power line and network maintenance. The system has had 100% availability since the installation and acceptance test were completed at the end of August 2019.

Training Opportunities: The equipment purchased through the 2019 DURIP award to the Boston University Computational Electronics group has supported the ongoing research activities of two post-doctoral associates and five PhD students actively involved in DoD funded programs. Besides supporting their ongoing research, the acquisition of the new computational resources provided impetus to investigate the development of computationally efficient software. For example, the increasing availability of machine time across the cluster led to the use of MPI and OpenMP to distribute programs across a number of physically separate compute nodes. These techniques have been integrated into existing software. Additionally, having removed the machine availability bottleneck, a significant effort was devoted towards developing codes and methods for automating designs to increase overall throughput. The students have also been able to present their work at several high-profile conferences (SPIE Photonics West, Defense, Security + Sensing, Optics and Photonics) where it is possible to engage researchers from various DoD organizations.

RPPR Final Report
as of 08-Jul-2020

Results Dissemination: The following DoD funded publications have been supported in part by the equipment purchased through the 2019 DURIP award to the Boston University Computational Electronics Group:

Manuscripts Published

1 - A. Kyrtsos, M. Matsubara, and E. Bellotti, Investigation of the band gaps and bowing parameter of InAs1?xSbx alloys using the modified Becke-Johnson potential, Phys. Rev. Materials, Vol.4 No.1 Article Number: 014603, January 8 2020.

2 - A. Kyrtsos, M. Matsubara, and E. Bellotti, Band offsets of AlxGa1?xN alloys using first-principles calculations, J. Phys. Condens. Matter, Vol. 32, p.365504, May 2020

3 - F. Bertazzi, A. Tibaldi, J.A.G. Montoya, M. Goano, E. Bellotti, Non-equilibrium Green's function modeling of type-II superlattice detectors and its connection to semiclassical approaches, Phys. Rev. Applied, Accepted 29 June, 2020.

Conference Papers and Presentation

1 - E. Bellotti, F. Bertazzi, J. Bajaj, J. Schuster, M. Reed Understanding Fundamental Material Limitations to Enable Advanced Detector Design, NUSOD 2019, Invited Talk, conference paper at https://ieeexplore.ieee.org/abstract/document/8807083.

Manuscripts under review

1 – S.P. Svensson, W.L. Sarney,W.A. Beck,J. Liu, D. Donetsky, S. Suchalkin, G. Belenky, A. Kyrtsos, and E. Bellotti, P-doping with Beryllium of long-wavelength InAsSb, Semiconductor Science and Technology, under review

2 – A. Glasmann, A. Kyrtsos, and E. Bellotti, Machine learning for analyzing and characterizing InAsSb-based nBn photodetectors, Phys. Rev. Applied, under review.

Honors and Awards: Nothing to Report

Protocol Activity Status:

Technology Transfer: Nothing to Report

PARTICIPANTS:

Participant Type: PD/PI
Participant: Enrico Bellotti
Person Months Worked: 1.00 **Funding Support:**
Project Contribution:
International Collaboration:
International Travel:
National Academy Member: N
Other Collaborators:

Participant Type: Faculty
Participant: Francesco Bertazzi
Person Months Worked: 1.00 **Funding Support:**
Project Contribution:
International Collaboration:
International Travel:
National Academy Member: N
Other Collaborators:

RPPR Final Report
as of 08-Jul-2020

Participant Type: Graduate Student (research assistant)
Participant: Andreu Glassman
Person Months Worked: 12.00 **Funding Support:**
Project Contribution:
International Collaboration:
International Travel:
National Academy Member: N
Other Collaborators:

Participant Type: Postdoctoral (scholar, fellow or other postdoctoral position)
Participant: Alexandros Kyrtsos
Person Months Worked: 6.00 **Funding Support:**
Project Contribution:
International Collaboration:
International Travel:
National Academy Member: N
Other Collaborators:

Final Report

DURIP: Center for Semiconductor Modelling Computational Infrastructure

2019 DoD DURIP Program

Contract # W911NF-19-0161.

PI: Prof. Enrico Bellotti
Department of Electrical and Computer Engineering
8 Saint Mary's Street
Boston, MA 02215
bellotti@bu.edu

ARO Technical POC: Dr. Joseph Myers
U.S. Army Research Office RDRL-ROI-M
Box 12211 Research Triangle Park, NC 27709-2211
josephd.myers@us.army.mil
Tel. (919) 549-4245

Table of Contents

Summary

The computational platform acquired with the DURIP 2019 funding has enabled the Computational Electronics Group at Boston University to investigate and answer a number of fundamental questions related to semiconductor materials and devices of interested for DoD and the ARMY.

- We have investigate the nature of $InAs_{1-x}Sb_x$ alloys that are important for the design of a variety of infrared detectors. Specifically we have theoretically determined the behavior of the energy gap of these alloys as a function of the composition and shown that it is similar to what was measured by the group of S. Svensson at ARL.

- We have computed the band offsets of $Al_xGa_{1-x}N$ alloys that are very important for a number of critical applications of interest to the ARMY. The knowledge of the band edge (valence and conduction) offsets is critical to the device design.

- We have shown that the presence of disorder, regardless its nature and cause, introduces fundamental limitations to the vertical carrier transport properties of gallium free strained balanced $InAs/In_xAs_{1-x}Sb$ type-II superlattices. These limitations become particularly severe at low operating temperature that are normally required to reduce noise and dark current. Furthermore, when holes are the minority carrier that contribute to the device photocurrent, the degradation of their transport coefficient is so dramatic that the operation of detector may be compromised.

- Three journal papers and a conference paper (invited talk) where published as a result of the investigations that were made possible by the system that was acquired. Two more journal papers are under review.

The final hardware that was acquired in composed of:

- Ten nodes with two Intel Xeon Gold 6248 processors, each with 20 cores, 768GB of memory, 10Gb and 100Gb EDR interfaces.
- Two nodes with two Intel Xeon Gold 6248 processors, each with 20 cores, 1.5TB of memory, 10Gb and 100Gb EDR interfaces.
- A file server with two Intel Xeon Gold 6248 processors, each with 20 cores, 256GB of memory, 10Gb and 100Gb EDR interfaces, and 97TB of solid state storage.
- A 36-port EDR 100Gb InfiniBand switch.

The system has been installed in a rack within the main server room in the BU campus and uses the main communication backbone of the room, the redundant power and connectivity. This approach does allow the system to be operational during power line and network maintenance. The system has had 100% availability since the installation and acceptance test were completed at the end of August 2019.

1 – Introduction

Electronics and optoelectronics devices based on semiconductor materials play a crucial role for a variety of applications and in systems currently employed by the Department of Defense (DoD). While the development of silicon electronics has reached a high level of sophistication enabled by well-developed and accurate simulation tools, for other semiconductor material systems the situation is significantly less mature. These advanced simulation tools are necessary to gain insight into new physical phenomena and exploit novel electronic, photonic and spintronic materials to enhance device functionalities and performance. Furthermore, these simulation programs have become invaluable instruments to probe future directions for materials and device development. Many DoD related applications, for example those in the electro-optical area, employ semiconductor materials for which simulation and design tools are much less developed and the technology associated to device fabrication is less understood. This introduces a significant risk in the development process.

These new software tools rely on the availability of modern computer hardware that, with its flexibility and power, has made it possible to tackle complex numerical simulation problems. One of the key issues to be considered is the development of efficient simulation methodologies to investigate physical phenomena at different spatial and temporal scales. Indeed the development of multi-scale simulation methodologies is an area of active research and numerous groups are actively working on this topic. The development of computationally efficient and truly multi-scale simulation methodologies would lead to a unprecedented understanding of materials and devices' properties and ultimately be valuable approach to mitigate technology development risks.

To better understand these risks, Bajaj and co-authors have surveyed the development process of several technologies that are relevant for the ARMY and their transition to systems. They have pointed out that a novel approach is necessary to improve the ability of the science and technology community to develop novel semiconductor devices and transition into specific system applications. Specifically, they emphasized that the timely technology transition with minimal risk requires an understanding of fundamental and technology limitations of material synthesis, device operation and design controllable parameters. However, this knowledge-based approach requires substantial investment of resources in the Science and Technology (S&T) stage of development. For low volume niche semiconductor technologies of DoD relevance, industry alone cannot justify these investments simply because there is no significant return on investment. As a result, technology transition from S&T to product development is often expensive, delayed, and carries risks. To address this challenge, the Computational Electronics Group at Boston University led by Prof. E. Bellotti and a team from the Army Research Laboratory led by Dr. M. Reed have worked to establish the Center for Semiconductor Modeling (CSM). The CSM immediate scientific focus will be to develop robust and predictive models to minimize risk in developing new technology. The CSM will focus on the theory, simulation and the experimental validation of the models.

2 – Scientific and Engineering Achievements Enabled by the Acquired Computational System

The computational platform acquired with the DURIP 2019 funding has enabled the Computational Electronics Group at Boston University to investigate and answer a number of fundamental questions related to semiconductor materials and devices of interested for DoD and the. ARMY in particular.

2.1 Explained the energy gap bowing of $In_{1-x}As_xSb$ alloys.

We have investigate the nature of $InAs_{1-x}Sb_x$ alloys that are important for the design of a variety of infrared detectors. Specifically we have theoretically determined the behavior of the energy gap of these alloys as a function of the composition and shown that it is similar to what was measured by the group of S. Svensson at ARL. We have computed the band gaps and structural properties of $InAs_{1-x}Sb_x$ alloys using both the modified Becke-Johnson exchange potential and hybrid functional calculations. We have found that a good agreement between the two approaches. We have estimated a value of 0.85eV for the bowing parameter enables the use $InAs_{1-x}Sb_x$ in long wavelength infrared (LWIR) applications. Furthermore, we have also obtained a value of 0.29 eV for the bowing parameter is obtained for the structures yielding the largest band gaps, demonstrating the strong nonlinearity of the band gap versus the composition for this system. Figure 1 presents the calculated values of the energy gap.

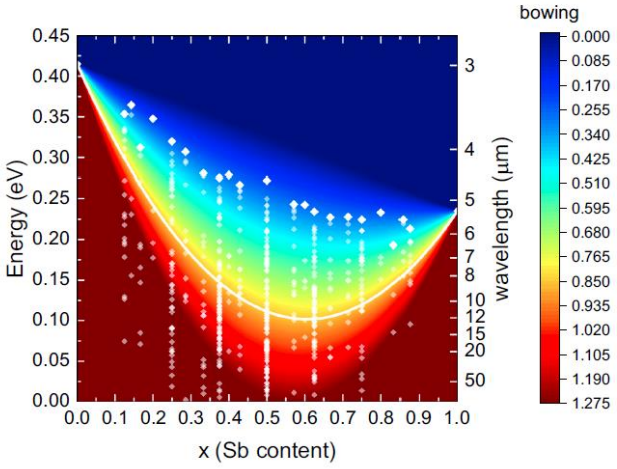

Figure 1 - Band gap values obtained by the PBE- modified Becke-Johnson exchange potential calculations for the different atomic configurations using supercells of up to 16 atoms. The color map illustrates the different bowing parameters as a guide to the eye.

2.2 Determined the band edge offsets of $Al_{1-x}Ga_xN$ alloys.

$Al_xGa_{1-x}N$ alloys are very important for a number of critical applications of interest to the ARMY. Among these, they are used in UV emitters (lasers and light emitting diodes) and detectors for non-line of sight communication, power electronics devices for electric vehicles. The knowledge of the band edge (valence and conduction) offsets is critical to the device design. We have used first-principles calculations to study of the band offsets of $Al_xGa_{1-x}N$ alloys, taking into account

their composition and atomic configuration. Specifically, the band offsets are obtained using PBE, PBEsol, Heyd, Scuseria, and Ernzerhof (HSE), and modified Becke–Johnson calculations, comparing the results and discussing the advantages and disadvantages of each functional. The band alignments are performed using the branch point energies of the materials as their common reference level. HSE calculations predict a valence band offset of 0.9 eV between GaN and AlN. Regarding the alloys, a conduction band edge bowing parameter of 0.55 eV and a practically zero bowing for the valence band edge is predicted on average. The different atomic configurations affect mainly the valence band edges, where deviations from linearity by more than 0.1 eV are observed. Figure 2 presents a summary of the calculated values of the band edge offsetts.

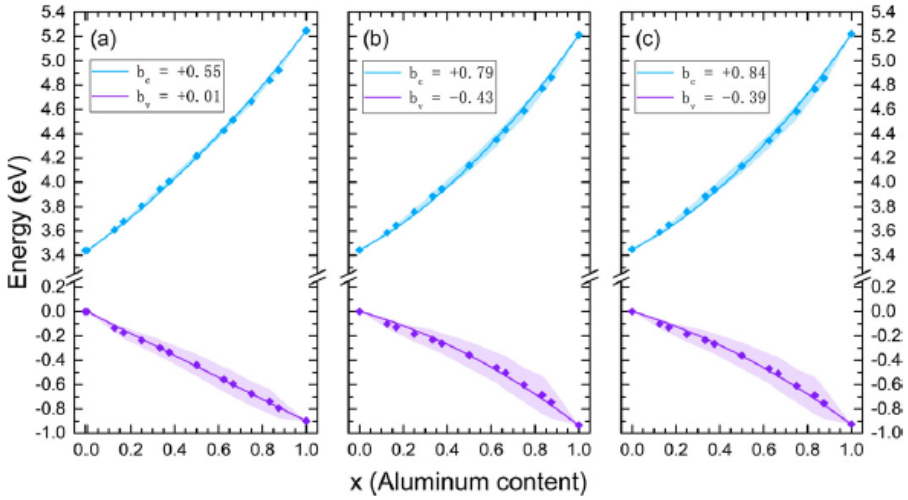

Figure 2 - The band offsets of the alloys obtained by (a) HSE calculations, as well as mBJ calculations with (b) an optimal and (c) a species-specific *c* parameter. The legends indicate the bowing parameter of the valence and conduction band edges. The valence band edge of GaN is set to 0 eV for convenience.

2.3 Explained the nature of carrier transport in LWIR Type-II Superlattices.

Type-II superlattices are of critical importance for the new generation of high temperature infrered detectors. In spite of the initial promising results, a number of issues are still holding back strain-balanced InAs/$In_xAs_{1-x}Sb$ T2SLs from achieving their full potential. While in the MWIR spectral region, imaging devices based on InAs/$In_xAs_{1-x}Sb$ T2SLs T2SLs have delivers performance comparable to conventional indium antimonide cameras, but at higher operating temperatures, for the LWIR spectral band, a number of problems still remain. Specifically, the reduction of the operating temperature, necessary to reduce noise, results in a degraded quantum efficiency (QE) due to incomplete carrier collection. Conversely, higher operating temperatures, where QE is higher, lead to excessive dark current that degrade the image quality. QE degradation at low temperature is likely the results of a combination of degraded mobility and/or recombination processes. In fact, based on recent experimental investigations, carrier (holes in particular) mobility in T2SLs decreases with temperature, instead of increasing, and it is strongly anisotropic. This behavior is typical of hopping conduction rather than diffusive transport. Moreover, the anisotropic transport properties, namely the large different of carrier mobility in the directions parallel and perpendicular to the growth axis, also lead to a degradation of the modulation transfer

function (MTF) of the imaging array, resulting in a compromised image quality and resolution.

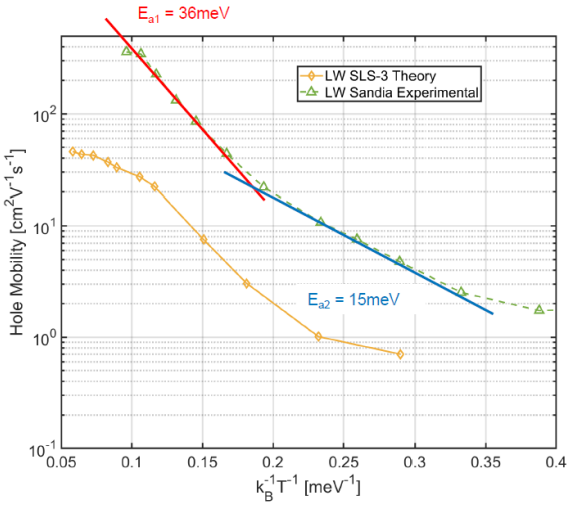

Figure 3(a) – Calculated hole mobility as a function of the temperature (yellow line). Measured hole mobility for a similar LWIR Type-II SLS (green line).

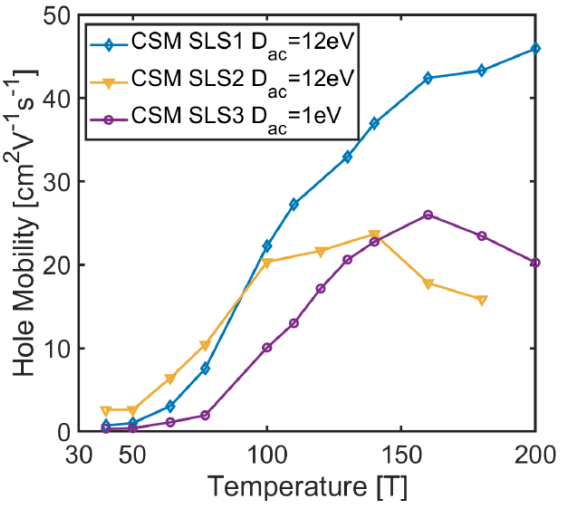

Figure 3(b) – Calculated hole mobility as a function of the temperature for three different random SLS configurations.

We have shown that the presence of disorder, regardless its nature and cause, introduces fundamental limitations to the vertical carrier transport properties of gallium free strained balanced $InAs/In_xAs_{1-x}Sb$ type-II superlattices. These limitations become particularly severe at low operating temperature that are normally required to reduce noise and dark current. Furthermore, when holes are the minority carrier that contribute to the device photocurrent, the degradation of their transport coefficient is so dramatic that the operation of detector may be compromised. Figure 3(a) and (b) presents a summary of the calculated values of hole mobility and a comparison with experimental data.

3 - Hardware Acquisition

Because of the experience gained with the computational system that was built using the funding from FY2014 DURIP, we performed extensive benchmarks on the various architectures to identify the best platform for a given specific task. We considered both our current production computing system and other computational platform such has the DoD HPC that we have been using because of our involvement in the Army Research Laboratory (ARL) Multi-scale Electronic Material Simulation (MSME) Collaborative Research Alliance (CRA). Based on performance evaluations of the systems acquired using the 2014 DURIP program, four specific criteria were used to determine the type of computational architectures targeted for acquisition, which are listed below:

- Use only on type of machines for all nodes, including file servers. Instead of focusing on specific processor configuration, large number of cores or speed, we have selected the best performance type of processor that can be used in all applications. We have selected node configurations with two Intel Xeon Gold 6248 20C/40T 2.5Ghz.

- Maximize the amount of memory in each node. Each node 768GB of memory except for two that have 1.5TB.

- Use highest performance interconnect. Specifically, we have selected a redundant 10Gb Ethernet for NFS and a 100Gb EDR InfiniBand for MPI applications.

- Use a high speed storage to minimize the IO time. We have acquired a SSD disk arrays with a total capacity of 97TB.

We have also designed the overall system to be integrated with existing backup facilities and in such a way that power and connectivity redundancy are provided by existing infrastructure at Boston University.

The final hardware that was acquired in composed of:
- Ten nodes with two Intel Xeon Gold 6248 processors, each with 20 cores, 768GB of memory, 10Gb and 100Gb EDR interfaces.
- Two nodes with two Intel Xeon Gold 6248 processors, each with 20 cores, 1.5TB of memory, 10Gb and 100Gb EDR interfaces.
- A file server with two Intel Xeon Gold 6248 processors, each with 20 cores, 256GB of memory, 10Gb and 100Gb EDR interfaces, and 97TB of solid state storage.
- A 36-port EDR 100Gb InfiniBand switch.

The system has been installed in a rack within the main server room in the BU campus and uses the main communication backbone of the room, the redundant power and connectivity. This approach does allow the system to be operational during power line and network maintenance. The system has had 100% availability since the installation and acceptance test were completed at the end of August 2019.

Figure 4(a) and 4(b) show the system as it is installed in the rack. The 36-port EDR 100Gb InfiniBand switch has been placed in the middle with six servers above and six below. The file server is at the top of the stack. The Ethernet switches are located at the top of the rack and provide redundant connectivity.

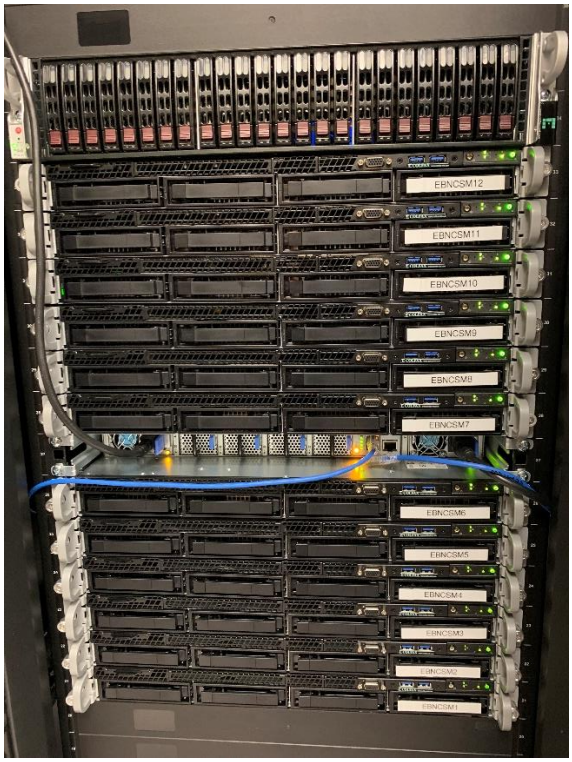

Figure-4(a) Front view of the cluster installed in the rack. Form the top we have: the file server, six compute nodes, the EDR 100Gb InfiniBand switch, and six more computer nodes.

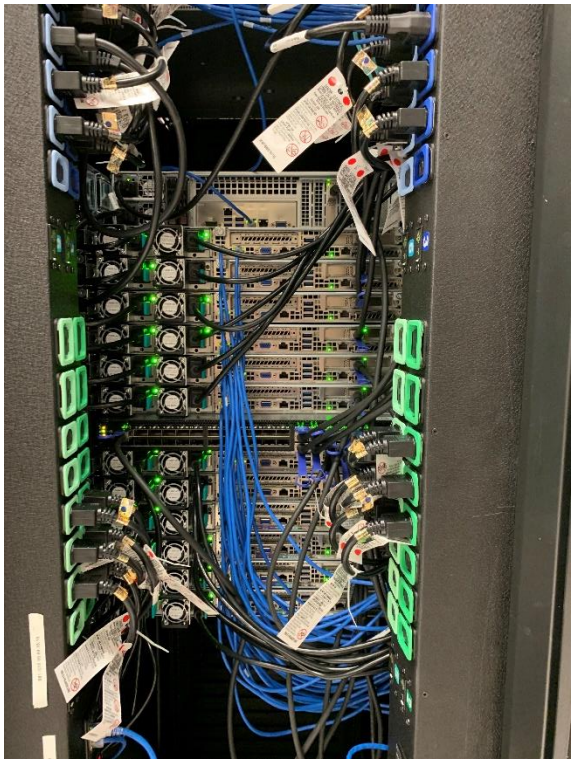

Figure-5(b) Rear view of the cluster installed in the rack. The blue cables are for the 10Gb Ethernet, the black cable on the right of the servers are for the EDR InfiniBand.

4 – Performance Evaluation for Selected Software Applications

The computing cluster acquired using DURIP-2019 has been connected to shared Boston University resources to enable access to a wide variety of software. We have carried out an extensive performance evaluation and compared the results with other computing platforms including the DoD HPC resources that we have access to. We will show the scaling results across different computational architectures from four software packages used routinely in our research: **VASP** density functional theory (DFT) for evaluating the electronic structure of semiconducting materials. **EPW** a code that computes carrier-phonon interaction starting from DFT calculations. **Synopsys EMW**, a finite difference time domain for electromagnetic scattering and absorption, and **Synopsys SDEVICE** for finite element solutions of the drift-diffusion semiconductor device equations. These applications have been chosen as they cover wide spatial scales, from the quantum to classical, and demonstrate the needs of multi-scale simulation hierarchies.

4.1 - Density Functional Theory Benchmark

For the DFT benchmark, we have compared sever different computing platforms:

1. The new system obtained by FY19 DURIP award
    a. 12 nodes (10 nodes with 768 GB memory + 2 nodes with 1.5 TB memory)
    b. CPU: 40 cores Intel Xeon Gold 6248 (Cascade Lake) 2.50 GHz
    c. Memory: DDR4-2933 768 GB/1.5 TB
    d. Interconnect: Infiniband EDR 100 Gbps

2. DoD HPC Cray XE6m system (Copper)
    a. 460 nodes
    b. CPU: 32 cores AMD Interlagos Opteron 2.30 GHz
    c. Memory: DDR3 64 GB
    d. Interconnect: Cray Gemini

3. DoD HPC Cray XC40 system (Gordon)
    a. 1,523 nodes
    b. CPU: 32 cores Intel Xeon E5-2698v3 (Haswell-EP) 2.30 GHz
    c. Memory: DDR3 128 GB
    d. Interconnect: Cray Aries / Dragonfly

4. DoD HPC Cray XC40/50 system (Onyx)
    a. 4,810 nodes
    b. CPU: 44 cores Intel Xeon E5-2699v4 (Broadwell) 2.80 GHz
    c. Memory: DDR4 128 GB
    d. Interconnect: Cray Aries

5. DoD HPC SGI 8600 system (Gaffney)
    a. 704 nodes
    b. CPU: 48 cores Intel Xeon Platinum 8168 (Skylake) 2.70 GHz
    c. Memory: DDR4 192 GB
    d. Interconnect: Intel Omni-Path

6. BU Cluster of three servers obtained in 2018
    a. 3 nodes
    b. CPU: 44 cores Intel Xeon E5-2699Av4 (Broadwell) 2.40 GHz
    c. Memory: DDR3 256 GB
    d. Interconnect: Infiniband FDR 40 Gbps

7. BU Cluster subsystem obtained by FY14 DURIP award
    a. 4 nodes
    b. CPU: 20 cores Intel Xeon E5-2690 v2 (Ivy Bridge-EP) 3.00GHz
    c. Memory: DDR3 256 GB
    d. Interconnect: Infiniband FDR 40 Gbps

4.1.2 - Scaling of VASP – Electronic Structure Calculation Code

We have analyzed both raw speed and scaling for the platform above using VASP. The latest version (version 5.4.4, patch.5.4.4.16052018 was applied) of VASP was used. Two different model systems were used for the tests that were performed:

1. A carbon doped GaN system with 96 atoms (48 Ga, 47 N and 1 C atoms), 8 k-points, at least 565 bands and 3 ionic steps in PBE functional.

2. A carbon doped GaN system with 192 atoms (96 Ga, 95 N and 1 C atoms), 4 k-points, at least 1140 bands and 5 ionic steps in PBE functional.

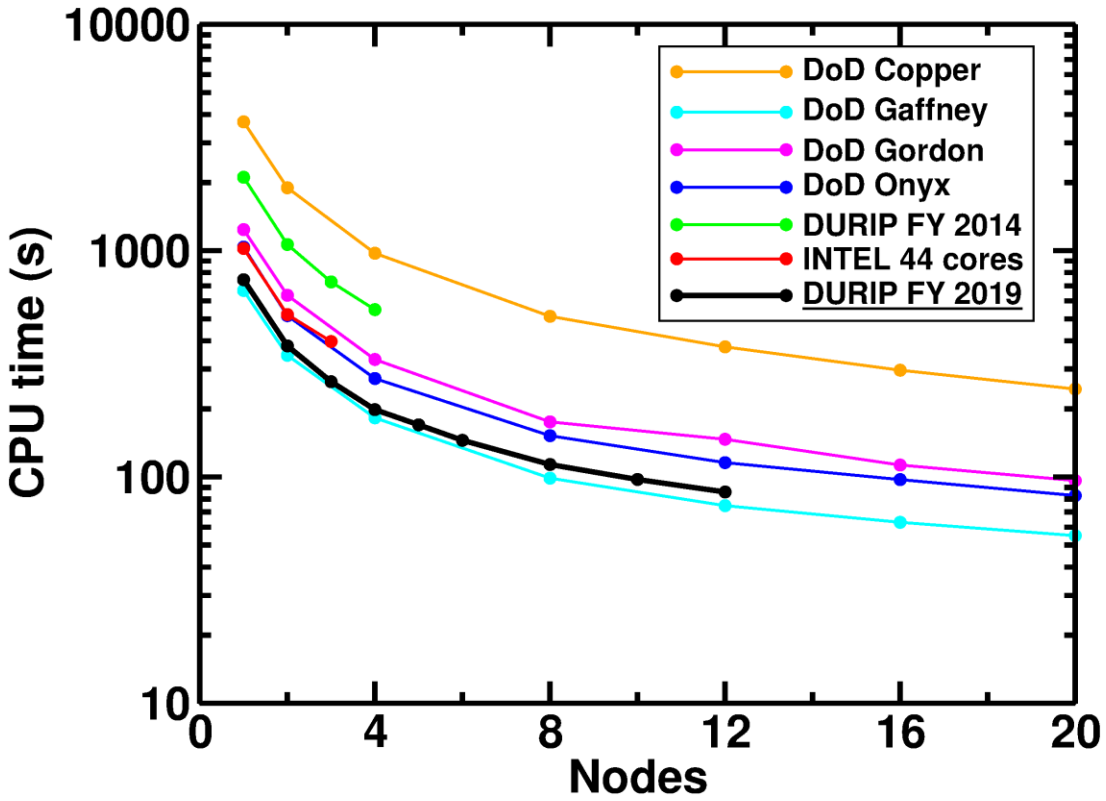

Figure 5 – Execution speed for a 96 atom system. Speed up in CPU time (in seconds) with increasing the number of nodes.

Figure 5 is for the raw speed of the calculations. The new system obtained by DURIP FY 2019 (black solid line) shows the speed almost as good as one of the fastest machine (Gaffney, ranked 123rd in the supercomputer 500 list, light blue solid line) among the DoD HPC supercomputers.

Table 1 - Execution speed for a 96 atom system. CPU time (in second) with increasing number of nodes.

Nodes	DURIP FY 2019	Gaffney	Gordon	Onyx
1	744.094	667.424	1240.130	1037.536
2	379.708	344.945	635.192	516.568
4	198.449	182.657	330.665	272.492
8	113.573	98.844	175.139	152.304
12	85.866	74.675	146.797	115.816

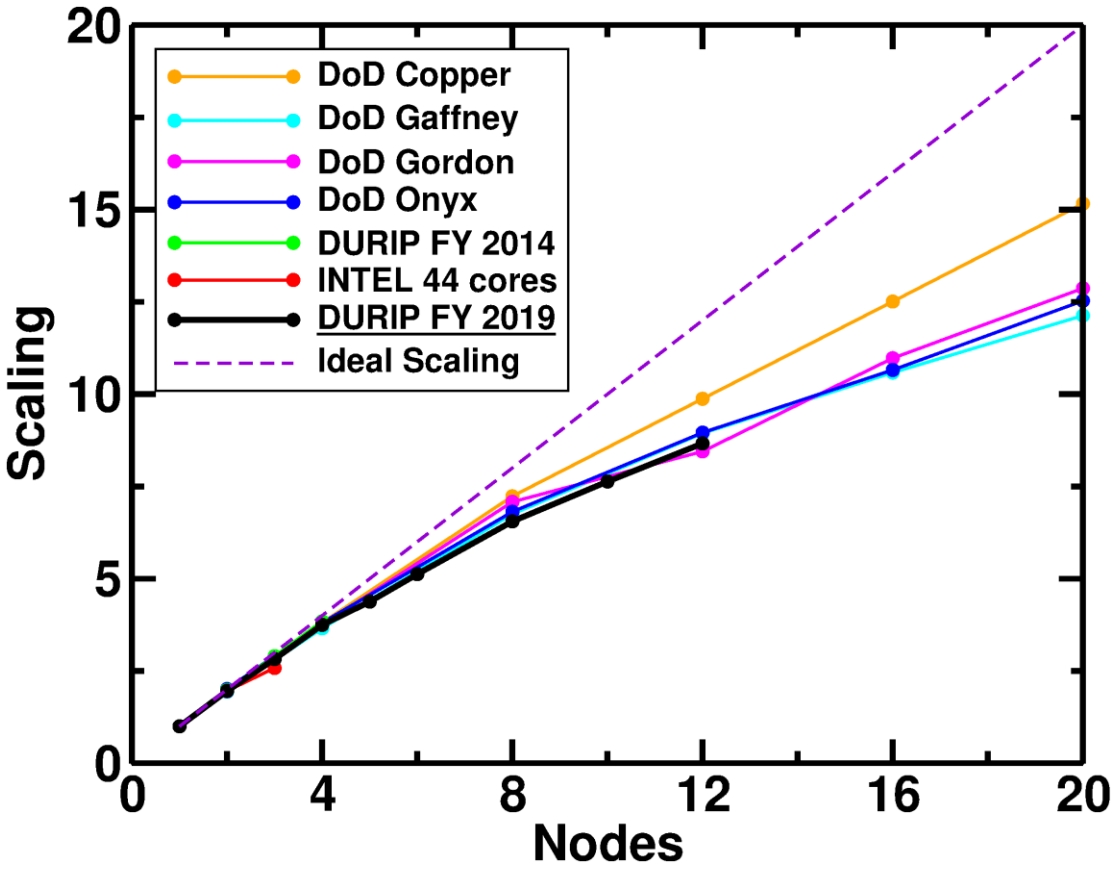

Figure 6 – Scaling for a 96 atom system with increasing the number of nodes.

Figure 6 presents the results for scaling as a function of the number of nodes. All systems show relatively good scaling. Copper shows the best scaling, but, as can be seen in Figure 2, it is in general much slower than other systems. All other systems show very similar scaling performance.

Table 2: Scaling for a 96 atoms system. Scaling with increasing the number of nodes.

Nodes	DURIP FY 2019	Gaffney	Gordon	Onyx
1	1	1	1	1
2	1.96	1.93	1.95	2.01
4	3.75	3.65	3.75	3.81
8	6.55	6.75	7.08	6.81
12	8.67	8.94	8.45	8.96

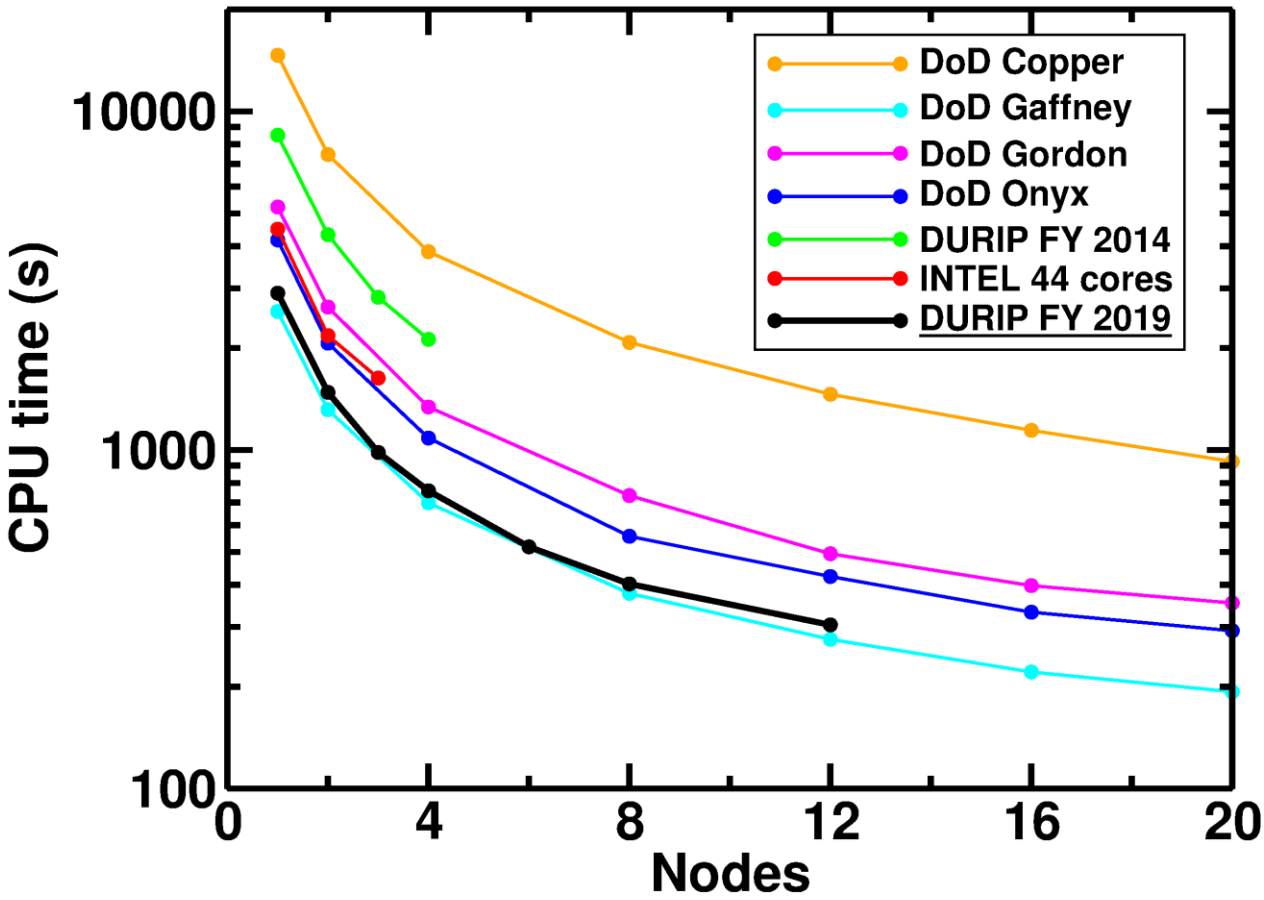

Figure 7 – Execution speed 192 atom system. Speed up in CPU time (in seconds) with increasing the number of nodes

Figure 7 presents the raw execution speed for 192 atom system. Once again, the new system obtained by DURIP FY 2019 shows the speed almost as good as Gaffney.

Table 3: 192 atom system. CPU time (in second) with increasing number of nodes.

Nodes	DURIP FY 2019	Gaffney	Gordon	Onyx
1	2905.523	2565.254	5217.710	4170.904
2	1479.933	1315.357	2643.105	2067.860
4	758.022	697.890	1340.120	1084.784
8	402.263	377.208	733.762	556.052
12	304.535	275.964	493.727	423.124

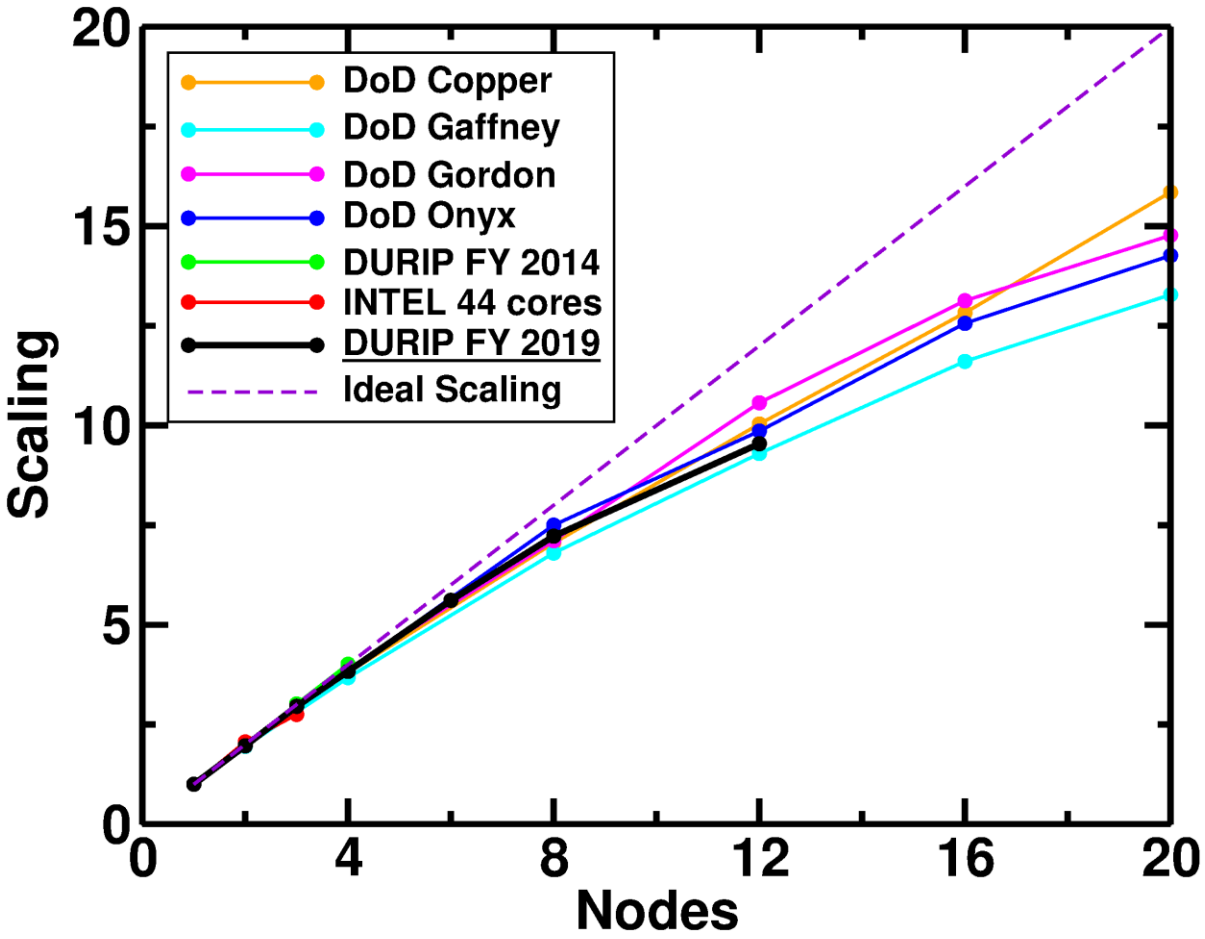

Figure 8 – Scaling for a 192 atom system with increasing the number of nodes.

Figure 8 presents the scaling results for a 192 atom system. All systems show relatively good scaling, but Gaffney's scaling is not as good as other systems. Cray's interconnect (Gemini in Copper and Aries in Gordon and Onyx) shows slightly better scaling behavior, compared to the scaling of Infiniband EDR used in the new system obtained by DURIP 2019. Also, Cray's

interconnect and Infiniband EDR shows improved scaling in 192 atoms system comparing to 96 atoms system, whereas the scaling of Intel Omni-Path in 96 atoms system and 192 atoms system are almost the same.

Table 4: 192 atoms system. Scaling with increasing the number of nodes.

Nodes	DURIP FY 2019	Gaffney	Gordon	Onyx
1	1	1	1	1
2	1.96	1.95	1.97	2.02
4	3.83	3.68	3.89	3.84
8	7.22	6.80	7.11	7.50
12	9.54	9.30	10.57	9.86

4.1.3 Scaling of EPW – Carrier-Phonon Interaction Calculation Code

We have analyzed both raw speed and scaling for the platform above using EPW version 5.0.0 included in Quantum Espresso version 6.3. Electron self-energies of GaN due to the electron-phonon interactions were computed with very coarse 25x25x25 k- and q-point meshes.

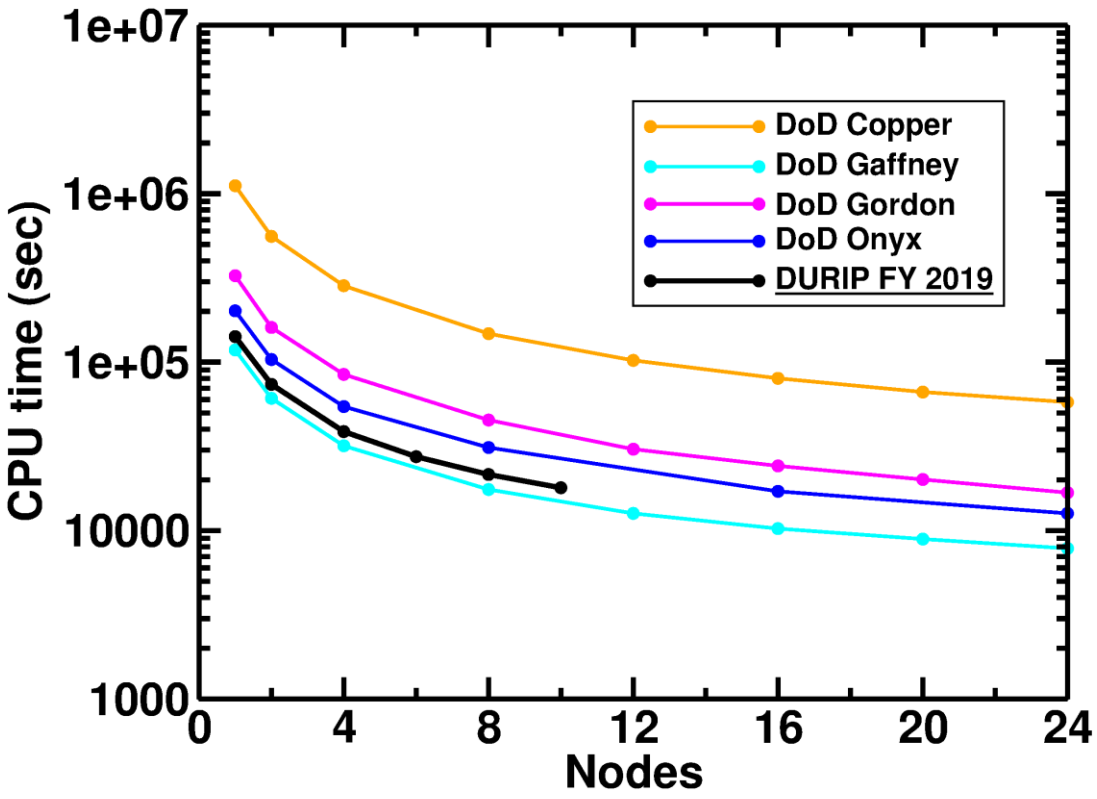

Figure 9 - EPW calculations. Speed up in CPU time (in seconds) with increasing the number of nodes.

Figure 9 presents the raw speedup for the EPW calculations. Again, the new system obtained by DURIP FY 2019 shows the speed almost as good as Gaffney. The speed of the new system with 8 nodes (21532.95 seconds) is almost the same as that of Gordon with 16 nodes (24209.11 seconds). In addition, the speed of the new system with 10 nodes (17955.63 seconds) is almost the same as that of Onyx with 16 nodes (17093.23 seconds).

Table 5: EPW calculations. CPU time (in second) with increasing number of nodes.

Nodes	DURIP FY 2019	Gaffney	Gordon	Onyx
1	14710.43	118078.04	325549.35	201538.44
2	73712.99	60934.16	160656.61	103652.63
4	38728.59	31874.25	84545.72	54462.00
8	21532.95	17524.65	45301.71	31111.68
10	17955.63	--	--	--
12	--	12650.40	30424.40	--
16	--	10265.56	24209.11	17093.23

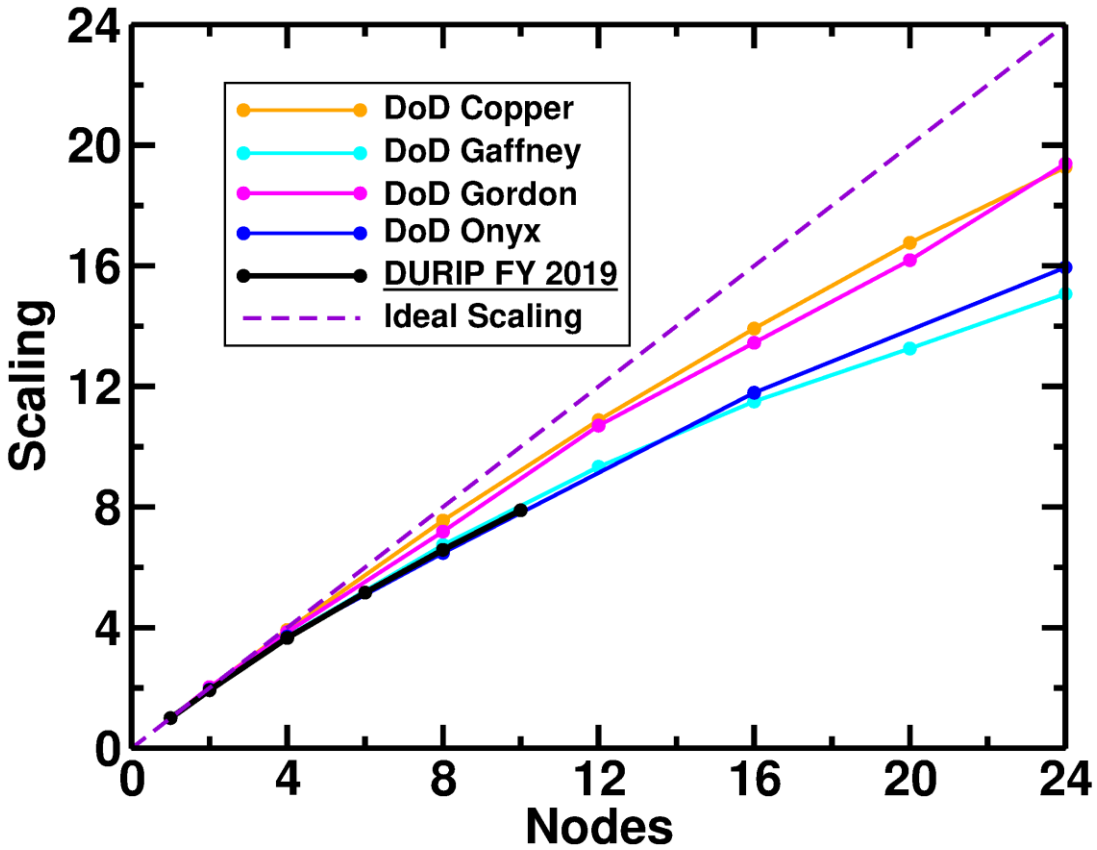

Figure 10 - EPW calculations. Scaling with increasing the number of nodes.

Figure 10 presents the scaling results for the EPW calcualtion. Copper and Gordon show similar and better scaling and Gaffney, Onyx and the new system obtained by DURIP FY 2019 show similar and worse scaling. It is not clear why there is difference between Gordon and Onyx (both

systems use Cray's Aries interconnect). In general, Cray's interconnect (Gemini in Copper and Aries in Gordon and Onyx) shows slightly better scaling behavior, comparing to the scaling of Infiniband EDR used in the new system obtained by DURIP 2019. This is the same trend as in the case of VASP calculations.

Table 6: EPW calculations. Scaling with increasing the number of nodes.

Nodes	DURIP FY 2019	Gaffney	Gordon	Onyx
1	1	1	1	1
2	1.92	1.94	2.03	1.94
4	3.66	3.70	3.85	3.70
8	6.58	6.74	7.19	6.48
10	7.89	--	--	--
12	--	9.33	10.70	--
16	--	11.50	13.45	11.79

The new system obtained by DURIP FY 2019 award shows the speed almost as good as the fastest machine (Gaffney, ranked 123rd in the supercomputer 500 list) among the DoD supercomputers. In addition, the new system shows the same (EPW) or slightly better scaling (VASP) than Gaffney with increasing the number of nodes.

4.2 - Finite Difference Time Domain

The Computational Electronics group frequently uses the finite-difference time domain (FDTD) method (implemented in Synopsys EMW) to determine the electromagnetic response of optoelectronic devices. The FDTD method uses a direct-time approach to solve Maxwell's curl equations by splitting them into three scalar partial differential equations and replacing the partial derivatives with first order central differences. The result is a set of six algebraic update equations at each spatial point on a structured grid. The update equations are used with a time-stepping algorithm to propagate a solution through a simulation domain. The efficiency of the FDTD algorithm is directly related to the computational mesh; an update equation must be solved at each grid point the FDTD method is therefore O(N) where N is the number of points in the grid. Furthermore, a physical steady-state solution must causally link one side of the domain to the other causing additional scaling with n_{tot}, the number of time steps. In three-dimensional simulations, it is assumed that n_{tot} is proportional to the third root of the mesh size causing overall $O(N^{4/3})$. Figure 8 shows the wall clock time required for a steady-state solution as a function of the number of cores used. Since the Synopsys EMW code is based on a share memory-programming model, it is only possible to perform a test on a single node of the cluster. Figure 12 presents the speedup performance for a steady-state solution as a function of the number of cores used.

4.3 - Finite Element Drift Diffusion Code

We have performed a similar analysis of the scaling of the finite element method (FEM) used for solving the drift-diffusion formulation of the semiconductor device equations, the results of which are shown in Figure 11 and 12. Unlike the previous FDTD simulations, the FEM method uses an unstructured mesh, which must be carefully designed with consideration of the physics of the

device. In general, the computational requirements (both CPU hours and memory) scale linearly with the size of the domain, but there is some problem-to-problem variation depending on the specific physics of the device under consideration.

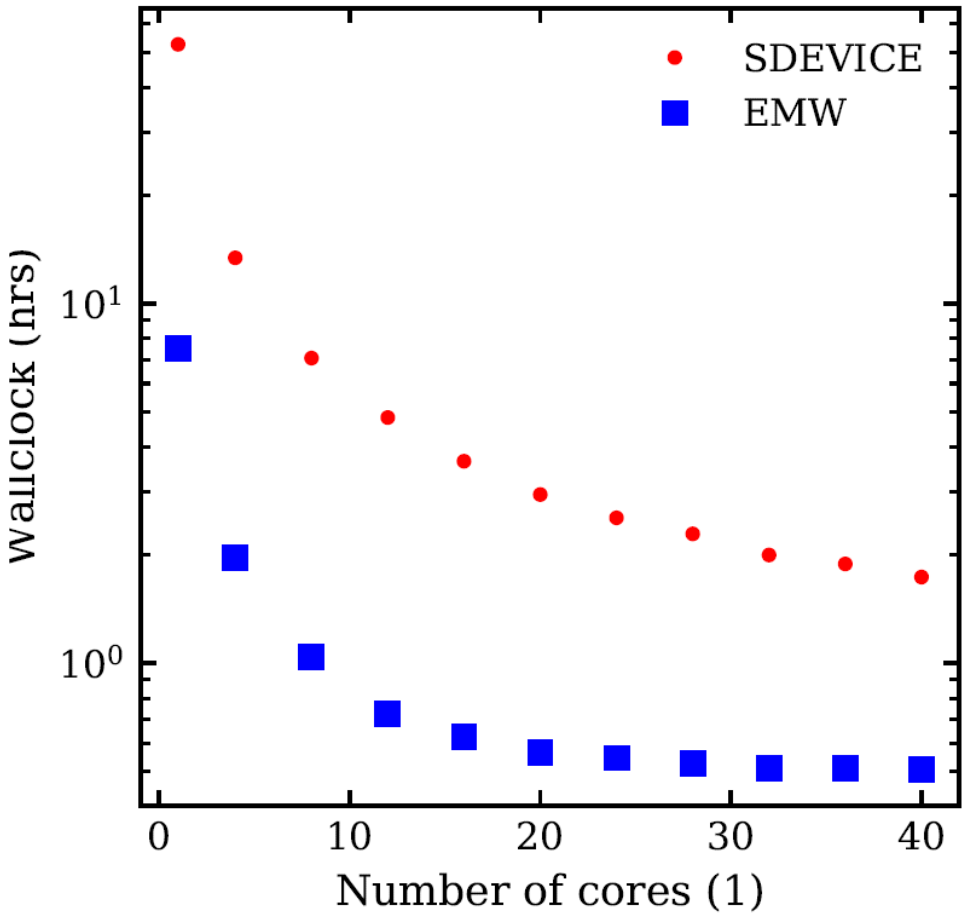

Figure 11 - Wall clock time required for a steady-state solution as a function of the number of cores used.

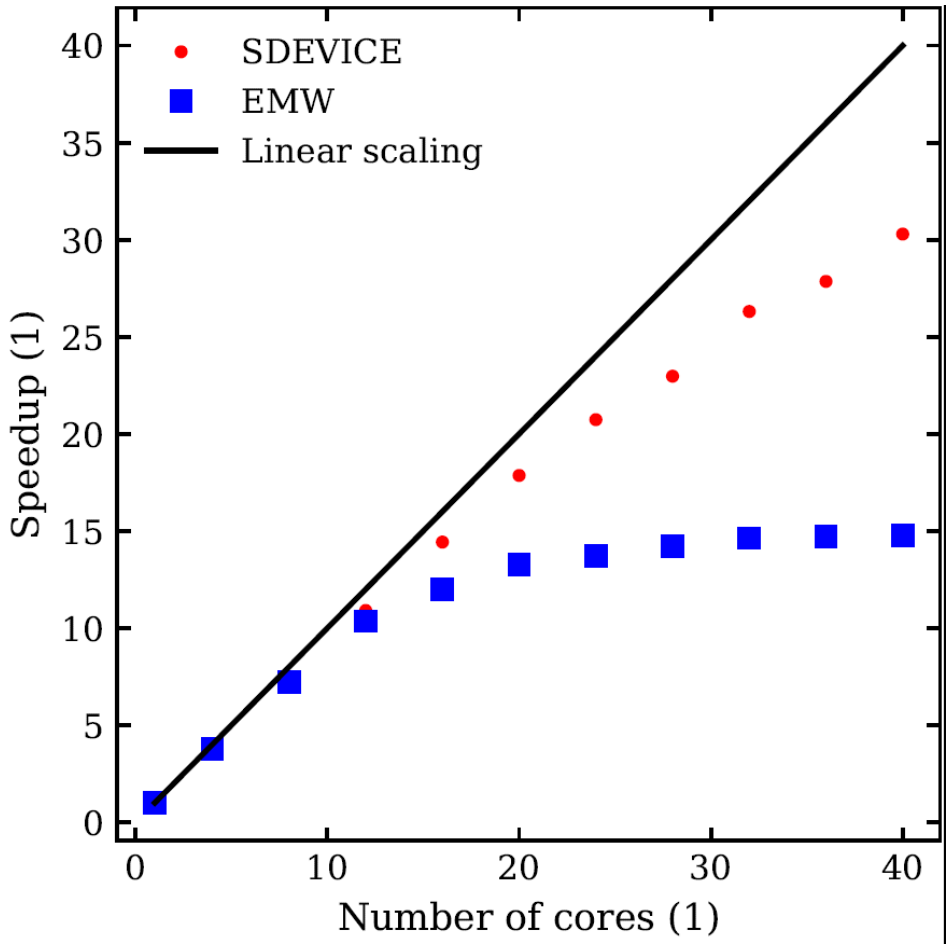

Figure 12 - Speedup performance for a steady-state solution as a function of the number of cores used.

5 - Educational Activity

The equipment purchased through the 2019 DURIP award to the Boston University Computational Electronics group has supported the ongoing research activities of two post-doctoral associates and five PhD students actively involved in DoD funded programs. Besides supporting their ongoing research, the acquisition of the new computational resources provided impetus to investigate the development of computationally efficient software. For example, the increasing availability of machine time across the cluster led to the use of MPI and OpenMP to distribute programs across a number of physically separate compute nodes. These techniques have been integrated into existing software. Additionally, having removed the machine availability bottleneck, a significant effort was devoted towards developing codes and methods for automating designs to increase overall throughput. The students have also been able to present their work at several high-profile conferences (SPIE Photonics West, Defense, Security + Sensing, Optics and Photonics) where it is possible to engage researchers from various DoD organizations.

6 – Publications Supported by 2019 DURIP Program

The following DoD funded publications have been supported in part by the equipment purchased through the 2019 DURIP award to the Boston University Computational Electronics Group:

5.1 Manuscripts Published

1 - A. Kyrtsos, M. Matsubara, and E. Bellotti, Investigation of the band gaps and bowing parameter of $InAs_{1-x}Sb_x$ alloys using the modified Becke-Johnson potential, *Phys. Rev. Materials,* Vol.4 No.1 Article Number: 014603, January 8 2020.

2 - A. Kyrtsos, M. Matsubara, and E. Bellotti, Band offsets of $Al_xGa_{1-x}N$ alloys using first-principles calculations, *J. Phys. Condens. Matter*, Vol. 32, p.365504, May 2020

3 - F. Bertazzi, A. Tibaldi, J.A.G. Montoya, M. Goano, E. Bellotti, Non-equilibrium Green's function modeling of type-II superlattice detectors and its connection to semiclassical approaches, *Phys. Rev. Applied,* Accepted 29 June, 2020.

5.2 – Conference Papers and Presentation

1 - E. Bellotti, F. Bertazzi, J. Bajaj, J. Schuster, M. Reed Understanding Fundamental Material Limitations to Enable Advanced Detector Design, NUSOD 2019, Invited Talk, conference paper at https://ieeexplore.ieee.org/abstract/document/8807083.

5.3 - Manuscripts under review

1 – S.P. Svensson, W.L. Sarney,W.A. Beck,J. Liu, D. Donetsky, S. Suchalkin, G. Belenky, A. Kyrtsos, and E. Bellotti, P-doping with Beryllium of long-wavelength InAsSb, *Semiconductor Science and Technology*, under review

2 – A. Glasmann, A. Kyrtsos, and E. Bellotti, Machine learning for analyzing and characterizing InAsSb-based nBn photodetectors, *Phys. Rev. Applied,* under review.

Investigation of the band gaps and bowing parameter of $InAs_{1-x}Sb_x$ alloys using the modified Becke-Johnson potential

Alexandros Kyrtsos,[1,*] Masahiko Matsubara,[1] and Enrico Bellotti[1,2]
[1]*Department of Electrical and Computer Engineering, Boston University, Boston, Massachusetts 02215, USA*
[2]*Division of Materials Science and Engineering, Boston University, Boston, Massachusetts 02215, USA*

(Received 4 September 2019; revised manuscript received 10 December 2019; published 8 January 2020)

The band gaps and structural properties of $InAs_{1-x}Sb_x$ alloys are investigated using both the modified Becke-Johnson exchange potential and hybrid functional calculations. A good agreement between the two approaches is observed for the alloys. The estimated value of 0.85 eV for the bowing parameter enables the use of InAsSb in long wavelength infrared (LWIR) applications. Furthermore, a lower limit of 0.29 eV for the bowing parameter is obtained for the structures yielding the largest band gaps, demonstrating the strong nonlinearity of the band gap versus the composition for this system.

DOI: 10.1103/PhysRevMaterials.4.014603

I. INTRODUCTION

The alloys of InAs and InSb exhibit the smallest band gaps among all III-V semiconductors [1], attracting attention both for fundamental research and relevant applications. Specifically, the pure phases of InAs and InSb exhibit band gaps of 0.415 and 0.235 eV, respectively, while their ternary alloys demonstrate strong positive (downward) band gap bowing [2,3]. $InAs_{0.91}Sb_{0.09}$ can be grown lattice matched to GaSb [4], enabling this material to be used in mid-wavelength infrared (MWIR, i.e., 3–5 μm) applications [5]. However, reaching even longer wavelengths requires significantly lower band gaps. Although the use of InAsSb in long wavelength infrared (LWIR, i.e., 8–12 μm) optoelectronic applications is of particular importance and has been discussed in literature for decades [6–8], the adaptation of this material for such applications has met with limited success. The main reasons for that are the widely accepted values of the band gap bowing parameter which do not predict the absorption wavelength to be adequately long and the absence of high quality substrates which enable the epitaxial growth of the material at relevant compositions [6].

Regarding the absence of suitable substrates, a typical approach has been the use of thick monolithic buffer layers that allow the relaxation through threading and misfit dislocations. In order to minimize the vertical propagation of the mismatch related defects into the active region, various techniques such as grading schemes [9,10] and blocking layers [11] have been developed. These techniques are successful in greatly reducing the defect densities but lead to some residual strain which affects the band gap and other optical properties of the material [5,6]. Over the last few years, further improvements to the quality of the samples has been achieved by the combination of compositional grading and a virtual substrate (VS) with the interfacial misfit (IMF) approach [5,6,12–14], resulting in unrelaxed and unstrained materials with inherent lattice constants and band gaps.

Early experimental data by Yen *et al.* [3] on samples grown on InAs substrates by molecular beam epitaxy indicated a bowing parameter of 0.685 eV. Later, Fang *et al.* [2] reported data on samples grown using organometalic vapor phase epitaxy on InAs substrates in which the bowing parameter was 0.672 eV. Such values for the bowing parameter are prohibitively small for LWIR applications. However, in a second paper by Yen *et al.* [15], the authors reported a photoluminescence peak at 10 μm for a sample of $InAs_{0.39}Sb_{0.61}$ grown on GaAs substrate. Furthermore, the development of methods to produce high quality substrates has led to materials with reduced band gaps [6,13] where the bowing parameter reaches 0.87 eV, thus enabling the use of InAsSb as a lower cost, III-V alternative to HgCdTe, which is currently primarily used in LWIR applications.

Compared to binary compounds, ternary alloys introduce an additional degree of freedom which is the atomic configuration of each structure at any given composition. The atomic configuration is known to affect the physical properties of the material significantly. Nonetheless, the numerous different configurations render the theoretical investigation of ternary systems more challenging and computationally expensive. The alloys are typically treated theoretically using either the virtual crystal approximation (VCA) [16,17] or the coherent potential approximation (CPA) [18–21]. These approaches, though, impose an artificially high symmetry and are unable to describe the effects of the local atomic environment in alloys. Even though the InAsSb system has been studied theoretically in the past using both first principles [22] and empirical pseudopotentials [23,24], a comprehensive theoretical study of the band gap dependence on composition taking into account the atomic configuration is still missing. The aim of this work is to employ first-principles calculations in the context of both standard and hybrid density functional theory (DFT) [25,26] in order to study the band gaps of the InAsSb system with respect to its stoichiometry and atomic configuration.

*akyrtsos@bu.edu

II. METHOD

Our DFT calculations employ the projector augmented wave (PAW) [27,28] method as implemented in the Vienna *ab initio* simulation package (VASP) [29]. Both standard and hybrid functional approaches were used for the treatment of the exchange-correlation (xc) energy. In the former case, the generalized gradient approximation (GGA) in the flavors of PBE [30,31] and PBEsol [32] was used. One of the known shortcomings of standard DFT is the underestimation of the band gap [33], which becomes particularly important in narrow gap systems where standard DFT produces even negative band gaps. A common approach for improving the description of the band gap along the standard DFT scheme is the use of meta-GGA functionals. In this work we employ the Tran-Blaha modified Becke-Johnson (mBJ) [34,35] meta-GGA functional, which is able to produce band gaps with an accuracy similar to hybrid functional or *GW* calculations and very good agreement with experimental data [36,37]. A species dependent c parameter was used for the mBJ calculations with a value of 1.220, 1.139, and 1.226 for In, As, and Sb, respectively, in order to reproduce the experimental band gaps of the pure phases.

Hybrid functional calculations were performed using the parametrization introduced by Heyd, Scuseria, and Ernzerhof (HSE) [38,39] in order to compare the results to the ones obtained by the semilocal approach. In the case of the HSE calculations we employed a composition dependent mixing parameter for the Hartree-Fock exchange, which changes linearly from $a = 0.286$ for pure InAs ($x = 0$) to $a = 0.264$ for pure InSb ($x = 1$). The use of a variable mixing parameter for the study of the electronic properties of different materials relies on the fact that the reference levels used for the alignment of the energy eigenvalues of each system are not dependent on the mixing parameter [40,41]. In this work the vacuum level and the average electrostatic potential obtained by slab calculations were used to verify this condition.

The different atomic configurations were generated using the ATAT code [42,43]. Supercells of up to 16 atoms were investigated, yielding 692 distinct atomic configurations. A cutoff energy of 350 eV was used for the plane-wave basis set and the Brillouin zone was sampled using Γ-centered k meshes with a density of 1000 k points per reciprocal atom. In the case of the GGA calculations the volume of each supercell was optimized with a force criterion of 10^{-2} eV/Å. Further atomic-only relaxations were performed with a criterion of 10^{-3} eV/Å. In the case of the HSE calculations, the force criterion for the volume and atomic relaxations was set to 10^{-2} eV/Å. Furthermore, the indium $3d$ electrons were treated as valence electrons and spin-orbit coupling (SOC) was taken into account for the band gap calculations in both cases. Finally, in order to reduce the computational cost of the HSE calculations, a subset of 290 configurations was used and the PBEsol structures were used as a starting point for the atomic relaxations.

III. RESULTS AND DISCUSSION

The crystallographic parameters of zincblende InAs and InSb were obtained using both the PBEsol and HSE functionals. In the case of InAs the lattice constant obtained from the PBEsol and HSE calculations was 6.083 and 6.084 Å, respectively, while for InSb the obtained lattice constant was 6.513 and 6.509 Å. Compared to the experimental lattice constants of 6.058 and 6.479 Å for InAs and InSb, respectively [44], the calculations overestimate the values by approximately 0.5%, indicating an excellent agreement for both functionals. Table I summarizes the results, including the band gaps obtained by GGA and HSE calculations, where GGA refers to the mBJ coupled PBE calculations (PBEmBJ), in structures optimized with the PBEsol functional.

TABLE I. Crystallographic parameters and band gaps of InAs and InSb obtained by the GGA and HSE calculations. The GGA lattice constants are obtained by the PBEsol functional while the band gaps are obtained by the PBEmBJ functional.

	Method	a (Å)	E_g (eV)
InAs	GGA	6.083	0.415
	HSE	6.084	0.415
	Expt.	6.058[a]	0.415[b]
InSb	GGA	6.513	0.235
	HSE	6.509	0.236
	Expt.	6.479[a]	0.235[b]

[a]Reference [44].
[b]Reference [2].

In a solid solution following Vegard's law [45], the lattice constant changes linearly between the two constituents according to the rule of mixtures. In order to assess the agreement with Vegard's law, the lattice constants of the InAsSb alloys for different compositions are presented in Fig. 1, both for PBEsol and HSE calculations. A straight line connecting the lattice constants of the pure phases using the PBEsol functional is drawn to guide the eye. The small variations of the lattice constant at each composition are due to the different

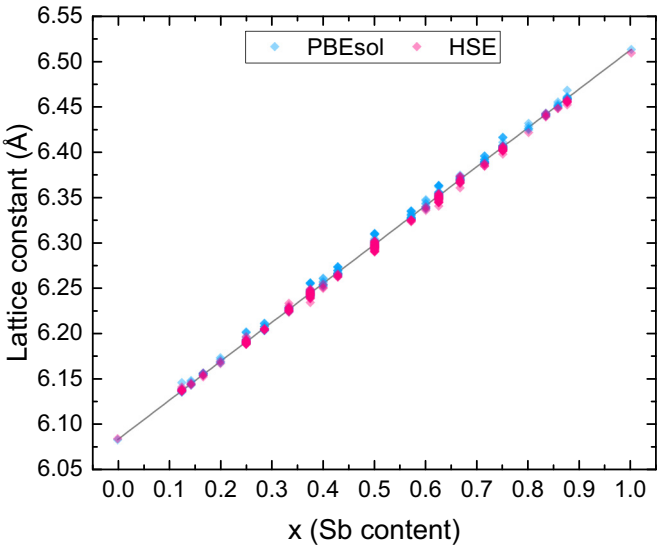

FIG. 1. The lattice constants of the InAsSb alloys for different compositions obtained by calculations using the PBEsol and HSE functionals.

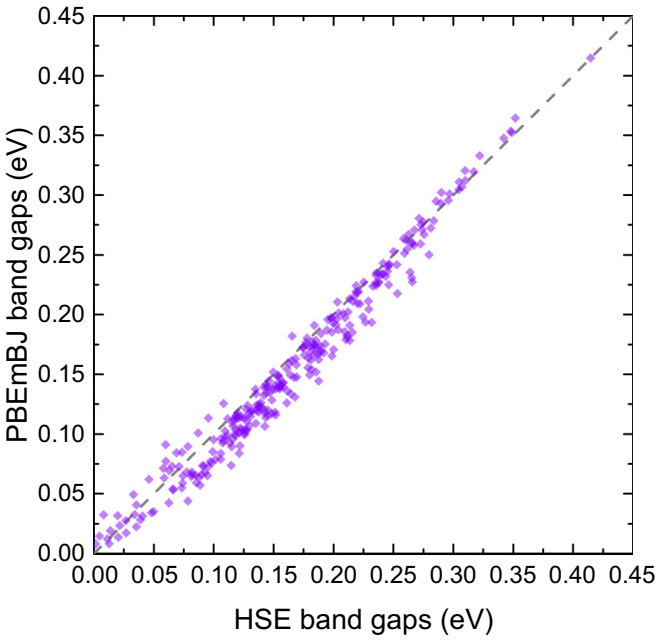

FIG. 2. Comparison of the band gaps obtained by the HSE and PBEmBJ calculations in a subset of 290 atomic configurations.

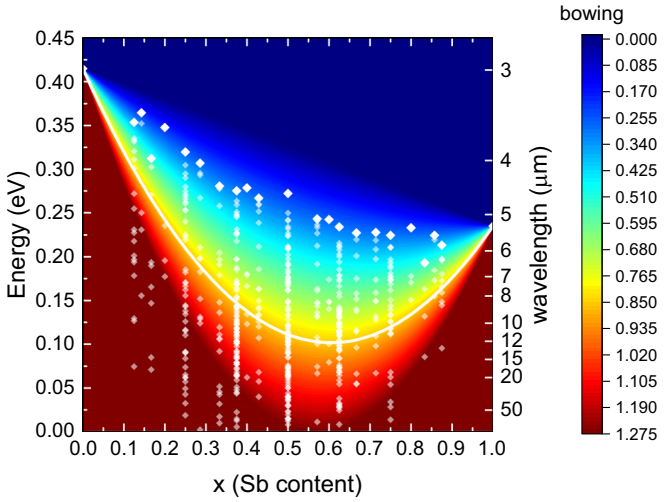

FIG. 3. Band gap values obtained by the PBEmBJ calculations for the different atomic configurations using supercells of up to 16 atoms. The color map illustrates the different bowing parameters as a guide to the eye.

atomic configurations. The maximum variation is less than 0.26% compared to the average value for each composition. Evidently, an excellent agreement with linearity is observed for both functionals.

In a system such as InAsSb, where including SOC is essential [46], managing the increased computational cost becomes even more important. Previous studies have demonstrated an excellent agreement between hybrid functional and mBJ calculations [35,47], where the latter are performed at a fraction of the computational cost of the former. In this work, the large number of atomic configurations requires the use of a computationally efficient, yet reliable scheme. Therefore, the band gaps of the various configurations at different compositions were obtained using the PBEsol optimized structures and the mBJ functional.

Figure 2 presents the comparison of the PBEmBJ band gaps versus the results obtained by HSE calculations in the subset of 290 structures. The dashed line is used as a guide to demonstrate the case of perfect agreement. The results indicate that, typically, the HSE band gaps are systematically larger compared to the semilocal approach, especially in the lower range of values. The agreement seems to improve significantly for larger band gaps. This can be attributed to the fact that small band gaps are more sensitive to the comparison between the two approaches, since the difference becomes comparable to the value of the band gap itself. Nonetheless, an overall good agreement is observed between the two functionals.

For a given compound of constituents A and B, the composition dependent band gap can be expressed as

$$E_g^{A_{1-x}B_x} = xE_g^B + (1-x)E_g^A - bx(1-x), \qquad (1)$$

where E_g^A and E_g^B are the band gaps of each constituent, respectively, and b is the bowing parameter. Large positive values of the bowing parameter indicate strong downward deviations of the band gaps from linearity, implying longer absorption wavelengths. As mentioned earlier, the matter of the bowing parameter in the InAsSb system has been discussed extensively for decades [2,6,8]. Experimental findings [6] have demonstrated the existence of InAsSb alloys capable of reaching the LWIR regime with larger bowing values than previously proposed. Based on Eq. (1), reaching the beginning of the LWIR regime at 8 μm requires a bowing parameter of at least 0.63 eV at a composition of 64% Sb content.

Figure 3 presents the band gaps obtained by the different atomic configurations using PBEmBJ calculations. It also includes a color scheme to visualize the different values of the bowing parameter as a guide to the eye. One immediate observation is the strong nonlinearity of the band gap versus the composition, since even the largest band gaps, shown with magnified diamonds in Fig. 3, deviate from linearity. Using these values, one can obtain the lower limit of the bowing parameter to be 0.29 eV. However, only few atomic configurations exhibit so large band gaps. In fact, the majority of the different atomic configurations yield band gaps in the LWIR regime and even approach 0 eV. This can be observed by the density of points in Fig. 3. Additionally, Fig. 4 illustrates the above remark through a histogram of the band gap values for the cases of 37.5%, 50%, and 62.5% of Sb content.

An estimate for the bowing parameter can be obtained by fitting Eq. (1) using the arithmetic mean of the band gaps for each of the compositions of 37.5%, 50%, and 62.5% of Sb content, since most of the data points lie in these compositions. The obtained value of 0.85 eV is shown with the solid curve in Fig. 3, and is in excellent agreement with previous experimental results by Svensson *et al.* [6] where the bowing parameter was 0.87 eV. A different approach would be to use the formation enthalpy of each configuration and employ an averaging scheme based on the Boltzmann distribution. This scheme yields a weighted average for the band gap of each composition. The assumptions of this approach

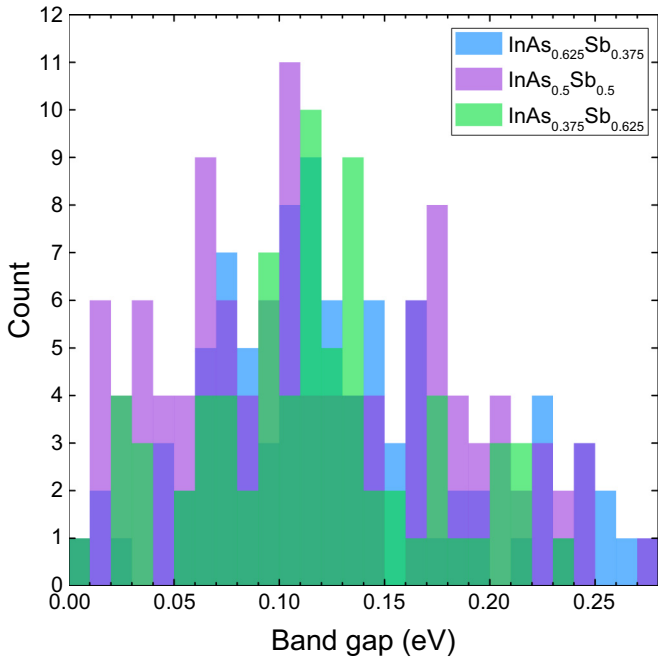

FIG. 4. The frequency of the band gaps for the compositions of 37.5%, 50%, and 62.5% of Sb content.

should be mentioned though. First, this approach is valid under the assumption that bulk thermodynamics determines the likelihood of each configuration. However, this might not be necessarily true, particularly in epitaxial growth where kinetics and surface phenomena play an important role in the formation of the material. Second, at high temperatures the likelihood obtained by the Boltzmann distribution approaches the simple arithmetic mean. In our case specifically, the results of the bowing parameter obtained by both approaches were identical at a temperature of approximately 700 K, which is relevant during growth.

Furthermore, two examples of configurations with band gaps in the LWIR regime for $x = 0.625$ are the $(InAs)_3/(InSb)_5$ superlattices along the [100] (CuAu ordering) and [311] directions with band gaps of 0.10 and 0.12 eV, respectively. It should be noted that Fig. 3 shows the range of possible band gaps obtained by the various atomic configurations. Experimentally, though, not all the atomic configurations might be accessible.

At this point, it is worth mentioning a recent development regarding the InAsSb system, which is the fact that structures exhibiting CuPt ordering, i.e., ordering along the [111] direction, are able to produce topological semimetallic phases in InAsSb. Investigating such effects in alloy systems is not a trivial matter, especially in the case of large supercells. On the one hand, the E versus $\boldsymbol{k}$ relationship becomes too complicated in large supercells due to the folding of the bands. On the other hand, traditional approaches such as the VCA or the CPA fail to capture the important effects of the local atomic environments in alloys by imposing an artificially high symmetry. Hence, in both cases, valuable information is concealed.

The above mentioned problems can be mitigated with the use of the effective band structure (EBS) [48,49] method which is a supercell approach capable of restoring the E versus $\boldsymbol{k}$ band dispersion of the alloy into the primitive Brillouin zone. Figure 5 shows the band structures of the CuPt-ordered alloys for 25%, 50%, and 75% Sb content, obtained by PBEmBJ calculations in a region close to the Γ point ($|\boldsymbol{k}| \leqslant 0.25\,\text{Å}^{-1}$) and towards the X and L points. The unfolding has been performed using the BandUP code [50,51]. Theoretical evidence of the semimetallic behavior of CuPt-ordered InAsSb was reported previously by Wei and Zunger [52]. Recently, Winkler *et al.* [53] expanded the discussion on this matter including the CuPt-ordered structures of $InAs_{0.67}Sb_{0.33}$ and $InAs_{0.33}Sb_{0.67}$ in addition to $InAs_{0.5}Sb_{0.5}$, demonstrating the topological semimetallic phases of these structures. The band structure presented in Fig. 5 is in excellent agreement with previous results [53].

Typically, monolayer superlattices tend to increase the band gap due to quantum confinement. However, in the case of zincblende InAsSb, the ordering along the [111] direction reduces the T_d symmetry of the crystal to C_{3v}, where the L point folds into the center of the Brillouin zone. This

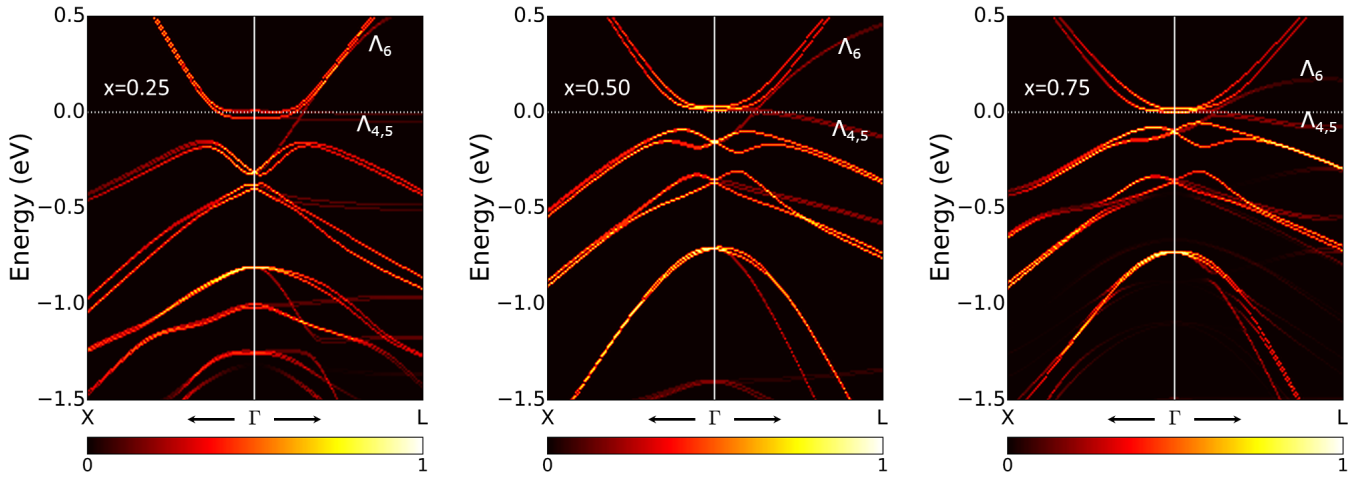

FIG. 5. The effective band structures obtained by the PBEmBJ calculations for the CuPt-ordered alloys with 25%, 50%, and 75% Sb content, around the Γ point ($|\boldsymbol{k}| \leqslant 0.25\,\text{Å}^{-1}$). The spectral weights are normalized to one.

folding causes a repulsion [54] of the Γ-like states at the band edges, which reduces the band gap significantly. Furthermore, the crossing in the band structure causing the semimetallic character, shown in Fig. 5, appears due to the band inversion between the $\Lambda_{4,5}$ and Λ_6 bands and is topologically protected by the C_3-rotational symmetry of the crystal [53].

IV. CONCLUSION

In conclusion, the band gaps of 692 distinct atomic configurations of InAsSb alloys, obtained by supercells of up to 16 atoms, were investigated using the PBE formalism coupled with the mBJ exchange potential and supported by hybrid functional calculations. The smallest bowing parameter of 0.29 eV, corresponding to the largest calculated band gap of each composition, is indicative of the nonlinearity of the band gap for this system. Furthermore, the existence of multiple configurations capable of producing band gaps in the LWIR regime was theoretically verified for a wide range of compositions and a bowing parameter of 0.85 eV was obtained by averaging the band gaps of the different atomic configurations with compositions of 37.5%, 50%, and 62.5% of Sb content. Additionally, a comparison of the PBEmBJ calculations versus more computationally expensive HSE calculations revealed the good agreement of the two approaches, demonstrating the efficiency and accuracy of the former for the study of the InAsSb alloy system. Finally, the EBS approach was used to illustrate the band structure of some configurations exhibiting CuPt-type ordering, which give rise to topological semimetallic phases.

ACKNOWLEDGMENTS

The authors gratefully acknowledge fruitful discussions with Prof. G. Belenky and Dr. S. P. Svensson, as well as financial support from the US Army Research Laboratory through the Collaborative Research Alliance (Grant No. W911NF-12-2-0023) for Multi-Scale multidisciplinary Modeling of Electronic Materials (CRA-MSME) and the Center for Semiconductor Materials and Devices Modeling (Grant No. W911NF-18-2-0027) at Boston University. The computational resources were provided by the DoD HPC Systems and the 2019 Army Research Office DURIP Award (Grant No. W911NF-19-1-0161) made to Dr. E. Bellotti.

[1] A. G. Thompson and J. C. Woolley, Can. J. Phys. **45**, 255 (1967).
[2] Z. M. Fang, K. Y. Ma, D. H. Jaw, R. M. Cohen, and G. B. Stringfellow, J. Appl. Phys. **67**, 7034 (1990).
[3] M. Y. Yen, R. People, K. W. Wecht, and A. Y. Cho, Appl. Phys. Lett. **52**, 489 (1988).
[4] S. Elies, A. Krier, I. R. Cleverley, and K. Singer, J. Phys. D: Appl. Phys. **26**, 159 (1993).
[5] W. L. Sarney, S. P. Svensson, Y. Xu, D. Donetsky, and G. Belenky, J. Appl. Phys. **122**, 025705 (2017).
[6] S. P. Svensson, W. L. Sarney, H. Hier, Y. Lin, D. Wang, D. Donetsky, L. Shterengas, G. Kipshidze, and G. Belenky, Phys. Rev. B **86**, 245205 (2012).
[7] J. D. Kim, D. Wu, J. Wojkowski, J. Piotrowski, J. Xu, and M. Razeghi, Appl. Phys. Lett. **68**, 99 (1996).
[8] W. M. Coderre and J. C. Woolley, Can. J. Phys. **46**, 1207 (1968).
[9] E. C. Young, F. Wu, A. E. Romanov, D. A. Haeger, S. Nakamura, S. P. Denbaars, D. A. Cohen, and J. S. Speck, Appl. Phys. Lett. **101**, 142109 (2012).
[10] M. A. Hossain, M. R. Islam, M. K. Hossain, A. Hashimoto, and A. Yamamoto, Mater. Renew. Sustain. Energy **3**, 20 (2013).
[11] M. B. Katz, M. E. Twigg, N. A. Mahadik, C. L. Canedy, and C. A. Affouda, J. Electron. Mater. **45**, 2102 (2016).
[12] A. P. Craig, A. R. J. Marshall, Z.-B. Tian, S. Krishna, and A. Krier, Appl. Phys. Lett. **103**, 253502 (2013).
[13] G. Belenky, D. Donetsky, G. Kipshidze, D. Wang, L. Shterengas, W. L. Sarney, and S. P. Svensson, Appl. Phys. Lett. **99**, 141116 (2011).
[14] W. L. Sarney, S. P. Svensson, H. Hier, G. Kipshidze, D. Donetsky, D. Wang, L. Shterengas, and G. Belenky, J. Vac. Sci. Technol. B **30**, 02B105 (2012).
[15] M. Y. Yen, R. People, and K. W. Wecht, J. Appl. Phys. **64**, 952 (1988).
[16] L. Nordheim, Ann. Phys. **401**, 607 (1931).
[17] N. J. Ramer and A. M. Rappe, Phys. Rev. B **62**, R743 (2000).
[18] P. Soven, Phys. Rev. **156**, 809 (1967).
[19] P. Soven, Phys. Rev. **178**, 1136 (1969).
[20] J. S. Faulkner and G. M. Stocks, Phys. Rev. B **21**, 3222 (1980).
[21] J. Faulkner, Prog. Mater. Sci. **27**, 1 (1982).
[22] S.-H. Wei and A. Zunger, Phys. Rev. B **52**, 12039 (1995).
[23] H. Wen and E. Bellotti, Appl. Phys. Lett. **107**, 222103 (2015).
[24] N. Bouarissa, N. Amrane, and H. Aourag, Infrared Phys. Technol. **36**, 755 (1995).
[25] P. Hohenberg and W. Kohn, Phys. Rev. **136**, B864 (1964).
[26] W. Kohn and L. J. Sham, Phys. Rev. **140**, A1133 (1965).
[27] P. E. Blöchl, Phys. Rev. B **50**, 17953 (1994).
[28] G. Kresse and D. Joubert, Phys. Rev. B **59**, 1758 (1999).
[29] G. Kresse and J. Furthmüller, Phys. Rev. B **54**, 11169 (1996).
[30] J. P. Perdew, K. Burke, and M. Ernzerhof, Phys. Rev. Lett. **77**, 3865 (1996).
[31] J. P. Perdew, K. Burke, and M. Ernzerhof, Phys. Rev. Lett. **78**, 1396 (1997).
[32] J. P. Perdew, A. Ruzsinszky, G. I. Csonka, O. A. Vydrov, G. E. Scuseria, L. A. Constantin, X. Zhou, and K. Burke, Phys. Rev. Lett. **100**, 136406 (2008).
[33] J. P. Perdew and A. Zunger, Phys. Rev. B **23**, 5048 (1981).
[34] A. D. Becke and E. R. Johnson, J. Chem. Phys. **124**, 221101 (2006).
[35] F. Tran and P. Blaha, Phys. Rev. Lett. **102**, 226401 (2009).
[36] D. Koller, F. Tran, and P. Blaha, Phys. Rev. B **85**, 155109 (2012).
[37] H. Jiang, J. Chem. Phys. **138**, 134115 (2013).
[38] J. Heyd, G. E. Scuseria, and M. Ernzerhof, J. Chem. Phys. **118**, 8207 (2003).
[39] J. Heyd, G. E. Scuseria, and M. Ernzerhof, J. Chem. Phys. **124**, 219906 (2006).
[40] A. Alkauskas, P. Broqvist, F. Devynck, and A. Pasquarello, Phys. Rev. Lett. **101**, 106802 (2008).

[41] A. Kyrtsos, M. Matsubara, and E. Bellotti, Phys. Rev. B **99**, 035201 (2019).
[42] A. van de Walle, M. D. Asta, and G. Ceder, Calphad **26**, 539 (2002).
[43] A. van de Walle, Calphad **33**, 266 (2009).
[44] G. Giesecke and H. Pfister, Acta Crystallogr. **11**, 369 (1958).
[45] A. R. Denton and N. W. Ashcroft, Phys. Rev. A **43**, 3161 (1991).
[46] Y.-S. Kim, K. Hummer, and G. Kresse, Phys. Rev. B **80**, 035203 (2009).
[47] F. Tran and P. Blaha, J. Phys. Chem. A **121**, 3318 (2017).
[48] V. Popescu and A. Zunger, Phys. Rev. Lett. **104**, 236403 (2010).
[49] V. Popescu and A. Zunger, Phys. Rev. B **85**, 085201 (2012).
[50] P. V. C. Medeiros, S. Stafström, and J. Björk, Phys. Rev. B **89**, 041407(R) (2014).
[51] P. V. C. Medeiros, S. S. Tsirkin, S. Stafström, and J. Björk, Phys. Rev. B **91**, 041116(R) (2015).
[52] S. Wei and A. Zunger, Appl. Phys. Lett. **58**, 2684 (1991).
[53] G. W. Winkler, Q. S. Wu, M. Troyer, P. Krogstrup, and A. A. Soluyanov, Phys. Rev. Lett. **117**, 076403 (2016).
[54] S.-H. Wei and A. Zunger, Phys. Rev. B **39**, 3279 (1989).

IOP Publishing Journal of Physics: Condensed Matter
J. Phys.: Condens. Matter **32** (2020) 365504 (9pp) https://doi.org/10.1088/1361-648X/ab922a

Band offsets of $Al_xGa_{1-x}N$ alloys using first-principles calculations

Alexandros Kyrtsos[1,3], **Masahiko Matsubara**[1] and **Enrico Bellotti**[1,2]

[1] Department of Electrical and Computer Engineering, Boston University, Boston, MA 02215, United States of America
[2] Division of Materials Science and Engineering, Boston University, Boston, MA 02215, United States of America

E-mail: akyrtsos@bu.edu

Received 20 March 2020, revised 1 May 2020
Accepted for publication 12 May 2020
Published 17 June 2020

Abstract

First-principles calculations are employed for the study of the band offsets of $Al_xGa_{1-x}N$ alloys, taking into account their composition and atomic configuration. Specifically, the band offsets are obtained using PBE, PBEsol, Heyd, Scuseria, and Ernzerhof (HSE), and modified Becke–Johnson calculations, comparing the results and discussing the advantages and disadvantages of each functional. The band alignments are performed using the branch point energies of the materials as their common reference level. HSE calculations predict a valence band offset of 0.9 eV between GaN and AlN. Regarding the alloys, a conduction band edge bowing parameter of 0.55 eV and a practically zero bowing for the valence band edge is predicted on average. The different atomic configurations affect mainly the valence band edges, where deviations from linearity by more than 0.1 eV are observed.

Keywords: density functional theory, alloys, band offset, AlGaN

(Some figures may appear in colour only in the online journal)

1. Introduction

Group III-nitride semiconductors have demonstrated their technological importance in various applications such as optoelectronics [1, 2], power electronics [3], and photovoltaics [4]. In particular, wurtzite $Al_xGa_{1-x}N$ alloys, hereafter called AlGaN for the sake of brevity, feature a wide range of band gaps ranging from 3.4 to 6.2 eV [5] for pure GaN and AlN, respectively, spanning the ultraviolet (UV) and deep UV spectrum. Typical examples of applications in this spectrum involve free space communications, identification of biochemical agents, counterfeit detection, disinfection, and medical diagnostics.

In general, a miscibility gap is observed in group III-nitride mixed crystals in temperatures well above growth temperature [6, 7]. Specifically, phase separation has been observed in InGaN and InAlN alloys in a wide range of compositions [8–15], while the same has been observed in the case of BGaN and BAlN as well, where the boron incorporation is typically less than 3% [15–18]. The spinodal decomposition occurring in the above mentioned cases acts as a strain relief mechanism driven by the internal strain due to the excessive lattice mismatch caused by the presence of indium or boron. AlGaN, on the other hand, is an exception in III–V semiconductors due to the relatively small lattice mismatch between GaN and AlN. The critical temperature for the appearance of the miscibility gap in the case of the AlGaN system has been shown to be much lower than the typical growth temperatures of this material [15, 19]. Hence, excellent solubility is achievable for this system at any composition.

Although pure GaN and AlN have been investigated fairly extensively, the electronic properties of the alloys pose a greater challenge due to the plethora of different atomic configurations and their effect on the properties of the material. Therefore, many discrepancies appear in the reported results for wurtzite AlGaN alloys. For instance, the reported values for the band gap bowing parameter range from −0.8 (upward bowing) to +2.6 eV (downward bowing) [20–31], even though

[3] Author to whom any correspondence should be addressed.

the early findings of an upward bowing have not been reproduced [26, 28]. Furthermore, experimentally measured values for the valence band offset between GaN and AlN range from 0.15 to 1.4 eV [32–35], while theoretical calculations estimate the valence band offset between 0.34 and 1.6 eV [36–47].

The technological importance of AlGaN requires the comprehensive investigation of the electronic properties of this system. However, such an investigation imposes certain challenges from a theoretical point of view. Typical theoretical approaches for the investigation of alloys include the virtual crystal approximation (VCA) [48] and the coherent potential approximation (CPA) [49]. In the VCA, a virtual atom is employed, for which the potential is averaged based on the ionic weights of the atoms in the corresponding alloy, while in the CPA the alloy is replaced by an ordered effective medium where the configurational averaged properties of the real system are calculated using the Green's functions formalism. Even though these methods are computationally inexpensive and have been used extensively in various systems, both of them rely on an averaging scheme and are unable to capture the effects of the various atomic configurations on the properties of the alloys.

It is the aim of this work to investigate the band offsets of the wurtzite AlGaN system over the whole composition range, elucidating the effects of the various atomic configurations by first-principles calculations. Specifically, we employ both standard and hybrid density functional theory (DFT) [50, 51] calculations, including different commonly used functionals in order to compare the results. Furthermore, a discussion is provided aiming to present the advantages and disadvantages of each approach and develop a methodology for the treatment of the band offsets of alloy systems by considering their atomic configurations explicitly.

The manuscript is organized as follows. In the following section (section 2) we describe the method and the details of the calculations. Section 3 presents the results of our calculations, followed by a discussion on the implications of the results and a comparison with the available data in literature in section 4. Finally, section 5 summarizes and concludes the manuscript.

2. Method

Both standard DFT and hybrid functional calculations were employed using the Vienna *ab-initio* simulation package (VASP) [52]. Specifically, the standard DFT approach refers to calculations with the PBE [53, 54] and PBEsol [55] generalized gradient approximation (GGA) functionals. Hybrid functional calculations were performed in the parameterization by Heyd, Scuseria, and Ernzerhof (HSE) [56, 57]. Finally, the Tran–Blaha modified Becke–Johnson (mBJ) [58, 59] meta-GGA functional was also employed and compared to the computationally more expensive HSE calculations.

The alloys were studied considering the exhaustive set of wurtzite atomic configurations in supercells of up to 16 atoms generated by the ATAT code [60, 61]. A total number of 401 distinct atomic configurations in 13 different compositions including the binaries were employed. For consistency purposes, Γ-centered k-point meshes with a density of at least $1000\,k$ points per reciprocal atom were used for all the supercells throughout the calculations. Furthermore, all the calculations were spin polarized with an energy cutoff of 500 eV for the plane-wave basis set, while the gallium 3d electrons were treated as valence electrons. The supercells were optimized using both atomic and volume relaxations, with a force criterion of 10^{-3} and 0.02 eV Å^{-1} for the standard DFT and hybrid functional calculations, respectively. Specifically, PBE, PBEsol, and HSE results correspond to structures optimized with their corresponding functional, while mBJ results correspond to structures optimized with the PBEsol functional.

Although standard DFT calculations typically underestimate the band gap of semiconductors significantly [62], they remain popular due to the considerably lower computational cost compared to other approaches such as hybrid functional or GW calculations. An improved description of the band gap at almost the same cost as standard DFT calculations arises from the mBJ [58, 59] meta-GGA functional, which yields band gaps with an accuracy similar to hybrid functional or GW calculations and in very good agreement with experimental data [63, 64]. The mBJ potential by Tran and Blaha [58] is a modification to the Becke–Johnson (BJ) [59] potential and is given by

$$v_{x,\sigma}^{\mathrm{mBJ}}(\mathbf{r}) = c\,v_{x,\sigma}^{\mathrm{BR}}(\mathbf{r}) + (3c-2)\frac{1}{\pi}\sqrt{\frac{5}{12}}\sqrt{\frac{2t_\sigma(\mathbf{r})}{\rho_\sigma(\mathbf{r})}}, \qquad (1)$$

where $v_{x,\sigma}^{\mathrm{BR}}(\mathbf{r})$ is the Becke–Roussel (BR) [65] potential, $\rho_\sigma(\mathbf{r})$ is the electron density, and $t_\sigma(\mathbf{r})$ is the kinetic energy density. For $c = 1$ the original BJ [59] potential is recovered. Parameter c in equation (1) is defined as

$$c = \alpha + \beta\left(\frac{1}{\Omega}\int_{\mathrm{cell}}\frac{|\nabla\rho(\mathbf{r}')|}{\rho(\mathbf{r}')}\,\mathrm{d}\mathbf{r}'\right)^{1/2}, \qquad (2)$$

where α and β are empirically determined parameters and Ω is the volume of the supercell. The typical values of $\alpha = -0.012$ (dimensionless) and $\beta = 1.023\,\mathrm{bohr}^{1/2}$ are obtained by minimizing the mean absolute relative error for the band gap of the solids listed in table 1 of reference [58]. In general, the optimal value c_{opt} which yields perfect agreement with the experimental band gaps lies in the range of 1.1–1.3 and 1.4–1.7 for small and large band gap materials [58], respectively and is typically different from the self-consistent value obtained by equation (2).

The experimental band gaps of GaN and AlN are reproduced with HSE calculations using a Hartree–Fock (HF) mixing parameter of 0.28 and 0.32, respectively. Regarding the alloys, a linear interpolation between the values of 0.28 and 0.32 was employed for the study of the alloys, as described elsewhere [36]. Similar to the HSE calculations, a single c parameter of the mBJ potential is not able to reproduce the band gaps of both GaN and AlN at the same time. In the case of mBJ calculations though, there are a few different ways to treat parameter c. First, parameter c can be determined self-consistently by the electron density as shown in equation (2), where α and β are empirical parameters. An other

way is to set parameter c to a value that reproduces the band gap of the given material, in which case it is usually referred to as optimal c. Finally, the last approach is to set a species-specific c_i parameter. In this case, the mBJ potential at point $\mathbf{r}$ is calculated using the parameter c_i belonging to the atomic species which is nearest to the position $\mathbf{r}$.

In general, the electronic properties of alloys, such as the band gap and the band offsets, change in a non-linear fashion with respect to the composition. In such cases, a quadratic behavior is typically assumed. Therefore, a quantity Q of a compound $A_{1-x}B_x$ can be expressed as

$$Q = (1-x)Q_A + xQ_B - bx(1-x), \tag{3}$$

where Q_A and Q_B refer to the given quantity of the pure constituents A and B, respectively. The factor b is commonly called the bowing parameter of the given quantity and determines the degree of nonlinearity. Positive values of the bowing parameter result in convex behavior (downward bowing), while negative values indicate concave behavior (upward bowing). Equation (3) can be applied to the conduction and valence band edges independently, giving rise to the bowing parameters b_c and b_v, respectively. Furthermore, the total bowing parameter of the band gap can be expressed in terms of b_c and b_v by the relationship $b_g = b_c - b_v$. In this work, the constituents A and B refer to pure GaN and AlN, respectively.

Various methods for aligning the band edges of different materials are available through first-principles calculations. Some of the most commonly used methods are the alignment with respect to the vacuum level following Shockley–Anderson's electron affinity rule [66–68] and the alignment using the heterostructure approach [69, 70]. These methods use the average electrostatic potential along a certain direction as a reference level by employing a supercell of specific orientation. Moses *et al* [37] have shown that the average electrostatic potential is sensitive to the stoichiometry of the alloy in each layer perpendicular to the chosen direction in which the electrostatic potential is averaged. This finding imposes an insurmountable challenge for alloy systems, since very few atomic configurations fulfill this condition. The conditions become even more stringent in the case of wurtzite AlGaN because non-polar directions should be used in order to avoid polarization fields that affect the alignment. Therefore, the above mentioned techniques are unpractical for a comprehensive study of the band offsets in alloy systems.

A different approach which is more suitable for alloy systems is the alignment with respect to the branch point energy of each material [71, 72]. The branch point energy or charge neutrality level of each material is given by [71]

$$E_{BP} = \frac{1}{2N_{\mathbf{k}}}\sum_{\mathbf{k}}\left[\frac{1}{N_{CB}}\sum_{i}^{N_{CB}}\varepsilon_i^{CB}(\mathbf{k}) + \frac{1}{N_{VB}}\sum_{i}^{N_{VB}}\varepsilon_i^{VB}(\mathbf{k})\right], \tag{4}$$

where $N_{\mathbf{k}}$ refers to the total number of k points on which the summation is performed. A number of N_{CB} and N_{VB} of the lowest and uppermost conduction and valence bands, respectively, are included in the calculation of the E_{BP}. Furthermore, $\varepsilon_i^{CB}(\mathbf{k})$ and $\varepsilon_i^{VB}(\mathbf{k})$ refer to the energy eigenvalues of the chosen conduction and valence bands. Since the number of bands increases with the number of atoms in the supercell, for consistency purposes, two conduction and four valence bands per primitive cell were employed[4] in the calculation of the branch point energy in the alloy supercells. Once E_{BP} is determined by equation (4), the valence band maximum (VBM) and conduction band minimum (CBM) obtained by the bulk calculation may be referenced to the branch point energy as $\varepsilon^*_{VBM} = \varepsilon_{VBM} - E_{BP}$ and $\varepsilon^*_{CBM} = \varepsilon_{CBM} - E_{BP}$, respectively. As a result, the band edges of different structures can be aligned using ε^*_{VBM} and ε^*_{CBM}.

At this point it is also useful to mention that not all the 401 configurations employed in this study are equally likely to occur in reality. Furthermore, the present work does not examine the occurrence likelihood of each configuration. Instead, the aim is to rely on a reasonably large number of configurations in order to infer the possible variation of the band gaps and band offsets of the alloys due to the atomic configuration. A more detailed discussion about the formation energies of these structures, and the fact that they alone are not sufficient to provide a definite answer for the occurrence frequency of each configuration is provided elsewhere [36].

3. Results

The band gaps were obtained using the PBE and PBEsol GGA functionals, the HSE hybrid functional, and the mBJ meta-GGA functional using three different approaches for the determination of parameter c. Figure 1 shows the band gaps obtained by the PBE, PBEsol, and HSE calculations. As expected, the GGA functionals underestimate the band gaps of the binaries and the alloys. Specifically, the values of 1.72 and 1.91 eV were calculated for the band gap of GaN using PBE and PBEsol, respectively. In the case of AlN the band gaps from PBE and PBEsol were 4.07 and 4.12 eV, respectively. The minor differences between the PBE and PBEsol results are attributed to the fact that the latter is optimized for solid calculations and that these two GGA functionals predict slightly different lattice constants. On the other hand, the HSE functional is able to reproduce the correct experimental band gaps for the pure GaN and AlN using an appropriate HF mixing parameter and, therefore, it provides a better description of the band gaps of the alloys. Nonetheless, standard DFT calculations are in good qualitative agreement with the more expensive HSE calculations, except for the systematic underestimation of the band gap of each structure.

The mBJ calculations were performed following the three different methods discussed earlier for the determination of parameter c. The atomic structures were optimized using the PBEsol functional before performing the calculation with the mBJ potential for the determination of the band gap. In the case of the self-consistent determination of c, its value is obtained by equation (2) using the charge density and the

[4] For instance, in the 16-atom supercell one would need four times more valence and conduction bands compared to the primitive cell.

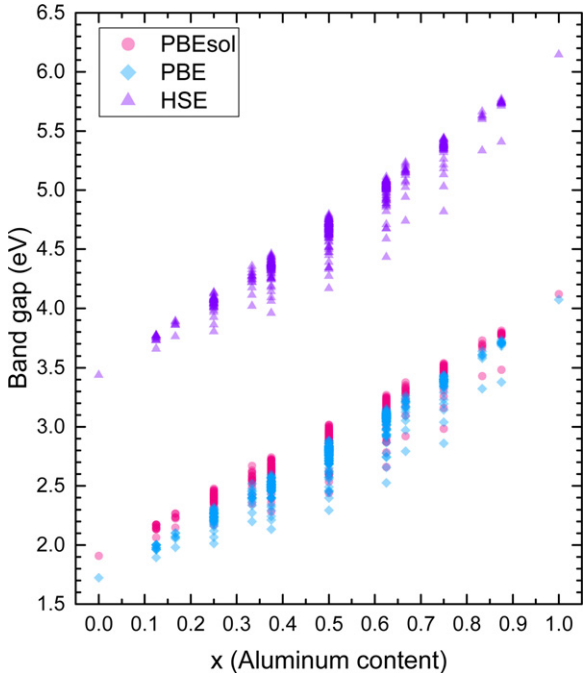

Figure 1. The band gaps of the alloys obtained by HSE, PBE, and PBEsol calculations.

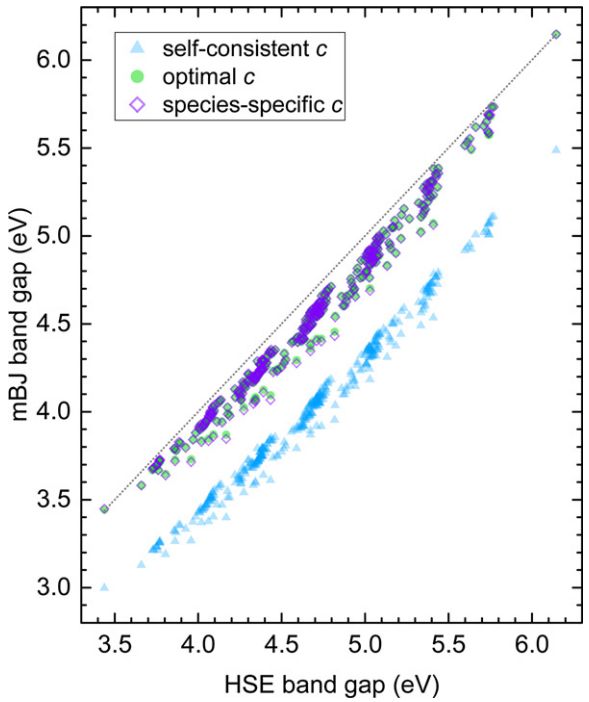

Figure 2. The mBJ values of the band gaps obtained by a self-consistent, optimal, and species-specific c parameter, compared to the values obtained by HSE calculations.

default values of α and β. The values of $c = 1.335$ and $c = 1.297$ with corresponding band gaps of 3.00 and 5.49 eV were obtained for GaN and AlN, respectively. This is already a significant improvement over the standard DFT approach at only marginally higher computational cost. The band gaps of all the atomic configurations obtained with a self-consistent parameter c are shown as blue triangles in figure 2. These values are still smaller than the experimental data and a larger c is necessary to achieve a better agreement.

A much better agreement between the mBJ and HSE calculations is observed in the other two cases. Regarding the case of an optimal c parameter, the values of $c_{\text{opt}}^{\text{GaN}} = 1.498$ and $c_{\text{opt}}^{\text{AlN}} = 1.526$ yield values of 3.44 and 6.15 eV for the band gaps of GaN and AlN, respectively. Similar to the HSE calculations, the value of c for the alloys was varied linearly between the values of the binaries. The results of this approach versus the HSE band gaps are shown as green circles in figure 2. The last case refers to the use of a species-specific parameter c_i. A parametric study of c_i was performed with respect to the band gaps of pure GaN and AlN, revealing that the results are mainly affected by c_{Ga} and c_{Al}. The values of $c_{\text{Ga}} = 1.50$, $c_{\text{Al}} = 1.54$, and $c_{\text{N}} = 1.47$ were obtained by the best fit to the parametric study and were eventually used in the alloy calculations. The results for the species-specific c parameter are presented in figure 2 with purple diamonds.

The alignment of the band edges of alloys of different compositions and atomic configurations was facilitated by the use of their branch point energies as the common reference level. The advantage of this approach is that it does not require the use of an interfacial supercell, whether it is with vacuum or a different material, where various stringent conditions need to be met. Instead, the bulk supercell of each structure may be used directly. Therefore, all the different atomic configurations can be investigated without exception. Naturally, the investigation of the band offsets requires the accurate description of the band gaps. In that respect, PBE, PBEsol, and mBJ calculations with a self-consistent c parameter yield band gaps that are typically smaller than the experimental data. Therefore, these calculations might not be suitable for the investigation of the band offsets, unless an *ad hoc* correction is applied in order to account for the underestimation of the band gap. Approaches such as HSE and mBJ calculations with variable mixing parameters provide a better description of the band gaps. Consequently, these methods appear to be more suitable for the study of the band offsets.

The results of the band offsets obtained by HSE calculations, as well as mBJ calculations with an optimal and a species-specific c parameter are presented in figures 3(a)–(c), respectively. The VBM of GaN is set to zero in all cases for convenience. The mean value and the standard deviation of the conduction and valence band edges at each composition are shown with diamond markers and shaded areas, respectively. The solid lines represent the least squares fit of equation (3) for the valence and conduction band edges separately. In the case of the HSE calculations, shown in figure 3(a), the valence band offset between GaN and AlN is 0.90 eV, while in the mBJ calculations, shown in figures 3(b) and (c), the valence band offset is 0.93 eV. The conduction band offset between GaN and AlN is 1.81 and 1.77 eV obtained by HSE and mBJ calculations, respectively. The mBJ results using the self-consistent value of the c parameter yield a valence and conduction band offset between the binaries of 0.80 and 1.69 eV, respectively. Consequently, a good agreement between HSE and mBJ is observed for the band offsets of the pure binaries. The results are listed in table 1.

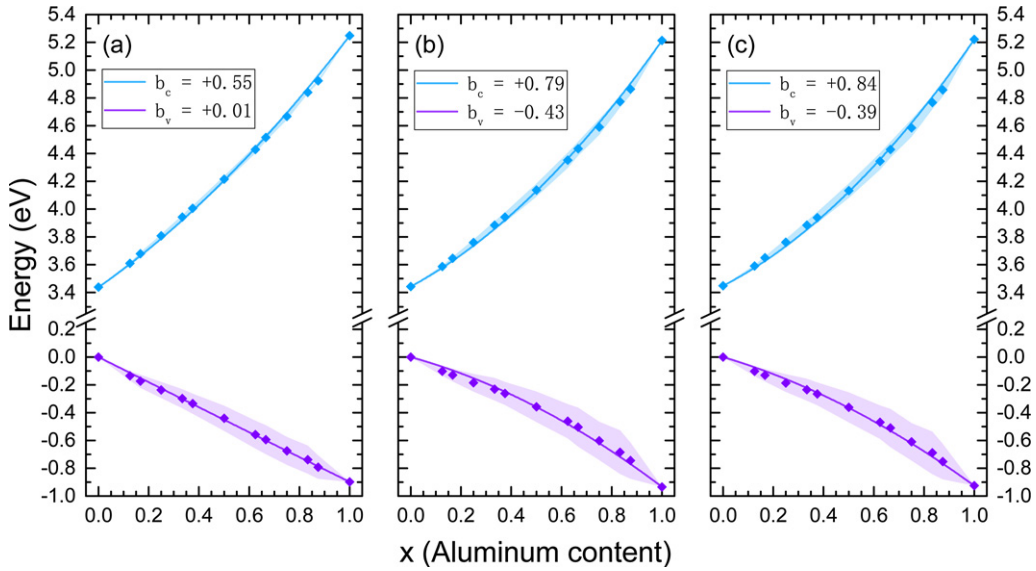

Figure 3. The band offsets of the alloys obtained by (a) HSE calculations, as well as mBJ calculations with (b) an optimal and (c) a species-specific c parameter. The legends indicate the bowing parameter of the valence and conduction band edges. The valence band edge of GaN is set to 0 eV for convenience.

Table 1. The band gaps for pure GaN and AlN, the valence and conduction band bowing parameters for the alloys, and the valence (ΔE_{v}) and conduction (ΔE_{c}) band offsets between the binaries, obtained by the four different functionals. The units of all the values are in eV.

Property	HSE	PBE	PBEsol	mBJ optimal c	mBJ Species-specific c	mBJ Self-consistent c
$E_{\mathrm{g}}^{\mathrm{GaN}}$	3.44	1.72	1.91	3.44	3.45	3.00
$E_{\mathrm{g}}^{\mathrm{AlN}}$	6.15	4.07	4.12	6.15	6.15	5.49
b_{v}	+0.01	−0.02	+0.04	−0.43	−0.39	−0.28
b_{c}	+0.55	+0.58	+0.55	+0.79	+0.84	+0.75
ΔE_{v}	0.90	0.77	0.73	0.93	0.93	0.80
ΔE_{c}	1.81	1.58	1.48	1.77	1.77	1.69

The striking difference between the two approaches lies in the results of the alloys. The mean values of the valence band offsets obtained by HSE calculations yield a valence band bowing of 0.01 eV, indicating a practically linear change of the valence band offsets throughout the whole composition range. The conduction band bowing parameter was 0.55 eV according to the HSE calculations. On the other hand, mBJ calculations yield a valence band bowing of −0.43 and −0.39 eV for an optimal and a species-specific c parameter, respectively. This negative bowing can also be seen by the concave behavior of the valence band offsets in figures 3(b) and (c). Furthermore, the conduction band bowings are 0.79 and 0.84 eV resulting in a total band gap bowing of 1.22 and 1.23 eV, respectively. Additionally, the mBJ calculations with a self-consistent c parameter yield the values of −0.28 and 0.75 eV for the valence and conduction band bowing parameters, respectively. Apparently, the total band gap bowing parameter obtained by the mBJ calculations is much larger compared to the HSE calculations. This is not surprising, since it was evident from figure 2 that even though HSE and mBJ calculations agree on the values of the binaries, the latter systematically underestimate the band gaps of the alloys.

It was mentioned earlier that standard DFT faces certain limitations on the description of the band offsets due to the underestimation of the band gap. This is true when one considers the full picture where both the band edges and the band gaps should be described properly. However, one might examine the alignment of the conduction and valence band edges separately, focusing only on their corresponding offsets and bowing parameters without considering the correct value of the band gap. Figure 4 shows the band offsets of the alloys, obtained by the PBE and PBEsol functionals. Although the band gaps are significantly smaller than the experimental values, the results are in good agreement with HSE calculations. Specifically, the valence band offset between GaN and AlN obtained by PBE and PBEsol calculations is 0.77 and 0.73 eV, respectively. Also, the valence band bowing parameter is −0.02 and 0.04 eV. Regarding the alignment of the conduction band edges, PBE and PBEsol calculations yield an offset of 1.58 and 1.48 eV between GaN and AlN, with corresponding conduction band bowing parameter of 0.58 and 0.55 eV. Therefore, the bowing parameters obtained by standard DFT calculations are in excellent agreement with the ones obtained by HSE calculations. Table 1 summarizes the results.

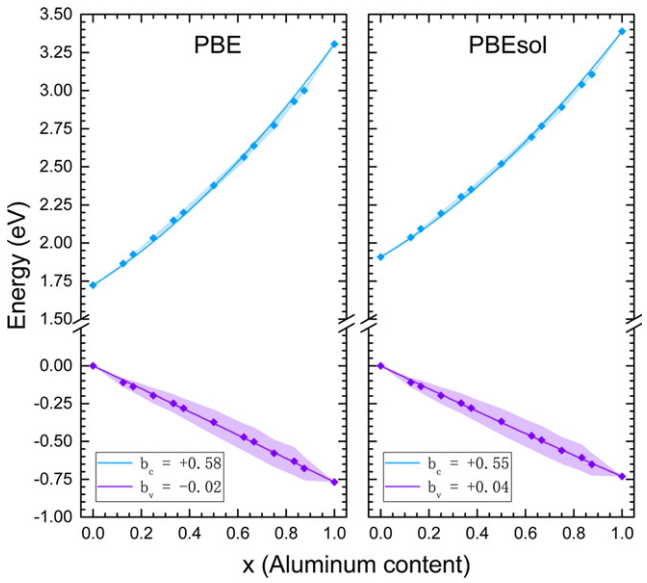

Figure 4. The band offsets of the alloys obtained by PBE and PBEsol calculations. The legends indicate the bowing parameter of the valence and conduction band edges. The valence band edge of GaN is set to 0 eV for convenience.

A common characteristic which is captured by all the different calculations is the fact that the valence band edges of the alloys exhibit larger standard deviations compared to the conduction band edges. The variations of the valence band edges are caused by the different atomic configurations. On the other hand, the conduction band edges are less sensitive to the various atomic configurations. This result can be discussed on the basis of the information derived by combining figures 1 and 3(a). The results presented in figure 1 indicate that the total bowing parameter takes non-negative values. Specifically, there are structures whose band gap lies on the straight line connecting the binaries yielding zero bowing and others that indicate a total bowing parameter that reaches large positive values. This can be explained in terms of the results presented in figure 3(a) regarding the valence band edges. Although a zero valence band bowing is calculated by the mean values of the valence band edges, the large deviations allow for large positive or negative values of the valence band bowing parameter. Hence, a large downward deviation of the valence band edges ($b_v > 0$) counteracts the conduction band bowing, which is less sensitive in changes due to the various atomic configurations, yielding a total zero bowing for the band gap. Similarly, an upward deviation for the valence band edges ($b_v < 0$), further increases the total bowing parameter of the band gap.

A closer inspection of the atomic configurations that cause large deviations from linearity for the valence band edges in different compositions reveals certain trends. In general, structures where the cations are homogeneously mixed, were found to exhibit downward deviation from linearity. On the other hand, structures where the cations are poorly mixed, such as superlattices, exhibited an upward deviation of their valence band edges. This result is consistent with a previous work [36] for the AlGaN system as well, where the alignment with respect to the vacuum level was employed to study the band offsets between the binaries and $Al_{0.5}Ga_{0.5}N$ alloys.

4. Discussion

The main goal of this work is to employ DFT calculations and demonstrate different approaches for the investigation of the electronic properties of alloy systems. In this effort, standard DFT, hybrid functional, and mBJ calculations were performed. In the case of HSE and mBJ calculations a variable HF mixing parameter and c parameter were utilized, respectively. Therefore, it is essential to discuss the use of a variable mixing parameter and its effects on different properties of the material before commenting on the results of this work. The mBJ calculations with a variable c parameter are similar to HSE calculations in many respects, since the mBJ potential can be viewed as a kind of hybrid potential where the amount of exact exchange is given by c [58]. Therefore, the term *mixing parameter* will be used interchangeably for both functionals in the discussion that follows.

Although the thermodynamic properties of the AlGaN alloys are beyond the scope of this work, it is worth mentioning the effects of a variable mixing parameter on these properties for completeness. These properties rely on the comparison of the total energies of different structures. The mBJ functional is a potential-only functional. Therefore, the calculations are not self-consistent with respect to the total energy and the total energies obtained by this functional cannot be used for the study of thermodynamic properties, regardless of the value of c. Instead, this functional is intended only for the description of the electronic properties of the system. Regarding the HSE calculations, the mixing parameter affects the total energy and, consequently, a comparison of the total energies of different alloys with the total energies of the pure binaries in order to obtain their formation enthalpies would be detrimental when a variable mixing parameter is used. A different functional such as PBE or HSE with constant mixing parameter for all the involved structures would be more suitable in this case.

The effects of the mixing parameter on the electronic properties of the system depend on the specific property under investigation. For instance, the band gaps are obtained as the difference of the eigenvalues of the CBM and the VBM. Even though the mixing parameter of both HSE and mBJ significantly affects these eigenvalues the band gap is an inherent property of each material and is independent of the band gap of different structures. Therefore, an optimized mixing parameter may be utilized in order to describe the band gap of each structure independently. Contrary to the band gaps, the band offsets are given as a relative quantity among the structures. Regardless of the method of choice for obtaining the band offsets, the band edges of each structure are aligned with respect to a chosen reference level. Therefore, it is essential to examine the effect of a variable mixing parameter on the reference level of choice in order to verify the validity of the results.

Using the Shockley–Anderson's electron affinity rule [66–68] the alignment occurs with respect to the vacuum level. In a previous work [36] it was shown that a variable

mixing parameter in HSE calculations does not affect the reference level in the AlGaN system using this method of alignment. Furthermore, in the heterostructure approach [69, 70] the band edges are aligned with respect to the average electrostatic potential at each side of the interface between the two materials. Alkauskas *et al* [70] showed that varying the mixing parameter in HSE calculations only marginally affected the reference levels and therefore a variable mixing parameter was justified in the case of the heterostructure method as well. In our case, the branch point energies of the alloys were used as the common reference level for the alignment of their band edges. The mixing parameter of the HSE calculations ranges between 0.28 and 0.32. In this range, the branch point energy of pure GaN, AlN, and the alloy structures was found to remain practically constant versus the HF mixing parameter. Specifically, the maximum deviation of the branch point energy of each structure was less than 0.04 eV, while in most cases the deviation was of the order of 0.02 eV. In the case of the mBJ calculations, the *c* parameter was found to greatly affect the branch point reference level by more than 0.17 eV. Figure 5 demonstrates the effect of a variable mixing parameter in HSE and mBJ calculations for the case of GaN by showing the band gap and the branch point energy in a range of mixing parameters that were relevant for the calculations in both schemes. The branch point energy obtained by the smallest mixing parameter in each scheme is set to zero for convenience.

As mentioned above, HSE calculations with a varying mixing parameter maintain a constant reference level and are suitable both for the study of band gaps and the band offsets. On the contrary, even though mBJ calculations improve the description of the band gaps compared to standard DFT calculations, the effect of a varying mixing parameter is detrimental since the reference level varies significantly, hence making this functional unsuitable for the band offsets. Additionally, one of the known [73] shortcomings of the mBJ functional is its limited success on the description of the effective masses, which is directly related to the accurate determination of the energy eigenvalues in the Brillouin zone. However, since a good description of the eigenvalues is essential for the determination of the branch point energy, the use of the mBJ potential is further exacerbated[5].

A comparison of the calculated and experimental band gaps and band offsets of GaN and AlN is possible due to the uniqueness of these structures. However, in the case of alloys, the comparison is not straightforward due to the plethora of different atomic configurations. Therefore, other macroscopic indicators such as the bowing parameter should be employed in order to facilitate a comparison with experimental data. The experimental values for the band gap bowing parameter of the AlGaN system range from −0.8 eV to +2.6 eV [21–31]. However, the early reports of an upward (negative) bowing have not been reproduced [26, 28]. Figure 1 indicates a non-negative bowing parameter supporting the experimental results. A detailed comparison of the effect of the different atomic configurations of the alloys on the bowing parameter was presented in a previous work [36], where it was shown that the PBE and HSE calculations yield the same total bowing parameter. In the case of mBJ calculations, although the band gaps of GaN and AlN are in excellent agreement with experimental data, the alloys exhibit a larger bowing parameter than HSE, as shown in figure 2.

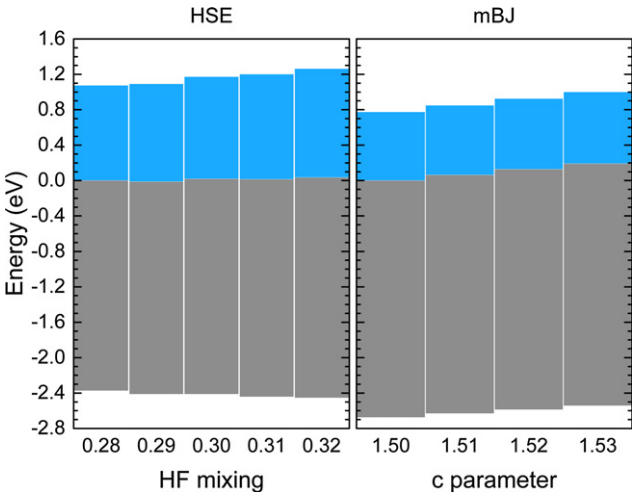

Figure 5. The effect of a variable Hartree–Fock mixing (HSE) and *c* (mBJ) parameter on the branch point energy of GaN. The first branch point energy of each method is set to 0 eV for convenience. The blue and gray boxes indicate the difference from the branch point energy to the conduction and valence band edge, respectively.

The band offsets obtained in the present work refer to the natural or unstrained band offsets. Therefore, the results could be compared to results obtained by the ionization potentials (IP) and electron affinities (EA) of unstrained materials. The IP is defined as the VBM referenced to the vacuum level, while the EA corresponds to the CBM referenced to the vacuum level. The experimental values of the EA of GaN range from 2.6 to 3.5 eV [74–77]. In the case of AlN, the experimental values of the EA range from 0 to 1.9 eV [76, 78]. Therefore, the conduction band offset between GaN and AlN ranges from 0.7 to 3.5 eV according to the experimental data. It should be noted that the wide discrepancy of the experimental values is caused by the challenging task to accurately determine the EA due to surface contamination and oxidation of the samples. Our results indicate a conduction band offset of 1.81 eV, which is in reasonable agreement with the experimental data. Furthermore, the branch point energies of GaN and AlN were found to be 2.37 and 3.27 eV above the VBM, respectively, according to the HSE calculations. Hence, the valence band offset between the binaries is 0.9 eV. These results are in excellent agreement with the results obtained by Schleife *et al* [71], where they calculated branch point energies of 2.37 and 3.33 eV for GaN and AlN, respectively, yielding a valence band offset of 0.96 eV.

Finally, it should be noted that the methods of alignment with respect to the vacuum level or the branch point energy should in principle yield similar results since they both refer to the natural band offset. Previous [36, 37] calculations

[5] It is important to note that the results for the mBJ functional were not affected by the choice of the PBEsol-relaxed structures. The results were the same as well for the HSE-relaxed structures with appropriately optimized mixing parameters.

employing the vacuum level as the reference level reported a valence band offset between GaN and AlN of 0.40–0.46 eV. These values are nearly half the ones reported here and elsewhere [71] by the method of alignment with respect to the branch point energies. Evidently, even though both methods yield values that are within the range of experimental results and are consistent with other similar calculations, there seems to be a discrepancy. A reasonable explanation for this discrepancy is not available. Nevertheless, both methods agree to the fact that the various atomic configurations mainly affect the valence band offsets rather than the conduction band offsets. This may be seen in figures 3 and 4, where the standard deviations of the valence band edges of each composition are much larger compared to the conduction band edges. The deviations arise from the different atomic configurations of the alloys.

The above mentioned effect was previously demonstrated [36] using two different kinds of structures and only for $Al_{0.5}Ga_{0.5}N$, due to the stringent requirements of the vacuum level approach regarding the atomic configurations. The first structure was representative of atomic configurations where the cations are poorly mixed, such as superlattices, while the second structure represented the cases where the cations are homogeneously mixed. It was found that in the former case an upward deviation from linearity appears for the valence band offsets, while a downward deviation was observed for the latter. In this work, the chosen method for the alignment of the band edges allows for the inclusion of all the different structures in all compositions without exceptions. Therefore, a much larger sample of atomic configurations can be examined. The results obtained by the comprehensive study among all the different structures are in excellent agreement with the previously reported data. Combining the information provided in figures 1–3, the variation of the band gaps arises mainly by the different position of the valence band edges. Specifically, alloys with a homogeneous distribution of cations yield larger band gaps and a downward valence band bowing, while the opposite applies for poorly mixed alloys, such as superlattices.

5. Conclusion

The band offsets of AlGaN alloys were investigated employing different levels of theory. Specifically, standard DFT, hybrid functional and mBJ calculations were performed on all the possible atomic configurations generated by supercells of up to 16 atoms in order to investigate the effect of the various atomic configurations of the alloys on their band offsets. The band alignment relied on the branch point energies of the alloys as their common reference level, allowing for the investigation of all the structures at a small computational cost.

Standard DFT calculations underestimated the band gap of the binaries and the alloys but the band gap bowing parameter was in excellent agreement with HSE calculations. Regarding the mBJ calculations, excellent agreement with the HSE calculations was observed only for pure GaN and AlN. The band gaps of the alloys obtained by mBJ calculations exhibited smaller values compared to HSE calculations, yielding an overall larger bowing parameter.

The valence band offset between GaN and AlN was 0.90 and 0.93 eV, obtained by HSE and mBJ calculations, respectively, while PBE and PBEsol calculations predicted a value of 0.77 and 0.73 eV. Therefore, the band offset between GaN and AlN obtained by mBJ calculations was in better agreement with HSE calculations. Nevertheless, mBJ calculations failed to yield the same level of agreement for the alloys. Instead, standard DFT was in excellent agreement with HSE calculations for the valence and conduction band bowing parameters of the alloys, regardless of the poorer description of the band gaps. Overall, the mean values of the valence band edges were found to change linearly versus the composition of the alloy while a conduction band offset bowing of 0.55 eV was calculated for the composition dependence of the conduction band edges. Nonetheless, it should be noted that a minimal variation of the conduction band edge was observed for the alloys, while a large spread of more than 0.2 eV was observed in the valence band offsets due to the different atomic configurations. Specifically, homogeneous mixing of the cations was found to yield a downward deviation of the valence band offset from linearity, while poorly mixed configurations such as superlattices caused an upward deviation.

Finally, we discussed the effects of a variable mixing parameter in HSE and mBJ calculations on the electronic properties of the materials. Such practice is certainly beneficial for the description of the band gaps but might be detrimental for the band offsets. Thus, the impact of the variable mixing parameter on the reference level used for the band alignment should always be carefully examined. The mBJ calculations were found to be unsuitable for the study of the band offsets of the alloys since the reference level of the band edges was inconsistent versus a variable c parameter. On the contrary, HSE calculations were found suitable both for the description of the band gaps and the band offsets.

Acknowledgments

This work was supported by the US Army Research Laboratory through the Collaborative Research Alliance for Multi-Scale Multidisciplinary Modeling of Electronic Materials (Grant No. W911NF-12-2-0023). The computational resources were provided by the DoD HPC Systems and the 2019 Army Research Office DURIP Award (Grant No. W911NF-19-1-0161).

ORCID iDs

Alexandros Kyrtsos https://orcid.org/0000-0002-8916-3791

References

[1] Pimputkar S, Speck J S, DenBaars S P and Nakamura S 2009 *Nat. Photon.* **3** 180
[2] Khan A, Balakrishnan K and Katona T 2008 *Nat. Photon.* **2** 77
[3] Mishra U K, Parikh P and Wu Y F 2002 *Proc. IEEE* **90** 1022

[4] Dahal R, Li J, Aryal K, Lin J Y and Jiang H X 2010 *Appl. Phys. Lett.* **97** 073115
[5] Levinshtein M, Rumyantsev S and Shur M 2001 *Properties of Advanced Semiconductor Materials: GaN, AIN, InN, BN, SiC, SiGe* (New York: Interscience (Wiley-Interscience))
[6] Ho I and Stringfellow G B 1996 *Appl. Phys. Lett.* **69** 2701
[7] Matsuoka T 1997 *Appl. Phys. Lett.* **71** 105
[8] Teles L K, Furthmüller J, Scolfaro L M R, Leite J R and Bechstedt F 2000 *Phys. Rev.* B **62** 2475
[9] Singh R, Doppalapudi D, Moustakas T D and Romano L T 1997 *Appl. Phys. Lett.* **70** 1089
[10] McCluskey M D, Romano L T, Krusor B S, Bour D P, Johnson N M and Brennan S 1998 *Appl. Phys. Lett.* **72** 1730
[11] Karpov S Y 1998 *MRS Internet J. Nitride Semicond. Res.* **3** e16
[12] Gan C K, Feng Y P and Srolovitz D J 2006 *Phys. Rev.* B **73** 235214
[13] Duff A I, Lymperakis L and Neugebauer J 2015 *Phys. Status Solidi* **252** 855
[14] Palisaitis J, Hsiao C-L, Hultman L, Birch J and Persson P O Å 2017 *Sci. Rep.* **7** 44390
[15] Razeghi M and Henini M 2004 *Optoelectronic Devices: III-Nitrides* vol 3 (Amsterdam: Elsevier) ch 16
[16] Teles L K, Scolfaro L M R, Leite J R, Furthmüller J and Bechstedt F 2002 *Appl. Phys. Lett.* **80** 1177
[17] Wei C H, Xie Z Y, Edgar J H, Zeng K C, Lin J Y, Jiang H X, Chaudhuri J, Ignatiev C and Braski D N 2000 *J. Electron. Mater.* **29** 452
[18] Shibata M, Kurimoto M, Yamamoto J, Honda T and Kawanishi H 1998 *J. Cryst. Growth* **189–190** 445
[19] Albanesi E A, Lambrecht W R L and Segall B 1993 *Phys. Rev.* B **48** 17841
[20] Marques M, Teles L K and Ferreira L G 2007 *Phys. Rev.* B **75** 033201
[21] Yun F, Reshchikov M A, He L, King T, Morkoç H, Novak S W and Wei L 2002 *J. Appl. Phys.* **92** 4837
[22] Khan M A, Skogman R A, Schulze R G and Gershenzon M 1983 *Appl. Phys. Lett.* **43** 492
[23] Yoshida S, Misawa S and Gonda S 1982 *J. Appl. Phys.* **53** 6844
[24] Angerer H *et al* 1997 *Appl. Phys. Lett.* **71** 1504
[25] Koide Y, Itoh H, Khan M R H, Hiramatu K, Sawaki N and Akasaki I 1987 *J. Appl. Phys.* **61** 4540
[26] Lee S R, Wright A F, Crawford M H, Petersen G A, Han J and Biefeld R M 1999 *Appl. Phys. Lett.* **74** 3344
[27] Shan W, Ager J W, Yu K M, Walukiewicz W, Haller E E, Martin M C, McKinney W R and Yang W 1999 *J. Appl. Phys.* **85** 8505
[28] Vurgaftman I and Meyer J R 2003 *J. Appl. Phys.* **94** 3675
[29] Pelá R R, Caetano C, Marques M, Ferreira L G, Furthmüller J and Teles L K 2011 *Appl. Phys. Lett.* **98** 151907
[30] Wu J, Walukiewicz W, Yu K, Ager J, Li S, Haller E, Lu H and Schaff W J 2003 *Solid State Commun.* **127** 411
[31] Dridi Z, Bouhafs B and Ruterana P 2003 *Semicond. Sci. Technol.* **18** 850
[32] Sitar Z, Paisley M, Yan B, Davis R, Ruan J and Choyke J 1991 *Thin Solid Films* **200** 311
[33] Rizzi A, Lantier R, Monti F, Lüth H, Sala F D, Di Carlo A and Lugli P 1999 *J. Vac. Sci. Technol.* **17** 1674
[34] Waldrop J R and Grant R W 1996 *Appl. Phys. Lett.* **68** 2879
[35] Baur J, Maier K, Kunzer M, Kaufmann U and Schneider J 1994 *Appl. Phys. Lett.* **65** 2211
[36] Kyrtsos A, Matsubara M and Bellotti E 2019 *Phys. Rev.* B **99** 035201
[37] Moses P G, Miao M, Yan Q and Van de Walle C G 2011 *Chem. Phys.* **134** 084703
[38] Albanesi E A, Lambrecht W R L and Segall B 1994 *J. Vac. Sci. Technol.* **12** 2470
[39] Satpathy S, Popovic Z S and Mitchel W C 2004 *J. Appl. Phys.* **95** 5597
[40] Nardelli M B, Rapcewicz K and Bernholc J 1997 *Phys. Rev.* B **55** R7323
[41] Binggeli N, Ferrara P and Baldereschi A 2001 *Phys. Rev.* B **63** 245306
[42] Bernardini F and Fiorentini V 1998 *Phys. Rev.* B **57** R9427
[43] Majewski J A, Zandler G and Vogl P 1998 *Semicond. Sci. Technol.* **13** A90
[44] Cociorva D, Aulbur W G and Wilkins J W 2002 *Solid State Commun.* **124** 63
[45] Rubio A, Corkill J L and Cohen M L 1994 *Phys. Rev.* B **49** 1952
[46] Wei S and Zunger A 1996 *Appl. Phys. Lett.* **69** 2719
[47] Van de Walle C G and Neugebauer J 2003 *Nature* **423** 626
[48] Lothar N 1931 *Ann. Phys.* **401** 607
[49] Faulkner J S and Stocks G M 1980 *Phys. Rev.* B **21** 3222
[50] Hohenberg P and Kohn W 1964 *Phys. Rev.* **136** B864
[51] Kohn W and Sham L J 1965 *Phys. Rev.* **140** A1133
[52] Kresse G and Furthmüller J 1996 *Phys. Rev.* B **54** 11169
[53] Perdew J P, Burke K and Ernzerhof M 1996 *Phys. Rev. Lett.* **77** 3865
[54] Perdew J P, Burke K and Ernzerhof M 1997 *Phys. Rev. Lett.* **78** 1396
[55] Perdew J P, Ruzsinszky A, Csonka G I, Vydrov O A, Scuseria G E, Constantin L A, Zhou X and Burke K 2008 *Phys. Rev. Lett.* **100** 136406
[56] Heyd J, Scuseria G E and Ernzerhof M 2003 *Chem. Phys.* **118** 8207
[57] Heyd J, Scuseria G E and Ernzerhof M 2006 *Chem. Phys.* **124** 219906
[58] Tran F and Blaha P 2009 *Phys. Rev. Lett.* **102** 226401
[59] Becke A D and Johnson E R 2006 *Chem. Phys.* **124** 221101
[60] van de Walle A, Asta M D and Ceder G 2002 *CALPHAD, Comput. Coupling Phase Diagr. Thermochem.* **26** 539
[61] van de Walle A 2009 *CALPHAD, Comput. Coupling Phase Diagr. Thermochem.* **33** 266
[62] Perdew J P and Zunger A 1981 *Phys. Rev.* B **23** 5048
[63] Koller D, Tran F and Blaha P 2012 *Phys. Rev.* B **85** 155109
[64] Jiang H 2013 *Chem. Phys.* **138** 134115
[65] Becke A D and Roussel M R 1989 *Phys. Rev.* A **39** 3761
[66] Hinuma Y, Grüneis A, Kresse G and Oba F 2014 *Phys. Rev.* B **90** 155405
[67] Höffling B, Schleife A, Rödl C and Bechstedt F 2012 *Phys. Rev.* B **85** 035305
[68] Anderson R 1962 *Solid-State Electron.* **5** 341
[69] Hinuma Y, Oba F, Kumagai Y and Tanaka I 2013 *Phys. Rev.* B **88** 035305
[70] Alkauskas A, Broqvist P, Devynck F and Pasquarello A 2008 *Phys. Rev. Lett.* **101** 106802
[71] Schleife A, Fuchs F, Rödl C, Furthmüller J and Bechstedt F 2009 *Appl. Phys. Lett.* **94** 012104
[72] Landmann M, Rauls E and Schmidt W G 2017 *Phys. Rev.* B **95** 155310
[73] Kim Y-S, Marsman M, Kresse G, Tran F and Blaha P 2010 *Phys. Rev.* B **82** 205212
[74] Grabowski S P, Schneider M, Nienhaus H, Mönch W, Dimitrov R, Ambacher O and Stutzmann M 2001 *Appl. Phys. Lett.* **78** 2503
[75] Tracy K M, Mecouch W J, Davis R F and Nemanich R J 2003 *J. Appl. Phys.* **94** 3163
[76] Benjamin M, Bremser M, Weeks T, King S, Davis R and Nemanich R 1996 *Appl. Surf. Sci.* **104–105** 455–60
[77] Wu C I and Kahn A 1998 *J. Vac. Sci. Technol.* **16** 2218
[78] Wu C I, Kahn A, Hellman E S and Buchanan D N E 1998 *Appl. Phys. Lett.* **73** 1346

Non-equilibrium Green's function modeling of type-II superlattice detectors and its connection to semiclassical approaches

Francesco Bertazzi,* Alberto Tibaldi, and Michele Goano
DET, Politecnico di Torino, Torino, Italy and
IEIIT-CNR, Torino, Italy

Jesus Alberto Gonzalez Montoya
DET, Politecnico di Torino, Torino, Italy

Enrico Bellotti
ECE Department, Boston University, Boston, MA, USA

Theoretical investigations of carrier transport in type-II superlattice detectors have been mostly limited to simplified semiclassical treatments, due to the computational challenges posed by quantum kinetic approaches. For example, interband tunneling in broken-gap configurations calls for a multiband description of the electronic structure, and spatially indirect optical transitions in superlattice absorbers require fully nonlocal carrier-photon self-energies. Moreover, a large number of iterations is needed to achieve self-consistency between Green's functions and self-energies in the presence of strongly localized states not directly accessible from the contacts. We demonstrate an accurate, yet computationally feasible non-equilibrium Green's function model of superlattice detectors by formulating the kinetic equations in terms of problem-matched maximally localized basis functions, numerically generated from few modes representing the main conductive channels of the nanostructure. The contribution of all the remaining modes is folded in an additional self-energy to ensure current conservation. Inspection of spatially- and energetically-resolved single particle properties offers insight into the complex nature of carrier transport in type-II superlattice detectors, and the connection to semiclassical approaches enables the interpretation of mobility experiments.

I. INTRODUCTION

The nearly lattice-matched 6.1 Å semiconductor family, which includes GaSb, AlSb, InAs and their related compounds, offers a viable alternative to the state-of-the-art infrared imaging technology based on bulk HgCdTe, see Ref. 1 for a comparative study. The tunability of the detection wavelength over most of the technologically-relevant infrared spectrum, the possibility of even realizing different energy-band alignments, from type-I to type-II broken-gap (misaligned, or type III) superlattices, the band structure flexibility in controlling conduction and valence band edges independently through adjustment of the constituent layer compositions and/or thicknesses, have led to the development of new device concepts and architectures with potentially suppressed Auger generation rates, lower dark currents and consequently higher operating temperature.[1] Whether this technology will reach its potential depends on technological parameters such as Shockley-Read-Hall (SRH) lifetimes, but also on the understanding of the underlying physics. Theoretical investigations based on simple band-structure arguments have not been conclusive, probably because carrier transport in type-II superlattices (T2SLs) is not quite fitting a single picture, but rather involves the combination and possibly the transition between different mechanisms, from miniband (coherent) transport, to (incoherent) sequential tunneling, or even Wannier-Stark hopping, depending on built-in and/or applied fields. A self-consistent description of carrier transport and optical absorption in T2SLs can be obtained by a quantum-kinetic framework based on a non-equilibrium Green's function (NEGF) approach. The present implementation includes acoustic scattering in the equipartition approximation, inelastic polar optical scattering, and carrier-photon scattering,[2–4] described by fully nonlocal self-energies computed in the self-consistent Born approximation (SCBA).[5]

The electronic structure of T2SLs has been described using a variety of theoretical approaches such as the empirical tight-binding method,[6] the empirical pseudopotential method,[7] and multiband k·p models within the envelope function approximation.[8–10] With the inclusion of the first conduction band, heavy-hole, light-hole, and spin-orbit split-off bands, the multiband 8×8 k·p model seems a good compromise between accuracy and computational efficiency. The non-locality of the carrier-photon interaction, the slow convergence of the self-consistent calculation of Green's functions and self-energies in the presence of strong confinement,[11] and the large number of unknowns needed for spatial resolution in realistic devices, can easily lead to a staggering computational effort. Moving to a mode space basis [12, 13] is particularly advantageous in the analysis of *supercell* superlattice detectors such as graded-gap M-, W-structure, complementary barrier detectors with superlattice absorbers surrounded by electron- and hole-blocking unipolar barriers (CBIRDs), and interband

* francesco.bertazzi@polito.it

cascade IR photodetectors, in which the transport of the photogenerated carriers is mediated by few discrete states, possibly forming a miniband, rather than through the coupling to the continuum spectrum of the bulk layers embedding the active region of *buried* junction detectors.[14]

II. THEORY

Consider a system evolving under the Hamiltonian operator

$$\hat{\mathcal{H}} = \hat{H} + \hat{H}_{\mathrm{ep}} + \hat{H}_{\mathrm{e}\gamma}, \tag{1}$$

where $\hat{H}$ is the exactly-solvable part of the superlattice Hamiltonian that contains the lattice and the electrostatic potential, and $\hat{H}_{\mathrm{ep}}$, $\hat{H}_{\mathrm{e}\gamma}$ are the many-body components that include carrier-phonon and carrier-photon interactions, respectively. Carrier-carrier interactions are included at the Hartree level through coupling to Poisson's equation. Electron-electron interactions beyond the mean-field approximation may be considered by explicit inclusion of dynamical screening through the GW formalism.[15, 16] In general, electron-electron scattering may change the intraband carrier dynamics by setting up a heated Maxwellian distribution, redistributing the electron population between subbands.[17] For example, in hot-carrier solar cells, electron-electron scattering is responsible for the fast photocarrier escape from the confined absorber states to the extended quasi-continuum states via thermionic emission.[16] The effect was observed at high incident optical power densities, corresponding to photon fluxes greater than 10^{19} photons/cm^2/s.[18] Since IR detectors operate at low injection levels, with photon fluxes below 10^{14} photons/cm^2/s in the long wavelength infrared (LWIR) spectral range (the final photon flux incident on the IR detector depends on many quantities including, temperature of the target and spectral black body curve, spectral band and accompanying atmospheric transmission, f-number of the objective, and transmission through the optics),[19] we don't expect electron-electron scattering to play a significant role. As for the optical properties, the excitonic enhancement of interband transitions (electron-hole interaction) is also negligible, since the excitonic binding energy is small ($\sim 2\,\mathrm{meV}$).[9]

A. Real-space analysis

The starting point is the eight-band Pidgeon-Brown or Enders $k \cdot p$ Hamiltonian [20]

$$H_{k\cdot p}(\underline{K}) = \begin{bmatrix}
E_{\mathrm{g}} + A_c(k_x^2+k_y^2+k_z^2) & \mathrm{i}Pk_x & \mathrm{i}Pk_y & \mathrm{i}Pk_z \\
-\mathrm{i}Pk_x & Lk_x^2 + M(k_y^2+k_z^2) - \Delta/3 & Nk_xk_y - \mathrm{i}\Delta/3 & k_xN_+k_z + k_zN_-k_x \\
-\mathrm{i}Pk_y & Nk_xk_y + \mathrm{i}\Delta/3 & Lk_y^2 + M(k_x^2+k_z^2) - \Delta/3 & k_yN_+k_z + k_zN_-k_y \\
-\mathrm{i}Pk_z & k_zN_+k_x + k_xN_-k_z & k_zN_+k_y + k_yN_-k_z & Lk_z^2 + M(k_x^2+k_y^2) - \Delta/3 \\
0 & 0 & 0 & 0 \\
0 & 0 & 0 & -\Delta/3 \\
0 & 0 & 0 & -\mathrm{i}\Delta/3 \\
0 & \Delta/3 & \mathrm{i}\Delta/3 & 0
\end{bmatrix}$$

$$\begin{bmatrix}
0 & 0 & 0 & 0 \\
0 & 0 & 0 & \Delta/3 \\
0 & 0 & 0 & -\mathrm{i}\Delta/3 \\
0 & -\Delta/3 & \mathrm{i}\Delta/3 & 0 \\
E_{\mathrm{g}} + A_c(k_x^2+k_y^2+k_z^2) & \mathrm{i}Pk_x & \mathrm{i}Pk_y & \mathrm{i}Pk_z \\
-\mathrm{i}Pk_x & Lk_x^2 + M(k_y^2+k_z^2) - \Delta/3 & Nk_xk_y + \mathrm{i}\Delta/3 & k_xN_+k_z + k_zN_-k_x \\
-\mathrm{i}Pk_y & Nk_xk_y - \mathrm{i}\Delta/3 & Lk_y^2 + M(k_x^2+k_z^2) - \Delta/3 & k_yN_+k_z + k_zN_-k_y \\
-\mathrm{i}Pk_z & k_zN_+k_x + k_xN_-k_z & k_zN_+k_y + k_yN_-k_z & Lk_z^2 + M(k_x^2+k_y^2) - \Delta/3
\end{bmatrix}, \tag{2}$$

written in the zone-center basis

$$S\uparrow, X\uparrow, Y\uparrow, Z\uparrow, S\downarrow, X\downarrow, Y\downarrow, Z\downarrow, \tag{3}$$

where $\underline{K} = (k_x, k_y, k_z)$ (in the following, upper-case letters are for three-dimensional wavevectors and positions), E_{g} is the fundamental gap of the unstrained material, Δ is the spin-orbit splitting, P is the interband momentum matrix element, the renormalized parameters A_c, L, M, and N are obtained from the conduction band effective mass m_c^* and the modified Luttinger parameters in which the remote contribution of the conduction band has been

subtracted[21]

$$A_c = \frac{\hbar^2}{2m_c^*} - \frac{2P^2}{3E_{\rm g}} - \frac{P^2}{3(E_{\rm g}+\Delta)} \tag{4}$$

$$L = -\frac{\hbar^2}{2m_0}(\gamma_1 + 4\gamma_2) \tag{5}$$

$$M = -\frac{\hbar^2}{2m_0}(\gamma_1 - 2\gamma_2) \tag{6}$$

$$N = -\frac{\hbar^2}{2m_0}6\gamma_3. \tag{7}$$

In principle, k·p parameters can be derived from full-Brillouin-zone band structure calculations,[22] but here we adopt the semi-empirical parameter set reported in Ref. 9 and 10, with band offsets and bowing parameters from Ref. 23. InAs and GaSb are almost lattice-matched, while InAs/InAsSb SLs require strain-balancing techniques.[24] Strain was included in the $k \cdot p$ Hamiltonian (2) as described in Ref. 20. In the atomic basis (3), the spin-orbit part of the Hamiltonian is nondiagonal, but Burt-Foreman operator ordering can be more easily defined.[21, 25] According to operator ordering, the Kane parameter N is split into two asymmetric parts $N = N_+ + N_-$, with $N_- = M - \hbar^2/(2m_0)$. The splitting is shown only for the matrix elements of (2) that are linear in k_z, assuming z as the only symmetry-broken direction. Moving to the atomic-like basis set defined in Refs. 26 and 27, within the axial approximation, the bulk Hamiltonian block-diagonalizes with respect to the spin components, i.e., the 8×8 Hamiltonian decouples in two 4×4 blocks, and the energy dispersion becomes isotropic in the transverse wavevector, which simplifies the numerical integration of the self-energies. Rewriting the bulk $k \cdot p$ Hamiltonian as [28]

$$H_{k\cdot p}(\underline{K}) = H_2(\underline{k})k_z^2 + H_1(\underline{k})k_z + H_0(\underline{k}), \tag{8}$$

where $\underline{k}$ is the transverse component of $\underline{K}$, and replacing k_z with the corresponding operator $-i\partial_z$, gives the differential Hamiltonian operator

$$\begin{aligned} H_{k\cdot p}(\underline{k}, z) = &-\partial_z H_2(\underline{k}, z)\partial_z + H_{1L}(\underline{k}, z)\partial_z \\ &+\partial_z H_{1R}(\underline{k}, z) + H_0(\underline{k}, z). \end{aligned} \tag{9}$$

In the envelope function approximation, the nanostructure wavefunction includes a plane wave in the transverse direction, the zone-center Bloch functions $u_a(\underline{R})$ listed in (3), and the slowly-varying envelopes $\zeta_{\underline{k}\alpha}(z)$ that describe how the lattice-periodic functions are mixed together at every position in the symmetry-broken direction z

$$\psi_{\underline{k}\alpha}(\underline{R}) = \frac{1}{\sqrt{A}} e^{{\rm i}\underline{k}\cdot\underline{r}}\, u_a(\underline{R})\, \zeta_{\underline{k}\alpha}(z), \tag{10}$$

where $\underline{r}$ represents the translational invariant directions (x, y), $\underline{R} = (\underline{r}, z)$, $\alpha = (a, i)$ is a compound index combining indices a for band and i for space, and A is the normalization area. Expanding the envelope functions in first-order Lagrange polynomials, the finite-element procedure gives the steady-state Dyson and Keldysh equations in full matrix notation[2, 3, 29]

$$\left[EM - H(\underline{k}) - \Sigma^R(\underline{k}, E)\right] G^R(\underline{k}, E) = I \tag{11a}$$

$$G^{\lessgtr}(\underline{k}, E) = G^R(\underline{k}, E)\Sigma^{\lessgtr}(\underline{k}, E)G^A(\underline{k}, E), \tag{11b}$$

in which a contravariant representation is used for Green's functions and a covariant representation for self-energies, the two representations being related by the overlap matrix M. $\Sigma = \Sigma^B + \Sigma^{e\gamma} + \Sigma^{ep}$ includes both the boundary and the scattering self-energies.[3] The boundary self-energies $\Sigma_B^{R\lessgtr}$ reflecting the openness of system are obtained from the complex band structure of the reservoirs.[30]

The vibrational properties of antimonide-based SLs are quite complex and still almost unexplored. The InAs/GaSb system has the broken-gap type-II electronic band alignment and overlapping optical phonon spectra of the two constituents,[31, 32] while the InAs/InAsSb system has staggered type-II electronic band alignment and staggered overlapping optical phonon spectra,[33] which produces in both cases a wealth of possible phonon modes, including bulk-like (confined in one of the two constituents or extended in both), and interface phonon modes. The interaction with bulk-like modes is usually reduced in short-period SLs, but this reduction is balanced by the increasing contribution of interface modes, [34] whose properties critically depend on technological details such as interfacial bonding, compositional modulation, and alloy disorder.[35] Considering the uncertainties in the phonon spectra (as-grown SLs may significantly differ from design intentions),[35] we assume electrons interacting with bulk phonon modes. We will revisit this approximation in a future work. Coupling to acoustic and polar optical phonons is considered within the deformation potential and the Fröhlich formalism, respectively, by means of fully nonlocal self-energies $\Sigma_{ep}^{R\lessgtr}$ computed in the self-consistent Born approximation[2]

$$\begin{aligned} \left[\Sigma_{\rm ep}^{\lessgtr}(\underline{k}, E)\right]_{\alpha\beta} = &\sum_{\underline{Q}} |U_Q|^2 e^{{\rm i}q_z(z_i - z_j)} \\ &\Big[M\big(N_Q G^{\lessgtr}(\underline{k} - \underline{q}, E \mp \hbar\omega_{\underline{Q}}) + \\ &(N_Q + 1)G^{\lessgtr}(\underline{k} - \underline{q}, E \pm \hbar\omega_{\underline{Q}})\big)M\Big]_{\alpha\beta}, \end{aligned} \tag{12}$$

where $\alpha = (a, i)$ and $\beta = (b, j)$. Phonon occupation numbers N_Q in the (3D) phonon wavevectors $\underline{Q} = (\underline{q}, q_z)$ are computed according to Bose-Einstein statistics. Hot phonons effects are negligible, since background doping and photogenerated carrier concentrations in IR SL absorbers are too small to drive the phonon population out of equilibrium by polar optical emission.[36] Neglecting the principal part, which just leads to energy renormalization, the retarded component of the self-energy reads

[37]

$$\left[\Sigma^R_{\rm ep}(\underline{k},E)\right]_{\alpha\beta} = \sum_{\underline{Q}} |U_Q|^2 e^{{\rm i}q_z(z_i-z_j)} \Big[M\big(N_Q\, G^R(\underline{k}-\underline{q},E+\hbar\omega_{\underline{Q}})+ (N_Q+1)\, G^R(\underline{k}-\underline{q},E-\hbar\omega_{\underline{Q}}) + \frac{1}{2}G^<(\underline{k}-\underline{q},E-\hbar\omega_{\underline{Q}}) - \frac{1}{2}G^<(\underline{k}-\underline{q},E+\hbar\omega_{\underline{Q}})\big)M\Big]_{\alpha\beta}. \tag{13}$$

According to deformation-potential scattering theory, the scattering strength U_Q due to the interaction with acoustic modes is described by

$$U_Q = \sqrt{\frac{\hbar D_a^2}{2V\rho u_l}Q}, \tag{14}$$

where u_l is the longitudinal sound velocity in the material, $D_a = 8\,\mathrm{eV}$ is the deformation potential,[38, Chapter 5] ρ is the semiconductor mass density, and V is the normalization volume. Unless specified, material parameters are from Ref. 39. Assuming a dispersion-less longitudinal optical phonon with energy $\hbar\omega_{\rm LO} = 30\,\mathrm{meV}$, Fröhlich theory of polar optical scattering gives the interaction strength

$$U_Q = \sqrt{\frac{\mathrm{e}^2\hbar\omega_{\rm LO}}{2V}\left(\frac{1}{\epsilon_\infty}-\frac{1}{\epsilon_s}\right)}\frac{Q}{Q^2+q_0^2}, \tag{15}$$

where ϵ_s and ϵ_∞ are the static and optical dielectric constants of the material, and q_0 is the inverse of the Debye-Hückel screening length (10 nm in all the simulations below). The electron-photon self-energy components read in full matrix notation[37, 40, 41]

$$\Sigma^{\lessgtr}_{{\rm e}\gamma}(\underline{k},E) = \sum_{\lambda\underline{Q}} M^\gamma(\underline{k},\lambda)[N_{\lambda\underline{Q}}G^{\lessgtr}(\underline{k},E\mp\hbar\omega_{\lambda\underline{Q}})+ (N_{\lambda\underline{Q}}+1)G^{\lessgtr}(\underline{k},E\pm\hbar\omega_{\lambda\underline{Q}})]M^\gamma(\underline{k},\lambda), \tag{16a}$$

$$\Sigma^R_{{\rm e}\gamma}(\underline{k},E) = \sum_{\lambda\underline{Q}} M^\gamma(\underline{k},\lambda)[N_{\lambda\underline{Q}}G^R(\underline{k},E+\hbar\omega_{\lambda\underline{Q}})+ (N_{\lambda\underline{Q}}+1)G^R(\underline{k},E-\hbar\omega_{\lambda\underline{Q}}) + \frac{1}{2}G^<(\underline{k},E-\hbar\omega_{\lambda\underline{Q}}) - \frac{1}{2}G^<(\underline{k},E+\hbar\omega_{\lambda\underline{Q}})]M^\gamma(\underline{k},\lambda) \tag{16b}$$

with

$$M^\gamma_{\alpha\beta}(\underline{k},\lambda) = \frac{\mathrm{e}}{m_0}\sqrt{\frac{\hbar}{2\epsilon_0 V\omega_\gamma}}[\underline{\epsilon}_{\lambda\underline{Q}}\cdot\underline{p}_{\alpha\beta}(\underline{k})] \tag{17}$$

where $\underline{\epsilon}_{\lambda\underline{Q}}$ is the light polarization of the photon in mode λ and wavevector $\underline{Q}$, and the interband momentum matrix element is[42]

$$\underline{p}_{\alpha\beta}(\underline{k}) = \frac{m_0}{\hbar}\nabla_{\underline{K}}H_{\alpha\beta}(\underline{K}). \tag{18}$$

For a monochromatic illumination of energy $\hbar\omega_\gamma$ and light intensity J_γ, we replace $N_{\lambda\underline{Q}}$ with the number of photons $N_\gamma = \phi_{\omega_\gamma}V/\tilde{c}$, corresponding to the incoming flux $\phi_{\omega_\gamma} = J_\gamma/(\hbar\omega_\gamma)$ of photons with energy $\hbar\omega_\gamma$ and velocity $\tilde{c}$.

B. Mode-space analysis

Inspired by the spectral decomposition of the Green's function, [43] the main idea behind mode space approaches is to transform the kinetic equations from the original real space basis to a more convenient one defined by few basis functions, which should be as close as possible to the eigenstates of the nanostructure. A possible set of problem-matched basis functions can be obtained by selecting the eigenstates of the noninteracting Hamiltonian $\hat{H}_0$ (i.e., without boundary and scattering self-energies) with energies in a given energy range, representing all the relevant conduction channels of the nanodevice. In this representation, the number of basis functions required for a given accuracy should be much less than in the original space, reducing the computational effort significantly. Reduced-order models are usually limited to the coherent limit, since the extension to the dissipative case requires the scattering self-energies to be computed directly in the reduced subspace. An efficient implementation of scattering in mode space is based on the use of localized basis functions obtained by diagonalizing the position operator in the new representation.[44] For field-periodic structures, e.g., quantum cascade lasers, this procedure leads to the definition of maximally localized Wannier functions.[45, 46] Since every localized basis function is associated with the corresponding eigenposition, the scattering self-energies can be discretized directly in mode space, by just replacing the node coordinates of the mesh with these eigenpositions. The effectiveness of any mode space approach obviously depends on the number of basis functions needed to accurately represent the self-energies, but a simple projection scheme violates current conservation, even in the coherent limit, due to the incomplete representation of the boundary self-energies.[44]

In order to reduce the number of basis functions while still satisfying conservation rules, we propose a partitioning technique in which the eigenstates of the nanostructure are divided in two sets, a *near* set including the selected basis functions, and a *remote* set including all the other eigenstates. Current conservation is recovered by folding the influence of the remote modes in an additional self-energy, which is equivalent to the Hamiltonian-folding procedure commonly employed in real space to include the influence of the semi-infinite contacts without actually including them in the simulation domain.[4] More in detail, the numerical generation of problem-matched basis functions proceeds as follows. The gen-

eralized eigenvalue problem

$$H_0\psi_i = E_i M\psi_i \tag{19}$$

formulated in a finite-element overlapping basis is transformed by means of Löwdin symmetric orthogonalization to a standard eigenvalue problem with symmetrically orthogonalized functions, closest in the least square sense to the original nonorthogonal functions, thus eliminating the need for different contravariant and covariant representations for Green's functions and self-energies

$$M^{-1/2}H_0M^{-1/2}\psi_i = E_i\psi_i. \tag{20}$$

The solutions of (20) are classified as near or remote according to the proximity of their respective eigenvalue E_i to some value E_0 lying in the middle of the energy range considered. The position operator is then diagonalized in the near and remote representations to obtain maximally localized basis functions

$$\tilde{Z}_{\alpha_i}\psi^{ML}_{\alpha_i} = z_{\alpha_i}\psi^{ML}_{\alpha_i}, \tag{21}$$

with $\tilde{Z}_\alpha = T^\dagger_\alpha M^{-1/2}\, Z\, M^{-1/2}T_\alpha$, where Z is the finite-element representation of the position operator, and $T_\alpha = \{\psi_{\alpha_i}\}_{i=1}^{n_\alpha}$ is the transformation matrix whose columns are the near ($\alpha = n$) or remote ($\alpha = r$) modes. Having defined the transformation matrix $P = \{P_n, P_r\}$, with $P_\alpha = \{\psi^{ML}_{\alpha_i}\}_{i=1}^{n_\alpha}$, the Dyson an Keldysh equations for retarded and lesser components read in the complete (near plus remote) space

$$\left[\tilde{A}(\underline{k}) - \tilde{\Sigma}^R(\underline{k},E)\right]\tilde{G}^R(\underline{k},E) = I \tag{22a}$$

$$\tilde{G}^<(\underline{k},E) = \tilde{G}^R(\underline{k},E)\tilde{\Sigma}^<(\underline{k},E)\tilde{G}^A(\underline{k},E), \tag{22b}$$

where $\tilde{A} = EI - \tilde{H}$, and Green's functions and self-energies are given by

$$\tilde{\Sigma} = P^\dagger T^\dagger M^{-1/2}\,\Sigma\, M^{-1/2}TP \tag{23a}$$

$$\tilde{G} = P^\dagger T^\dagger M^{1/2}\, G\, M^{1/2}TP. \tag{23b}$$

Folding the influence of the remote states, the final form of the kinetic equations reads in block matrix notation

$$\left[\tilde{A}_{nn} - \tilde{\Sigma}^R_{nn} - \hat{\Sigma}^R_{nn}\right]\tilde{G}^R_{nn} = I_{nn} \tag{24a}$$

$$\tilde{G}^<_{nn} = \tilde{G}^R_{nn}\left[\tilde{\Sigma}^<_{nn} + \hat{\Sigma}^<_{nn}\right]\tilde{G}^A_{nn}, \tag{24b}$$

in which we have defined an additional self-energy $\hat{\Sigma}$ representing the contribution of the remote modes to the coherent solution (the parametric dependence on transverse wavevector and energy has been dropped for clarity):

$$\hat{\Sigma}^R_{nn} = \tilde{A}_{nr}\tilde{g}^R_{rr}\tilde{A}_{rn} \tag{25a}$$

$$\hat{\Sigma}^<_{nn} = -\tilde{\Sigma}^{B<}_{nr}\tilde{g}^A_{rr}\tilde{A}^*_{rn} - \tilde{A}_{nr}\tilde{g}^R_{rr}\tilde{\Sigma}^{B<}_{rn} + \tilde{A}_{nr}\tilde{g}^<_{rr}\tilde{A}^*_{rn}, \tag{25b}$$

with $\tilde{g}^R_{rr} = \tilde{A}^{-1}_{rr}$, and $\tilde{g}^<_{rr} = \tilde{g}^R_{rr}\,\tilde{\Sigma}^{B<}_{rr}\,\tilde{g}^A_{rr}$. From this point forward, the NEGF algorithm proceeds as usual, with the scattering self-energies computed directly in mode space, i.e., we replace in (12) and (13) node coordinates with the eigenpositions z_{n_i}.[44] Once self-consistency is achieved between Green's functions and self-energies, the scattering self-energies are transformed back to real space, and the Dyson and Keldysh equations are solved in real space to obtain the relevant one-particle properties.

The self-consistent solution of (24) may take a large number of iterations to converge in the presence of strongly localized states outside the spectral supports of the contacts.[11] This limitation is not related to the mode space representation but it is intrinsic to the SCBA algorithm, which includes higher-order diagrams at each iteration, regardless whether they are current-conserving or not.[47] In fact, the slow convergence of the SCBA inspired the concept of the lowest order approximation (LOA), which is based on the idea to collect only current-conserving diagrams at each scattering order. Several analytic continuation techniques were applied to the LOA series in order to reconstruct physical observables, proving that current conserving self-energies are not necessarily obtained through a self-consistent scheme.[48–52] These alternative approaches to the SCBA are compatible with mode space approaches, but they will not be treated here.

In addition to convergence issues, the SCBA is formally valid only in the weak coupling limit. Due to the computational complexity of Hedin's equations for the inclusion of vertex corrections,[53] the validity of the SCBA is seldom, if ever, discussed. One notable exception is a NEGF study of inelastic electronic transport in molecular devices, in which, depending on the initial conditions, the SCBA was shown to give multiple self-consistent solutions beyond a critical coupling electron-phonon strength.[54] Part of the reason why it is difficult to assess the limitations of the SCBA is that the numerical instabilities disappear if the Hartree part of the electron-phonon self-energy is neglected, as in most NEGF studies (including this work) of carrier transport in semiconductor nanostrutures. The applicability of Fermi golden rule to III-nitrides despite their strong electron-phonon coupling,[55] makes us confident in the validity of the SCBA in T2SLs, even in the presence of nearly dispersionless holes in the growth direction, due to the weakly ionic nature of the 6.1 Å material system and the strong anisotropy of the hole electronic structure.[56, 57]

III. RESULTS

The accuracy of the proposed approach and its applicability to complex T2SL-based architectures is discussed in Section III A. Interband cascade IR photodetector (ICIPs) achieve high-temperature and high-speed operation by employing a discrete absorber architec-

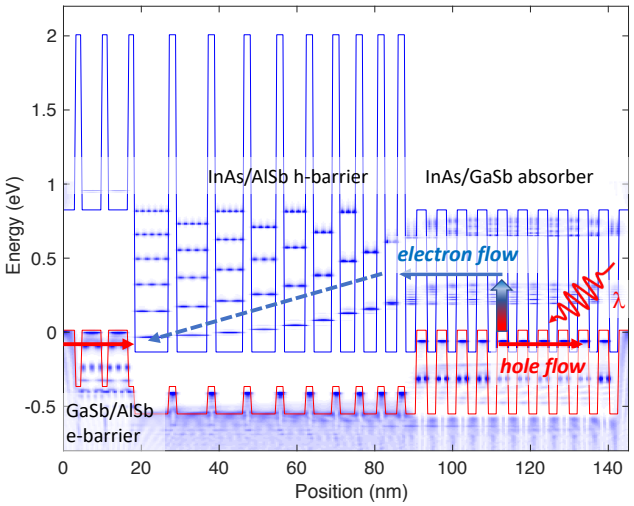

FIG. 1. Local density of states of one stage of a mid-wavelength infrared (MWIR) interband cascade photodetector shown for $\underline{k} = 0$ (color maps). The arrows indicate the direction of the electron and hole flow: the electron-hole pairs photogenerated in the superlattice absorber diffuse along the respective minibands, the electrons towards the hole barrier, where they relax by polar optical transitions down a Wannier-Stark ladder, until they reach the electron barrier, whereupon they tunnel into the valence miniband of the adjacent stage.

ture, each single absorber interposed between quantum-engineered electron and hole barriers to form a series of interband cascade stages. At high temperatures, the diffusion length is typically shorter than the absorption depth of the IR radiation. While the total thickness of the cascade can be comparable or even longer than the diffusion length, the photogenerated electrons travel only over one stage, which is significantly shorter than the diffusion length, before they recombine with the holes in the next stage. The structure considered here includes enhanced barriers, designed to suppress intraband-tunneling current between stages, and p-doped type-II InAs/GaSb superlattice absorbers.[58] Encompassing all the possible carrier transport mechanisms, including interband tunneling, ICIPs represent a good candidate for the accuracy assessment of the proposed mode space approach. Section III B focuses on the nature of carrier transport in LWIR SLs, and on the role of disorder. The connection to semiclassical approaches is made for the $InAs_{0.97}Sb_{0.03}/InAs_{0.55}Sb_{0.45}$ SL investigated experimentally in Ref. 59.

A. Accuracy assessment: ICIPs

Fig. 1 shows the local density of states of the ICIP under consideration. The hole and electron barriers also serve as electron-relaxation and interband-tunneling regions, respectively. The electron-relaxation region is designed to facilitate the transport of photogenerated carriers from the conduction miniband of one stage to the valence miniband of the next,[60]. For simplicity, the structure is considered in flat-band conditions, as the inclusion of space-charge effects will not affect the assessment of the proposed approach.[61]

Fig. 2 (a) shows the spectral photocurrent in one stage of an ICIP illuminated by monochromatic light. In the original real space representation, the device is discretized with a grid spacing of 0.5 nm, resulting, within our multiband $k\cdot p$ framework, in $n_t = 1160$ finite-element basis functions, while mode-space calculations are performed with $n_n = 250$ maximally localized basis functions, i.e., the matrix rank is reduced to approximately 22% of the original space. The continuous stripes in the current spectrum in the absorber region are indicative of miniband transport of the photogenerated electrons mediated by the extended states of the superlattice, while the staircase behavior in the relaxation layer is the signature of sequential tunneling. The interband tunneling through the type-II broken gap and finally the recombination with the holes of the next stage is also clearly visible. Upon convergence, the total energy-integrated current (black solid line) is approximately conserved over the whole device region, which is a very stringent test for any NEGF model. Residual fluctuations in the coherent current shown in panel Fig. 2 (a) (black solid line) may be traced back to the incompleteness of the basis. Neglecting the contribution of the remote modes results in severe violation of current conservation (black dotted line). Since the self-energies are additive, one can separate their contribution to the total current (this is an approximation, of course, because Green's functions determine self-energies and viceversa).[62] The radiative generation spectrum in Fig. 2 (b) shows the photogeneration of carriers in the superlattice absorber, and, unexpectedly, free carrier absorption in the valence band of the electron barrier. The generation current obtained from the integration of the local generation rate[63] (solid line) is equal to the total current in Fig. 2 (a), as expected in the case of complete carrier extraction. A comprehensive simulation of type-II SLs requires the inclusion of defect-mediated nonradiative recombination processes, which determine the extraction efficiency. Recently, a conserving SRH self-energy model fully compatible with the rigorous treatment of electron-photon and electron-phonon scattering within the NEGF formalism was proposed by Aeberhard.[64] Fig. 2 (c) shows the spectral scattering current (color maps) associated to the coupling with polar optical phonons. The phonon-assisted cascade of the (minority) electrons from the conduction miniband of the superlattice absorber across the graded superlattice (relaxation region) is clearly visible.

Encoding the contribution of the remote modes in the self-energy (25) improves significantly the convergence with respect to conventional projection-based approaches. Due to memory limitations of our parallel OpenMP implementation, a convergence analysis with respect to the partition of the modes in near and remote

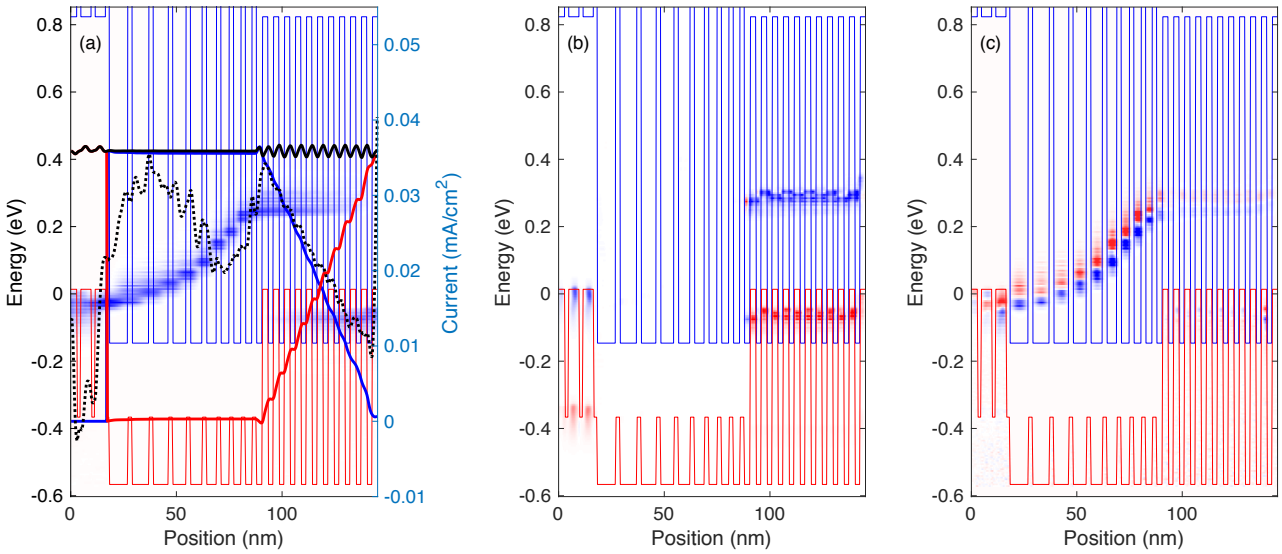

FIG. 2. (a) Spatially resolved photocurrent spectrum under a monochromatic illumination of 1 W/m^2 with $E_\gamma = 0.3\,\mathrm{eV}$ (color maps). The corresponding energy-integrated current (black solid line, right axis) is approximately conserved, save for small oscillations due to the incompleteness of the basis set. Blue and red lines indicate electron and hole contributions, respectively. A position-dependent energy threshold was defined according to the local density of states to separate electron and hole contributions (solid blue and red lines, respectively). Current conservation is clearly violated if the contribution of the remote modes is neglected (black dotted line). (b) Spatially resolved radiative generation spectrum (color maps). (c) Spectral scattering current due to coupling to polar optical phonons,[53] showing the relaxation of the carriers (positive/negative values, i.e., in/out-scattering of electrons, have a gradient from white to blue/red).

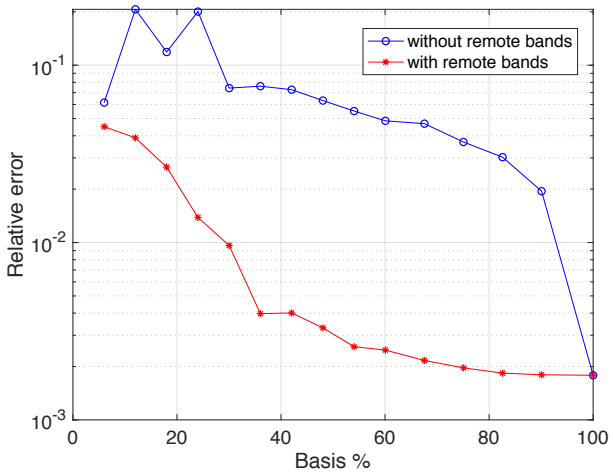

FIG. 3. Standard deviation of the photocurrent fluctuations normalized with respect to the mean spatial average, as a function of n_n/n_t, with and without the contribution of the remote modes.

sets is practicable only for the InAs/GaSb absorber, see Fig. 3. Convergence is better assessed on current densities, which are more sensitive to model-order reduction than other single-particle properties such as carrier densities. The speedup in computation time is close to $(n_n/n_t)^3$, as (25) is evaluated only once at the beginning of the self-consistent cycle (a computational complexity analysis of mode space approaches is presented in Ref. 44).

B. Connection to semiclassical approaches and experiments: LWIR T2SLs

We now turn our attention to the interpretation of the NEGF results from a semiclassical perspective. As a genuine quantum transport model, NEGF provides a comprehensive tool for the analysis of type-II SL photodetectors, with transport and generation-recombination processes encoded in energy- and momentum-dependent scattering self-energies. Nevertheless, it is interesting and useful to explore the connection between NEGF models and semiclassical approaches successfully applied to bulk MCT devices. Macroscopic quantities such as carrier mobilities and lifetimes are admittedly not germane to the NEGF formalism, but they represent critical ingredients needed in quantum-corrected drift-diffusion (DD) models [65]. A notable example is landscape localization theory, in which coherent processes such as localization and tunneling effects are included by means of an effective potential derived from a (non-autonomous) Schroedinger-like equation, while dissipative processes have to be described by appropriate mobilities.[66, 67] A mobility study could also be the starting point to develop fractional DD approaches, which may offer a unified description of carrier transport in disordered SLs, accounting for memory effects associated to trapping mechanisms, along the lines of recent investigations on anomalous (non-Fickian)

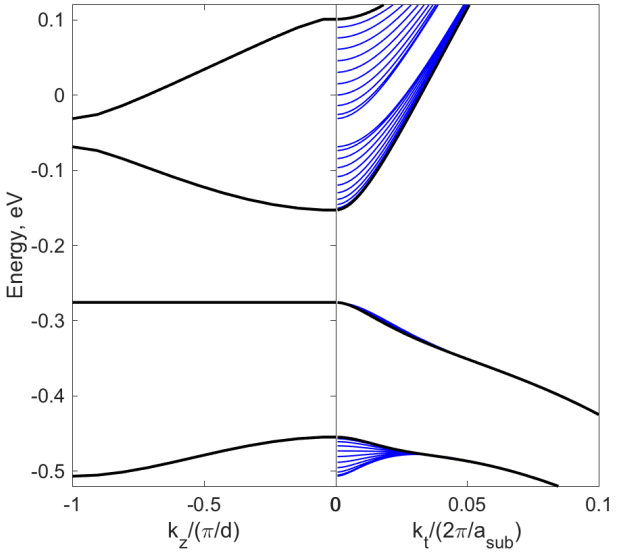

FIG. 4. $k\cdot p$ subband structure of the SL considered in Ref. 59, consisting in the alternating sequence of 10.26 nm $InAs_{0.97}Sb_{0.03}$ and 1.89 nm $InAs_{0.55}Sb_{0.45}$, plotted versus wavevectors along the in-plane (left panel) and growth direction (right panel). The in-plane dispersion for $k_z = 0$ is shown in black, while the blue curves are for equally spaced values of k_z up to the mini-Brillouin-zone boundary π/d (d is the SL period). Bowing parameters of the Luttinger parameters were computed as in Ref. 23.

transport in disordered organic semiconductors.[68]

Different techniques were proposed to extract the mobility from quantum transport simulations. A dispersive, time-dependent diffusion coefficient was obtained from Monte Carlo simulations of AlAs/GaAs disordered SLs.[69] An "apparent" position-dependent mobility was proposed in a study of diffusive transport in fully-depleted silicon-on-insulator transistors, bridging the gap between a Scharfetter-Gummel DD and NEGF models.[70] An efficient method to extract an effective mobility from NEGF and Kubo-Greenwood calculations, while minimizing contact resistance contamination and channel length misestimates, was discussed in the context of thin silicon films.[71] In the context of type-II SLs, electron and hole mobilities may be computed from $v_{n,p} = \mu_{n,p}F$, where F is the electric field and $v_{n,p}$ are the carrier velocities

$$v_{n,p} = \left\langle \frac{J_{n,p}}{\rho_{n,p}} \right\rangle \tag{26}$$

obtained from the NEGF carrier densities $\rho_{n,p}$ and current densities $J_{n,p}$.

The electronic structure computed with periodic boundary conditions[26] is shown in Fig. 4. The cutoff wavelength was found to be 11.8 μm, close to the experimental value of 12.5 μm extracted from low-temperature photoluminescence spectra.[59] The local density of states shown in Fig.5 reveals that the conduction minibands width Δ is larger than the gaps between them, while for the highest valence miniband, Δ is smaller than 1 meV (this value was obtained directly from the dispersion of the band structure along k_z, and so it does not include homogenous or inhomogeneous broadening). The difference in Δ, which in part is due to the relatively low conduction band offsets in InAs/InAsSb SLs, has a profound effect on the electron and hole transport properties. Although the spatially resolved spectral current in both n- and p-type SLs looks similar for small electric fields, see the continuous stripes crossing the band diagrams in Fig. 5, the nature of carrier transport for electrons and holes is very different. A closer inspection of the current components reveals that electron transport is mainly a coherent process through extended Bloch states at low fields, which can be expressed by the familiar Landauer-Büttiker formula

$$I_{\text{coherent}} = \frac{\mathrm{e}}{\hbar}\,\mathrm{Tr}\{\Gamma_1^B G^R \Gamma_2^B G^A\}(f_1 - f_2), \tag{27}$$

where $\Gamma_{1,2}^B$ are the broadening functions of the two contacts. On the other hand, hole transport is entirely non-coherent even in the low field limit, meaning that the holes, strongly localized in the weakly-coupled InAsSb QWs, can move across the miniband only if assisted by scattering mechanisms such as carrier-phonon interactions to (I_{coherent} is negligible compared to the scattering current).

Fig. 6 shows the electron and hole drift velocities as a function of the electric field at $T = 200$ K. The velocities are almost linear for low fields, confirming that the structure is long enough to reach the ohmic drift velocity regime. The critical field at which the electron drift velocity peaks is approximately 4 kV/cm, which corresponds to a potential drop per period $\mathrm{e}Fd = 5$ meV. From a semiclassical perspective, beyond this critical field, the electrons experience unscattered Bloch oscillations in the mini-Brillouin zone, which do not contribute to the net current. For higher fields, the Bloch oscillations should eventually lead to the breaking of the miniband into a ladder of Wannier-Stark (WS) levels, and carrier transport is best described by hopping between the states of the WS ladder rather than by miniband transport. However, due to the large width of the electron minibands and their relative small separation in energy, this condition is never reached. For higher fields, the electron velocity increases again because coherent tunneling between minibands (interminiband transport) becomes possible.

In n-type LWIR T2SLs, a low hole velocity and therefore a low collection efficiency is expected from the large band-edge hole effective mass in the growth direction, and perhaps for this reason, most LWIR detectors have been based on p-type absorbers; the experimental evidence that hole mobility in T2SLs is not as poor as expected was explained with the anisotropy and non-parabolicity of the valence band away from the band edge.[56] Our calculations indicate that the hole velocity, although approximately one order of magnitude smaller than the electron velocity, is significantly higher than expected. Esaki-Tsu theory[72] of superlattice transport in

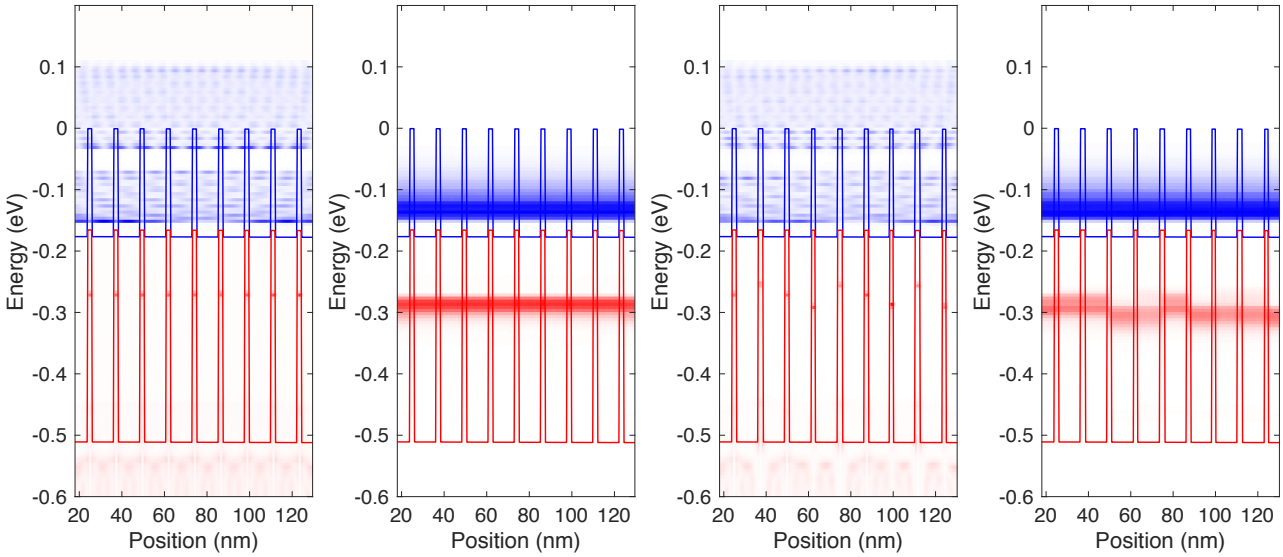

FIG. 5. Local density of states shown for $\underline{k} = 0$, computed for the ordered (a) and disordered SL (c). The applied electric field is $F = 0.1\,\mathrm{kV/cm}$. The first valence miniband (the sharp red peaks in the LDOS) is strongly localized in both energy and space; energy alignments are severely disrupted by the disorder, while the wider conduction minibands are not visibly affected, suggesting that hole transport is likely to be more sensitive to disorder. This is confirmed by the spatially-resolved current spectrum shown in the ordered (b) and disordered (d) structure. The energy-integrated current drops by approximately one order of magnitude in the presence of geometrical fluctuations at $T = 200\,\mathrm{K}$.

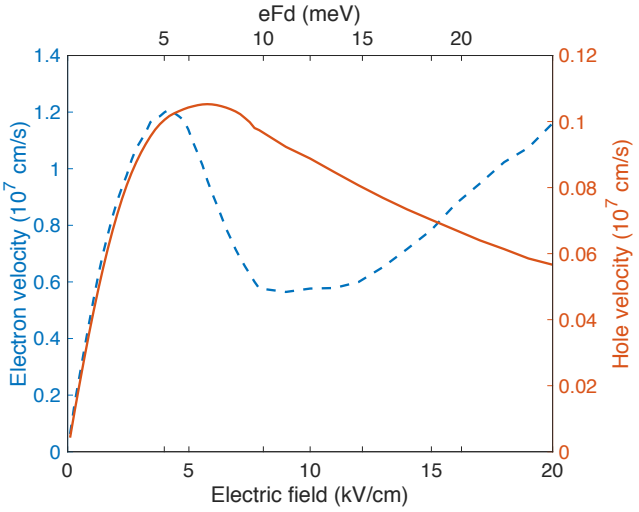

FIG. 6. Electron (left axis, dashed blue curve) and hole (right axis, solid red curve) velocity as a function of the applied electric field (lower axis) and of the potential drop per period eFd (upper axis), at $T = 200\,\mathrm{K}$.

terms of Bloch oscillations fails for such a narrow miniband, as e$Fd \gg \Delta$ for any realistic field F. Hole transport is always dissipative. The spectral scattering rates indicate that near the flatband condition, the holes move across the superlattice by hopping up and down the miniband, emitting and absorbing polar optical phonons. At higher fields, a WS ladder is clearly visible and electron hopping in the valence band is mostly a downhill process governed by the spontaneous emission of phonons.[73]

The velocity-field curves in Fig. 6 were computed for an ideal SL, but the very concept of miniband becomes questionable when Δ becomes very small, due to crystal imperfections and other departures from ideality. Experimental investigations of vertical hole transport in type-II antimonide-based SLs provide a clear indication of the presence of hopping mechanisms between trap states, with hole transport characteristics similar to those seen in amorphous semiconductors displaying Anderson localization. Olson et al. estimated the hole mobility by measuring minority carrier lifetimes and the fraction of injected holes that diffuse in the T2SL base region of a bipolar transistor; different slopes in the Arrhenius plot of the hole mobility were attributed by the authors to distinct transport regimes, from miniband transport of thermally activated carriers, to a regime dominated by hopping within defect states above the miniband mobility edge.[59] In a SL, the disorder may originate from crystal defects, interface roughness, compositional and thickness fluctuations of the layers. In order to investigate carrier transport in disordered SLs, we have added/subtracted randomly one ML to each layer, breaking the translational symmetry along the growth axis. The effect of the disorder is particularly evident for the hole miniband, which appears to be severely disrupted, see the local density of states shown in Fig. 5c, and the spectral current densities in Fig. 5d. And in fact, the hole current at $T = 200\,\mathrm{K}$ is reduced by one order of magnitude with respect to the ordered structure, while the electron current is nearly unaffected at the same temperature.

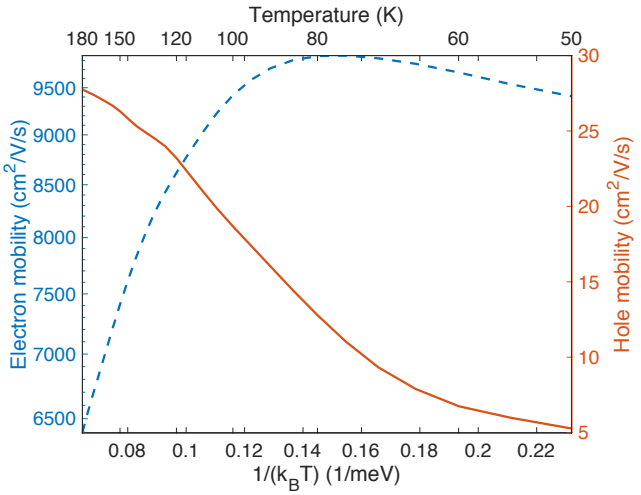

FIG. 7. Electron (left axis, dashed blue curve) and hole (right axis, solid red curve) mobility of the disordered SL as a function of inverse temperature, computed for an electric field of 0.1 kV/cm.

Fig. 7 shows the electron and hole low-field mobility (at $F = 0.1\,\mathrm{kV/cm}$) of the disordered SL as a function of inverse temperature. The electron mobility μ_n shows the conventional phonon-limited temperature dependence above 80 K, in which carrier-phonon scattering slows down the electron velocity, which is typical of miniband conduction. At lower temperatures, the energy-resolved current density becomes spectrally narrower, involving mainly the less extended states near the bottom of the conduction miniband, which results in a slight decrease of μ_n. On the other hand, the hole mobility is thermally activated in the whole temperature range. The calculated hole mobilities are smaller than the experimental results obtained by Olson, especially at higher temperatures, probably because the disorder is applied to the whole SL, irrespectively of the lateral degree of freedom. In general, in a SL sample of macroscopic size, the well/barrier thicknesses may fluctuate in the layer plane, meaning that fully localized states along the growth axis may coexist with miniband states sufficiently extended to allow transport, so that percolative transport along high conduction paths may even conceal the presence of localized states from mobility experiments. The activation energy estimated from our calculations $E_a = 17.1\,\mathrm{meV}$ is very close the one reported in Ref. 59 for region 3 ($E_a = 16\,\mathrm{meV}$), in which transport was considered to be dominated by hopping between localized states near the mobility edge, in the exponential tail of the valence miniband.

IV. CONCLUSION

Scaled on cluster architectures, the mode space approach, corrected to include the effect of the remote bands, is an enabling tool towards the simulation of realistic T2SL photodetectors. While it is difficult to combine the two pictures at opposite ends of the possible transport mechanisms – miniband transport and hopping regime – in a semiclassical theory that is valid at all fields and temperatures, the NEGF approach seamlessly describes situations in which the main ingredients, e.g., miniband widths, localization effects due to electric fields, geometrical and compositional fluctuations, and scattering-induced broadening determine a smooth transition between transport regimes. This is the most probable scenario in the realm of IR SL detectors.

ACKNOWLEDGMENTS

We thank Urs Aeberhard and Jonathan Schuster for useful discussions. This work was supported by the U.S. Army Research Laboratory through the Collaborative Research Alliance (CRA) for Multi-Scale multidisciplinary Modeling of Electronic materials (MSME). The computational resources were provided by HPC@POLITO (http://www.hpc.polito.it), the DoD HPC Systems and the 2019 Army Research Office DURIP Award (Grant No. W911NF-19-1-0161) made to Dr. E. Bellotti.

[1] A. Rogalski, P. Martyniuk, and M. Kopytko, "InAs/GaSb type-II superlattice infrared detectors: Future prospect," Appl. Phys. Rev. **4**, 031304 (2017).
[2] S. Steiger, *Modelling Nano-LEDs*, Ph.D. thesis, Eidgenössische Technische Hochschule Zürich (2009).
[3] U. Aeberhard, *A Microscopic Theory of Quantum Well Photovoltaics*, Ph.D. thesis, Eidgenössische Technische Hochschule Zürich (2008).
[4] U. Aeberhard, "Photovoltaics at the mesoscale: insights from quantum-kinetic simulation," J. Phys. D **51**, 323002 (2018).
[5] A small imaginary potential $i\eta$ is included in the Keldysh components of the self-energy. While these terms are negligible in the interacting case, they are needed to start the self-consistent Born loop in the presence of bound states lying outside the bandwidth of the contacts.[74] After the first iteration, η is set to zero to ensure current conservation.
[6] Y. Wei and M. Razeghi, "Modeling of type-II InAs/GaSb superlattices using an empirical tight-binding method and interface engineering," Phys. Rev. B **69**, 085316 (2004).
[7] R. Magri and A. Zunger, "Effects of interfacial atomic segregation and intermixing on the electronic properties of InAs/GaSb superlattices," Phys. Rev. B **65**, 165302 (2002).

[8] P. C. Klipstein, "Operator ordering and interface-band mixing in the Kane-like Hamiltonian of lattice-matched semiconductor superlattices with abrupt interfaces," Phys. Rev. B **81**, 235314 (2010).

[9] Y. Livneh, P. C. Klipstein, O. Klin, N. Snapi, S. Grossman, A. Glozman, and E. Weiss, "$k \cdot p$ model for the energy dispersions and absorption spectra of InAs/GaSb type-II superlattices," Phys. Rev. B **86**, 235311 (2012).

[10] Y. Livneh, P. C. Klipstein, O. Klin, N. Snapi, S. Grossman, A. Glozman, and E. Weiss, "Erratum: $k \cdot p$ model for the energy dispersions and absorption spectra of InAs/GaSb type-II superlattices," Phys. Rev. B **90**, 039903(E) (2014).

[11] U. Aeberhard, "Challenges in the NEGF simulation of quantum-well photovoltaics posed by non-locality and localization," Phys. Status Solidi B **99**, 1800500 (2019).

[12] M. Luisier, A. Schenk, and W. Fichtner, "Quantum transport in two- and three-dimensional nanoscale transistors: Coupled mode effects in the nonequilibrium Green's function formalism," J. Appl. Phys. **100**, 043713 (2006).

[13] D. A. Lemus, J. Charles, and T. Kubis, "Mode-space-compatible inelastic scattering in atomistic nonequilibrium Green's function implementations," `https://arxiv.org/abs/2003.09536` (2020).

[14] D. Z. Ting, A. Soibel, A. Khoshakhlagh, L. Höglund, S. A. Keo, S. B. Rafol, C. J. Hill, A. M. Fisher, E. M. Luong, J. Nguyen, J. K. Liu, J. M. Mumolo, B. J. Pepper, and S. D. Gunapala, "Antimonide type-II superlattice barrier infrared detectors," in *SPIE Defense+Security, Infrared Technology and Applications XLIII*, Vol. 10177, Proceedings of the SPIE (Anaheim, CA, 2017) p. 101770N.

[15] D. O. Winge, M. Franckié, C. Verdozzi, A. Wacker, and M. F. Pereira, "Simple electron-electron scattering in non-equilibrium Greens function simulations," J. Phys. Conf. Ser. **696**, 012013 (2016).

[16] U. Aeberhard, "Quantum transport simulation of hot carrier photocurrent generation in quantum well solar cells," Semiconductor Sci. Technol. **34**, 094002 (2019).

[17] O. Bonno, J.-L. Thobel, and F. Dessenne, "Modeling of electron-electron scattering in Monte Carlo simulation of quantum cascade lasers," J. Appl. Phys. **97**, 043702 (2005).

[18] L. C. Hirst, R. J. Walters, M. F. Führer, and N. J. Ekins-Daukes, "Experimental demonstration of hot-carrier photo-current in an InGaAs quantum well solar cell," Appl. Phys. Lett. **104**, 231115 (2014).

[19] S. B. Campana, *Passive electro-optical systems*, The Infrared & Electro-Optical Systems Handbook, Vol. 5 (SPIE, Washington, 1993).

[20] P. Enders, A. Bärwolff, M. Woerner, and D. Suisky, "$\mathbf{k} \cdot \mathbf{p}$ theory of energy bands, wave functions, and optical selection rules in strained tetrahedral semiconductors," Phys. Rev. B **51**, 16695 (1995).

[21] R. G. Veprek, S. Steiger, and B. Witzigmann, "Ellipticity and the spurious solution problem of $k \cdot p$ envelope equations," Phys. Rev. B **76**, 165320 (2007).

[22] X. Zhou, F. Bertazzi, M. Goano, G. Ghione, and E. Bellotti, "Deriving $k \cdot p$ parameters from full-Brillouin-zone descriptions: A finite-element envelope function model for quantum-confined wurtzite nanostructures," J. Appl. Phys. **116**, 033709 (2014).

[23] P. C. Klipstein, Y. Livneh, A. Glozman, S. Grossman, O. Klin, N. Snapi, and E. Weiss, "Modeling InAs/GaSb and InAs/InAsSb superlattice infrared detectors," J. Electron. Mater. **43**, 2984–2990 (2014).

[24] D. Lackner, M. Steger, M. L. W. Thewalt, O. J. Pitts, Y. T. Cherng, S. P. Watkins, E. Plis, and S. Krishna, "InAs/InAsSb strain balanced superlattices for optical detectors: Material properties and energy band simulations," J. Appl. Phys. **111**, 034507 (2012).

[25] B. Witzigmann, R. G. Veprek, S. Steiger, and J. Kupec, "Comprehensive modeling of optoelectronic nanostructures," J. Comp. Electron. **8**, 389–397 (2009).

[26] P.-F. Qiao, S. Mou, and S. L. Chuang, "Electronic band structures and optical properties of type-II superlattice photodetectors with interfacial effect," Opt. Express **20**, 2319–2334 (2012).

[27] G. Liu and S.-L. Chuang, "Modeling of Sb-based type-II quantum cascade lasers," Phys. Rev. B **65**, 165220 (2002).

[28] R. G. Veprek, *Computational modeling of semiconductor nanostructures for optoelectronics*, Ph.D. thesis, Eidgenössische Technische Hochschule Zürich (2009).

[29] F. Bertazzi, M. Goano, G. Ghione, A. Tibaldi, P. Debernardi, and E. Bellotti, "Electron transport," in *Handbook of Optoelectronic Device Modeling and Simulation*, edited by J. Piprek (CRC Press, Boca Raton, FL, 2017) Chap. 2, pp. 35–80.

[30] M. Luisier, A. Schenk, W. Fichtner, and G. Klimeck, "Atomistic simulation of nanowires in the $sp^3d^5s^*$ tight-binding formalism: From boundary conditions to strain calculations," Phys. Rev. B **74**, 205323 (2006).

[31] A. Fasolino, E. Molinari, and J. C. Maan, "Calculated superlattice and interface phonons of InAs/GaSb superlattices," Phys. Rev. B **33**, 8889(R) (1986).

[32] H. Liu, N. Yue, Y. Zhang, P. Qiao, D. Zuo, B. Kesler, S. L. Chuang, J.-H. Ryou, J. D. Justice, , and R. Dupuis, "Lattice vibration modes in type-II superlattice InAs/GaSb with no-common-atom interface and overlapping vibration spectra," Phys. Rev. B **91**, 235317 (2015).

[33] H. Liu, Y. Zhang, E. H. Steenbergen, S. Liu, Z. Lin, Y.-H. Zhang, J. Kim, M.-H. Ji, T. Detchprohm, R. D. Dupuis, J. K. Kim, S. D. Hawkins, and J. F. Klem, "Raman scattering study of lattice vibrations in the type-ii superlattice InAs/inas$_{1-x}$sb$_x$," Phys. Rev. Appl. **8**, 034028 (2017).

[34] B. K. Ridley, ed., *Electrons and phonons in semiconductor multilayers*, Cambridge Studies in Semiconductor Physics and Microelectronic Engineering (Cambridge University Press, Cambridge, U.K., 1996).

[35] M. R. Wood, *Order and disorder in type-II InAs/InAsSb superlattices*, Ph.D. thesis, Texas A&M Univers (2017).

[36] F. Compagnone, M. Manenti, A. Di Carlo, and P. Lugli, "Hot electrons and hot phonons in quantum cascade lasers," Physica B **314**, 336–340 (2002).

[37] U. Aeberhard and R. H. Morf, "Microscopic nonequilibrium theory of quantum well solar cells," Phys. Rev. B **77**, 125343 (2008).

[38] K. Hess, ed., *Monte Carlo Device Simulation: Full Band and Beyond* (Kluwer Academic Publishers, Boston, 1991).

[39] "Ioffe Physico-Technical Institute, St. Petersburg, Russia, "Physical properties of semiconductors"," .

[40] L. E. Henrickson, "Nonequilibrium photocurrent modeling in resonant tunneling photodetectors," J. Appl. Phys. **91**, 6273 (2002).

[41] A. Buin, A. Verma, and S. Saini, "Optoelectronic response calculations in the framework of $k \cdot p$ coupled to non-equilibrium Green's functions for one-dimensional systems in the ballistic limit," J. Appl. Phys. **114**, 033111 (2013).

[42] L. C. Lew Yan Voon and L. R. Ram-Mohan, "Tight-binding representation of the optical matrix elements: theory and applications," Phys. Rev. B **47**, 15500–15508 (1993).

[43] S. Datta, *Electronic Transport in Mesoscopic Systems* (Cambridge University Press, Cambridge, U.K., 1995).

[44] L. Zeng, Y. He, M. Povolotskyi, X. Liu, G. Klimeck, and T. Kubis, "Low rank approximation method for efficient Green's function calculation of dissipative quantum transport," J. Appl. Phys. **113**, 213707 (2013).

[45] S.-C. Lee and A. Wacker, "Nonequilibrium Green's function theory for transport and gain properties of quantum cascade structures," Phys. Rev. B **66**, 245314 (2002).

[46] A. Wacker, M. Lindskog, and D. O. Winge, "Nonequilibrium Green's function model for simulation of quantum cascade laser devices under operating conditions," IEEE J. Select. Topics Quantum Electron. **19**, 1200611 (2013).

[47] Y. Lee, D. Logoteta, N. Cavassilas, M. Lannoo, M. Luisier, and M. Bescond, "Quantum treatment of inelastic interactions for the modeling of nanowire field-effect transistors," Materials **13**, 60 (2019).

[48] M. Bescond, C. Li, H. Mera, N. Cavassilas, , and M. Lannoo, "Modeling of phonon scattering in n-type nanowire transistors using one-shot analytic continuation technique," J. Appl. Phys. **114**, 153712 (2013).

[49] H. Mera, M. Lannoo, N. Cavassilas, and M. Bescond, "Nanoscale device modeling using a conserving analytic continuation technique," Phys. Rev. B **88**, 075147 (2013).

[50] H. Mera, T. G. Pedersen, and B. K. Nikolic, "Hypergeometric resummation of self-consistent sunset diagrams for steady-state electron-boson quantum many-body systems out of equilibrium," Phys. Rev. B **94**, 165429 (2016).

[51] Y. Lee, M. Lannoo, N. Cavassilas, M. Luisier, and M. Bescond, "Efficient quantum modeling of inelastic interactions in nanodevices," Phys. Rev. B **93**, 205411 (2016).

[52] Y. Lee, M. Bescond, N. Cavassilas, D. Logoteta, L. Raymond, M. Lannoo, and M. Luisier, "Quantum treatment of phonon scattering for modeling of three-dimensional atomistic transport," Phys. Rev. B **95**, 201412(R) (2017).

[53] U. Aeberhard, "Theory and simulation of quantum photovoltaic devices based on the non-equilibrium Green's function formalism," IEEE J. Quantum Electron. **10**, 394–413 (2011).

[54] W. Lee, N. Jean, and S. Sanvito, "Exploring the limits of the self-consistent born approximation for inelastic electronic transport," Phys. Rev. B **79**, 085120 (2009).

[55] S. M. Komirenko, K. W. Kim, M. A. Stroscio, and M. Dutta, "Applicability of the Fermi golden rule and the possibility of low-field runaway transport in nitrides," J. Phys. Condens. Matter **13**, 6233–6246 (2001).

[56] D. Z. Ting, A. Soibel, and S. D. Gunapala, "Hole effective masses and subband splitting in type-II superlattice infrared detectors," Appl. Phys. Lett. **108**, 183504 (2016).

[57] J. Schuster, "Assessment of the modulation transfer function in infrared detectors with anisotropic material properties: type-II superlattices," IEEE Trans. Electron Devices **66**, 1338–1344 (2019).

[58] Z. Tian, R. T. Hinkey, R. Q. Yang, D. Lubyshev, Y. Qiu, J. M. Fastenau, W. K. Liu, and M. B. Johnson, "Interband cascade infrared photodetectors with enhanced electron barriers and p-type superlattice absorbers," J. Appl. Phys. **111**, 024510 (2012).

[59] B. V. Olson, J. F. Klem, E. A. Kadlec, J. K. Kim, M. D. Goldflam, S. D. Hawkins, A. Tauke-Pedretti, W. T. Coon, T. R. Fortune, E. A. Shaner, and M. E. Flatté, "Vertical hole transport and carrier localization in $InAs/InAs_{1-x}Sb_x$ type-II superlattice heterojunction bipolar transistors," Phys. Rev. Appl. **7**, 024016 (2017).

[60] Operating under zero bias, ICIPs create one electron from a number of photons equal to the number of the constituent stages, which is exactly the opposite of quantum cascade lasers, and the photosignal is determined by the stage with the smallest photocurrent, usually the last one from the illuminated contact.

[61] A charge self-consistent electronic-structure model for type-II broken-gap superlattices based on a multiband $k\cdot p$ envelope-function framework was proposed in Ref. 75 to avoid the ambiguous classification of electron and hole states when conduction and valence bands strongly intermix.

[62] T. Schmielau and M. F. Pereira, Jr., "Nonequilibrium many body theory for quantum transport in terahertz quantum cascade lasers," Appl. Phys. Lett. **95**, 231111 (2009).

[63] U. Aeberhard, "Photocarrier extraction in GaAsSb/GaAsN type-II QW superlattice solar cells," Appl. Phys. Lett. **112**, 213904 (2018).

[64] U. Aeberhard, "Nonequilibrium Green's function picture of nonradiative recombination of the Shockley-Read-Hall type," Phys. Rev. B **99**, 125302 (2019).

[65] A. Tibaldi, F. Bertazzi, M. Goano, R. Michalzik, and P. Debernardi, "VENUS: a Vertical-cavity surface-emitting laser Electro-opto-thermal NUmerical Simulator," IEEE J. Select. Topics Quantum Electron. **25**, 1500212 (2019).

[66] M. Filoche, M. Piccardo, Y.-R. Wu, C.-K. Li, C. Weisbuch, and S. Mayboroda, "Localization landscape theory of disorder in semiconductors. I. theory and modeling," Phys. Rev. B **95**, 144204 (2017).

[67] T.-Y. Tsai, K. Michalczewski, P. Martyniuk, C.-H. Wu, and Y.-R. Wu, "Application of localization landscape theory and the k.p model for direct modeling of carrier transport in a type II superlattice InAs/InAsSb photoconductor system," J. Appl. Phys. **127**, 033104 (2020).

[68] K. Y. Choo, S. V. Muniandy, K. L. Woon, M. T. Gan, and D. S. Ong, "Modeling anomalous charge carrier transport in disordered organic semiconductors using the fractional drift-diffusion equation," Org. Electron. **41**, 157–165 (2017).

[69] L.-W. Wang and A. Zunger, "Pseudopotential-based multiband $k \cdot p$ method for $\sim$ 250 000-atom nanostructure systems," Phys. Rev. B **54**, 11417–11435 (1996).

[70] G. Mugny, F. G. Pereira, D. Rideau, F. Triozon, Y. M. Niquet, M. Pala, D. Garetto, and C. Delerue, "A study of diffusive transport in 14nm FDSOI MOSFET: NEGF versus QDD," in *ESSDERC 2016. Proceedings of the 46th European Solid State Device Research Conference (Lau-*

sanne) (IEEE, 2016) pp. 424–427.

[71] Y.-M. Niquet, V.-H. Nguyen, F. Triozon, I. Duchemin, O. Nier, and D. Rideau, "Quantum calculations of the carrier mobility: Methodology, Matthiessen's rule, and comparison with semi-classical approaches," J. Appl. Phys. **115**, 054512 (2014).

[72] S. Rott, P. Binder, N. Linder, and G. H. Döhler, "A combined model for miniband and hopping transport in superlattices," Physica E **2**, 511–514 (1998).

[73] Monte-Carlo calculations of hopping transport predict a weak temperature dependence of the drift velocity in these conditions, since phonon absorption and stimulated emission, whose rates increase with temperature, tend to cancel each other, and the only contribution to the current is therefore the spontaneous emissions of phonons.[72].

[74] K. S. Thygesen and A. Rubio, "Conserving GW scheme for nonequilibrium quantum transport in molecular contacts," Phys. Rev. B **77**, 115333 (2008).

[75] T. Andlauer and P. Vogl, "Full-band envelope-function approach for type-II broken-gap superlattices," Phys. Rev. B **80**, 035304 (2009).

Understanding Fundamental Material Limitations to Enable Advanced Detector Design

E. Bellotti*, F. Bertazzi†, J. Bajaj‡, J. Schuster‡, M. Reed‡
* Boston University, 8 Saint Mary's St, Boston, MA USA 02215
† Dipartimento di Elettronica e Telecomunicazioni, Politecnico di Torino, corso Duca degli Abruzzi 24, 10129 Torino, Italy
‡ U.S. Army Research Laboratory, 2800 Powder Mill Road, Adelphi, MD USA 20783
E-mail: bellotti@bu.edu

***Abstract*—This work presents the activities of the Center for Semiconductor Modelling in the area of infrared imaging devices. We outline a methodology that enables the study of large scale infrared detector arrays to quantify their optical and electrical performance. Furthermore, we present an approach to investigate the quantum mechanical transport properties of superlattice based detectors that are an emerging technology with potential applications both in commercial and defense system.**

I. Introduction

Electronics and optoelectronics devices based on semiconductor materials play a crucial role for a variety of applications and in systems currently employed in commercial and defense areas. While the development of silicon electronics has reached a high level of sophistication, enabled by well developed and accurate simulation tools, for other semiconductor material systems the situation is significantly less mature. These advanced simulation tools are necessary to gain insight into new physical phenomena and exploit novel electronic, photonic and spintronic materials to enhance device functionalities and performance. Furthermore, these simulation programs have become invaluable instruments to probe future directions for materials and device development. Emerging software tools rely on the availability of modern computer hardware that, with its flexibility and power, has made it possible to tackle complex numerical simulation problems. Many applications, for example those in the electro-optical area, employ semiconductor materials for which simulation and design tools are much less developed and the technology associated to device fabrication is less understood. The development of computationally efficient and truly multi-scale simulation methodologies would lead to a unprecedented understanding of materials and devices' properties and ultimately be valuable approach to mitigate technology development risks.

Bajaj and co-authors [1] have pointed out that a novel approach is necessary to improve the ability of the science and technology community to develop novel semiconductor devices and transition into specific system applications. They emphasized that the timely technology transition with minimal risk requires an understanding of fundamental and technology limitations of material synthesis, device operation and design controllable parameters. For low volume niche semiconductor technologies, industry alone cannot justify these investments simply because there is no significant return on investment. To address this challenge, the Computational Electronics Group at Boston University and a team from the Army Research Laboratory have established the Center for Semiconductor Modeling (CSM). The CSM will focus on the theory, simulation and the experimental validation of the models.

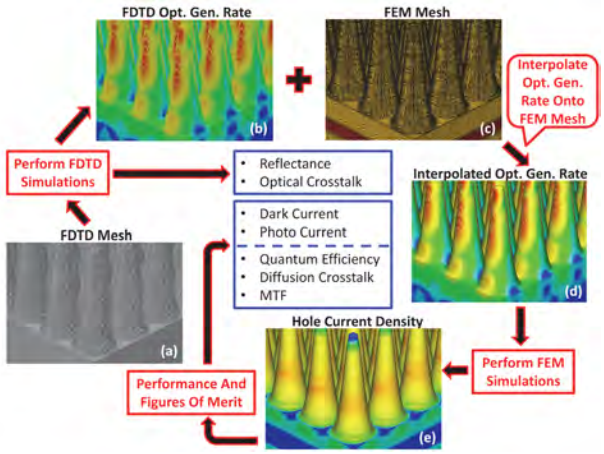

Fig. 1. Overview of modeling steps. Input and output of individual steps include, but are not limited to (a) FDTD structured tensor mesh, (b) optical generation rate saved onto FDTD mesh, (c) FEM unstructured mixed element mesh, (d) optical generation rate interpolated from FDTD mesh onto FEM mesh and (e) hole current density.

II. Modeling Approaches

Modeling of large format infrared (IR) detectors arrays for a variety of spectral ranges presents challenges at different scales [2], [3]. Of particular importance is the study of arrays of pixel detectors that are representative of an entire imaging device. This is becoming more and more important due to the effort to reduce pixel size and increase resolution. Modeling of large format IR detectors presents challenges at different scales. A detailed knowledge of the electronic structure of the material is needed to determine the radiative and non-radiative recombination rates. A realistic description of the device geometry at the pixel and array level is necessary to assess manufacturing issues. All these inputs play an important role in physical device modeling of IR detector arrays. The procedure to simulate the arrays that we have developed is outlined in Fig. 1 [4]–[6]. The electromagnetic response is

978-1-7281-1647-1/19/$31.00 ©2019 IEEE

obtained by a finite difference time domain (FDTD) analysis on a structured tensor mesh (Figure 1a) that is created based on the optical properties of the materials being used. Unlike the structured tensor mesh, the finite element mesh (Figure 1c) consists of triangular prisms of varying dimensions. Solving Maxwell's equations at every node in the mesh at each point in time yields the absorbed power density and the optical generation rate, shown in Fig. 1b, is calculated in each pixel of the array, as well as the total reflectance when the array is illuminated with planewaves. Alternatively, the array can instead be illuminated with a Gaussian beam to compute the optical crosstalk by integrating the optical generation rate in each pixel of the array. Subsequently, the electrical analysis is performed using the FEM to solve the drift-diffusion equations. This requires solving self-consistently the electron and hole continuity equations coupled with Poisson's equation. The optical generation terms in the electron and hole continuity equations are included by interpolating the optical generation rate evaluated from the FDTD simulations onto the finite element mesh (Fig. 1d). The FEM simulations yield quantities such as the hole current density (Fig. 1e) and currents at the contacts from which the quantum efficiency (QE), crosstalk and modulation transfer function (MTF) can be calculated (Fig. 1 (bottom center box)). This approach has been applied to the stude of a variety of IR detector arrays architectures based on a number of semiconductor material systems.

A. Quantum Mechanical Transport Models of SLS Infrared Detectors

The CSM is currently focusing on the performance improvement of IR detectors based on strained layer superlattices (SLSs)[7], [8]. Their optimization requires novel approaches to studying the carrier transport in these quantum structures. Our hierarchical model of carrier transport and optical processes in nanostructured materials includes a nonequilibrium Green's function (NEGF), a quasi-3D drift-diffusion code based on an axisymmetric FEM basis functions coupled to a Poisson-Schrödinger solver to account for quantum confinement, a heat transfer model, and rate equations connecting carriers with different dimensionalities (inspired by NEGF simulations) and a density matrix tool for the calculation of the material gain.

The hierarchical approach implemented in the simulation tools consist of two self-consistency loops, one that connects the Green's functions to the self-energies and, a second one provides the update of the Hartree potential from the solution of Poisson's equation. The boundary self-energies are computed exactly (eigenvalue technique) from the fluctuation-dissipation theorem. The scattering self-energies are computed in the self-consistent Born approximation. We explicitly include acoustic scattering in the equipartition approximation, inelastic polar optical scattering carrier-photon scattering ,ionized impurity scattering, and carrier-carrier interactions included at the Hartree level through coupling to Poisson's equation. Using this newly developed simulation code we have performed a preliminary studies of the carrier transport in type-II InAs/GaSb superlattices (T2SLs). We have have employed

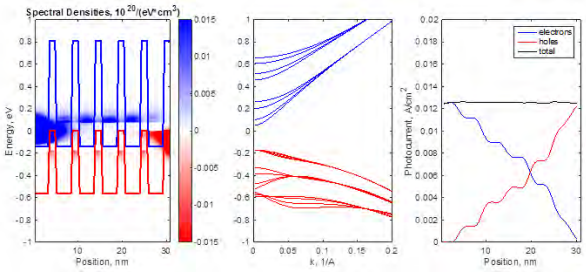

Fig. 2. Band diagram (left panel) of a nine-period InAs/GaSb superlattice, the corresponding subband dispersion (center panel) as a function of the transverse wavevector k, computed with periodic boundary conditions, and calculated electrons, hole and total current (right panel).

our rigorous 8-band k·p model for zincblende crystals which includes the correct operator ordering to ensure numerical stability. With this tool, we have obtained preliminary results of carrier transport in type-II InAs/GaSb superlattice absorbers illuminated with monochromatic light. Figure 2 shows the extraction of carriers photogenerated and transported by the states of a five-period superlattice. The subband diagram indicates a cut-off wavelength of 5.6μm. Upon convergence, the total current (electron + hole) is approximately conserved in the central region of the device.

The CSM is also developing a number of parallel collaborative projects aimed at the validation of the simulation tools. Among these, the measurement of vertical transport properties of carriers in strained layer superlattices and the investigation of noise and non-uniformity in dense detector arrays.

This work was supported by the ARL Center for Semiconductor Modelling under contract W911NF-18-2-0027, managed by Dr. M. Reed. Computational resource were provided by the DURIP Award W911NF1910161 to Dr. E. Bellotti.

REFERENCES

[1] J. Bajaj, R. DeWames, J. Schuster, M. Reed, P. Perconti, and E. Bellotti, "Accelerating technology innovations by early understanding of fundamental and technology limitations of material synthesis and device operation," *SPIE Proceedings*, vol. 10111, pp. 10 111–10 117, 2017.

[2] E. Bellotti, J. Schuster, B. Pinkie, and F. Bertazzi, "Multi-scale modeling of photon detectors from the infrared to the ultraviolet," *SPIE Proceedings*, vol. 8868, pp. 88 680R–1–8, 2013.

[3] J. Schuster, R. DeWames, E. D. Jr, E. Bellotti, N. Dhar, and P. P.S. Wijewarnasuriya, "Junction optimization in hgcdte: Shockley-read-hall generation-recombination suppression," *Applied Physics Letters*, vol. 107, pp. 023 502–1–5, 2015.

[4] J. Schuster, B. Pinkie, S. Tobin, C. Keasler, D. D'Orsogna, and E. Bellotti, "Numerical Simulation of Third-Generation HgCdTe Detector Pixel Arrays," *IEEE J. Select. Topics Quantum Electron.*, vol. 19, no. 5, p. 3800415, 2013.

[5] J. Schuster and E. Bellotti, "Evaluation of quantum efficiency, crosstalk, and surface recombination in hgcdte photon-trapping structures," *J. Electron. Mater.*, vol. 43, p. 2808, Aug. 2014.

[6] ——, "Numerical simulation of crosstalk in reduced pitch hgcdte photon-trapping structure pixel arrays," *Opt. Eng.*, vol. 21, p. 14713, Jun. 2013.

[7] M. Tidrow, L. Zheng, H. Barcikowski, J. Wells, and L. Aitcheson, "Manufacture of sb-based type ii strained layer superlattice focal plane arrays," *CS MANTECH Conference*, May 2009.

[8] C. Grein, J. Garland, and M. Flatte, "Strained and unstrained layer superlattices for infrared detection," *J. Electron. Mater*, vol. 38, pp. 1800–1804, 2009.